

5-2019

Preliminary Test Predictions for Scale Ram-Air Parachute Testing

Christian A. Guzman Zurita

Follow this and additional works at: <https://commons.erau.edu/edt>



Part of the [Aerodynamics and Fluid Mechanics Commons](#)

Scholarly Commons Citation

Zurita, Christian A. Guzman, "Preliminary Test Predictions for Scale Ram-Air Parachute Testing" (2019).
Dissertations and Theses. 446.

<https://commons.erau.edu/edt/446>

This Thesis - Open Access is brought to you for free and open access by Scholarly Commons. It has been accepted for inclusion in Dissertations and Theses by an authorized administrator of Scholarly Commons. For more information, please contact commons@erau.edu.

PRELIMINARY TEST PREDICTIONS FOR SCALE

RAM-AIR PARACHUTE TESTING

A Thesis

Submitted to the Faculty

of

Embry-Riddle Aeronautical University

by

Christian A. Guzman Zurita

In Partial Fulfillment of the

Requirements for the Degree

of

Master of Science in Aerospace Engineering

May 2019

Embry-Riddle Aeronautical University

Daytona Beach, Florida

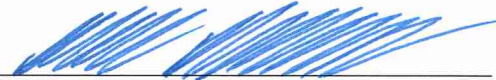
PRELIMINARY TEST PREDICTIONS FOR SCALE
RAM-AIR PARACHUTE TESTING

by

Christian A. Guzman Zurita

A Thesis prepared under the direction of the candidate's committee chairman, Dr. Mark Ricklick, Department of Aerospace Engineering, and has been approved by the members of the thesis committee, Dr. John Leishman and Dr. Ebenezer Gnanamanickam. It was submitted to the School of Graduate Studies and Research and was accepted in partial fulfillment of the requirements for the degree of Master of Science in Aerospace Engineering.

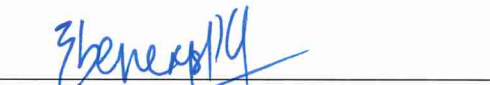
THESIS COMMITTEE



Chairman, Dr. Mark Ricklick



Member, Dr. J. Gordon Leishman



Member, Dr. Ebenezer Gnanamanickam



Graduate Program Coordinator, Dr. Magdy Attia

4/23/2019
Date



Dean of College of Engineering, Dr. Maj Mirmirani

4/23/2019
Date



Senior Vice President for Academic Affairs and Provost, Dr. Lon Moeller

4/24/19
Date

ACKNOWLEDGMENTS

It is an honor for me to gratefully acknowledge the people who have been with me on this journey as I have worked on this thesis. First, I owe my highest gratitude to my father Carlos, my mother Nancy, and my brothers Paul and Steven for the unconditional love, motivation, and support to pursue and achieve my dreams at places far away from my family and home, Ecuador.

Second, I would like to thank my supervisor, Dr. Ricklick, for his guidance, patience and support throughout these three years of investigation. Third, special thanks to my committee members, Dr. Leishman and Dr. Gnanamanickam, who encouraged and challenged me to develop technical skills. Additionally, special thanks to John Leblanc and the Performance Designs team for sharing their experience and knowledge on the design of ram-air parachutes.

Finally, I would like to thank my friends who I had the opportunity to share memorable moments along my university career. I share this thesis with my friend and work partner, Angelo Fonseca, who provided me invaluable knowledge, support and advice. Moreover, special thanks to all my closest friends Juan Granizo, Cristian Angarita, Vanessa Onyullo, May Chong Chan, Nathalie Quintero, Silvana Ureña, Andrea Cevallos, Wenyu Li, Amay Desai, Anish Prasad, Yogesh Pai, Gasper Hrescak, and my friends from groups “Los Cinco del Altiplano”, “The Fireballers” and “Gas Turbine Lab”, who I shared uncountable times of laughs, dinners, drinks, workout trainings, trips, concerts, and long overnights studies.

“Hope the voyage is a long one, full of adventure, full of discovery.”

C. P. Cavafy

TABLE OF CONTENTS

LIST OF TABLES	vi
LIST OF FIGURES	vii
SYMBOLS.....	xi
ABBREVIATIONS	xiii
NOMENCLATURE	xiv
ABSTRACT.....	xv
1. Introduction	1
1.1. Introduction to Ram-Air Parachutes	1
1.2. Motivation for this Study	6
1.3. Thesis Objectives.....	7
1.4. Thesis Outline.....	8
2. Literature Review.....	10
2.1. Introduction.....	10
2.2. Design Parameters.....	10
2.3. Aerodynamic Characteristics.....	12
2.3.1. Distortions on the Canopy Structure	16
2.4. Experimental Studies.....	20
2.5. Computational Studies	34
3. CAD Methodology and CFD Approach.....	49
3.1. Parafoil Geometry Development.....	49
3.1.1. Introduction to CATIA V5	49
3.1.2. Programming Interface Approach.....	50
3.1.3. CAD Design Methodology	51
3.1.4. Benchmark Geometry Models.....	55
3.2. Computational Modeling Approach.....	58
3.2.1. COMSOL 5.3 Multiphysics Introduction	59
3.2.2. Governing Equations, Turbulence Modeling and Wall Treatment.....	59
3.2.3. General Model Setup.....	61
3.2.4. Boundary Conditions	62
3.2.5. Mesh Independence Study	63
3.2.6. Computational Time.....	68
3.2.7. Test Cases and Flow Parameters	70
3.2.8. Test Matrix.....	75
4. Results and Discussion	76
4.1. Introduction.....	76
4.2. Geometry Creation	76
4.3. Computational Analysis.....	81
4.3.1. Validation of Numerical Results	82

4.3.2.	Reynolds Number Sensitivity	86
4.3.3.	Domain Size Sensitivity	92
5.	Conclusion, Recommendations and Future Work.....	103
5.1.	Conclusions.....	103
5.2.	Recommendations and Future Work	104
	REFERENCES	106
	Appendices.....	109
A.	Airfoil Coordinates of Ware & Hassell Canopy Model.....	109
B.	Experimental Data Points Digitalization.....	110
C.	Blockage Area Estimation.....	112
D.	CFD Results Summary.....	114
E.	2D Force Balance Development	117
E.1.	Introduction.....	117
E.2.	Force Measurement Approach	117
E.3.	Equipment and Experimental Setup.....	121
E.4.	Data Reduction	125
E.4.1.	Single Load Cell Calibration	125
E.4.2.	Load Cell Arrangement Calibration.....	127
E.5.	Results and Discussion.....	131

LIST OF TABLES

Table 3.1 Geometry characteristics of the scaled kite model.	56
Table 3.2 Geometry characteristics of the canopy model from Ware & Hassell.	57
Table 3.3 Run parameters for mesh independence study.	66
Table 3.4 Run parameters for computational time study in the cluster Vega.	69
Table 3.5 Fluid flow conditions and run parameters for the analysis of Case 1.	70
Table 3.6 Fluid flow conditions and run parameters for the analysis of Case 2.	71
Table 3.7 Canopy geometry dimensions, fluid flow conditions and run parameters for the analysis of Case 3.	72
Table 3.8 Fluid flow conditions and run parameters for the analysis of Case 3 Compressible.	73
Table 3.9 CFD test matrix.	75
Table 4.1 Values of lift curve slope (a), percentage of change in lift slope and offset at $\alpha = 0^\circ$ for Case 3, Case 3 Compressible and Case 4 as compared with Case 1.	95
Table 4.2 Values of L/D_{max} for Case 3, Case 3 Compressible and Case 4 and percentage of change as compared with Case 1.	101

LIST OF FIGURES

Figure 1.1	Ram-air parachute. Adapted from (Ortega, Flores, & Pons-Prats, 2017).	2
Figure 1.2	Airflow around a canopy cross section. Adapted from (Sobieski, 1994).....	4
Figure 1.3	Schematic of maneuverability and stability of the canopy. Adapted from (McConnel, 2017).....	5
Figure 2.1	Underside view of an inflated ram-air parachute (Adapted from Tactical Parachute Delivery Systems Inc., retrieved from http://tpdsairborne.com/products/parachutes/hlt-r/).....	18
Figure 2.2	Rear view of an inflated ram-air parachute (Adapted from Air Freshener, retrieved from https://airfreshener.club/quotes/ram-air-parachute-dimensions.html).....	18
Figure 2.3	Rib displacement and opening section of a ram-air parachute (Adapted from Tactical Parachute Delivery Systems Inc., retrieved from http://tpdsairborne.com/products/parachutes/hlt-r/).....	19
Figure 2.4	Notre Dame experimental set-up. Adapted from (Nicolaidis, 1971).....	21
Figure 2.5	NASA Langley wind tunnel schematic (Adapted from National Aeronautics and Space Administration, retrieved from https://www.nasa.gov/centers/langley/news/factsheets/30X60.html)	22
Figure 2.6	Tether test schematic set-up. Adapted from (Ware & Hassell, 1969).....	23
Figure 2.7	CL, CD and CL/CD versus α for a rectangular canopy with AR of 2. Adapted from (Nicolaidis, 1971).	24
Figure 2.8	CL versus α and drag polar for a rectangular canopy with AR of 2. Adapted from (Ware & Hassell, 1969).....	26
Figure 2.9	Rigid arched wing experimental set-up. Adapted from (Belloc, 2015).	27
Figure 2.10	CL and CL vs CD for experimental tests of a rigid arched wing. Adapted from (Belloc, 2015).....	28
Figure 2.11	Schematic of an experimental set-up for a pseudo 2D test. Adapted from (Uddin & Mashud, 2010).....	29
Figure 2.12	Variation of internal pressure with angle of attack of a pseudo 2D experimental test. Adapted from (Uddin & Mashud, 2010).	29
Figure 2.13	Internal and external pressure distribution of a pseudo 2D experimental test. Adapted from (Uddin & Mashud, 2010).....	30
Figure 2.14	Experimental set-up for laser scanning of an inflated canopy model. Adapted from (Lee & Li, 2007).	32
Figure 2.15	3D Scan views of the canopy inflated. Adapted from (Lee & Li, 2007).	33
Figure 2.16	Pressure field and velocity magnitude around the baseline airfoil model for 7° angle of attack. Adapted from (Mohammadi & Johari, 2010).	36

Figure 2.17 Pressure field and velocity magnitude around the cross section airfoil model for 7° angle of attack. Adapted from (Mohammadi & Johari, 2010).	37
Figure 2.18 Vorticity contours for the baseline and cross section airfoil models for 7° angle of attack. Adapted from (Mohammadi & Johari, 2010).	37
Figure 2.19 Structure mesh for 2D CFD analysis of an opened and closed NSRDEC airfoil shape. Adapted from (Ghoreyshi, et al., 2016).	39
Figure 2.20 Lift and Drag coefficients versus angle of attack curves for different CFD analysis and experiments for a straight wing. Adapted from (Ghoreyshi, et al., 2016).	40
Figure 2.21 2D and 3D geometries with distortions. Adapted from (Fonseca, 2018).	41
Figure 2.22 Internal surface pressure for the seven-cell canopy at 0° angle of attack, top view. Adapted from (Fonseca, 2018).	42
Figure 2.23 Non-deformed and deformation on the canopy structure by different external surface pressures. Adapted from (Peralta & Johari, 2015).	43
Figure 2.24 Cross section of the 3D CFD domain and boundary conditions applied to the walls. Adapted from (Fogell, 2014).	44
Figure 2.25 3D streamlines around the bottom surface of an inflated single cell canopy geometry. Adapted from (Fogell, 2014).	45
Figure 2.26 Truncated cone CFD domain schematic representation. Adapted from (Burnett, 2016).	46
Figure 2.27 Experimental test of a single cell canopy. Adapted from (Burnett, 2016).	47
Figure 3.1 Schematic for the CAD generation process.	50
Figure 3.2 2D airfoil shape of a scaled kite model.	52
Figure 3.3 Full number of canopy ribs generated with a MATLAB script.	52
Figure 3.4 Rib coordinate points imported into CATIA for a half kite canopy model.	53
Figure 3.5 General structure of the scaled canopy kite.	53
Figure 3.6 Location of the opening inlet in a 2D airfoil shape.	54
Figure 3.7 Canopy surfaces for the kite model simulating a structure inflation.	55
Figure 3.8 Top view of the flexible scaled kite model.	56
Figure 3.9 CAD model representation of the kite.	56
Figure 3.10 CAD model representation of the canopy from Ware & Hassell.	58
Figure 3.11 Rectangular cuboid, CFD fluid flow domain.	61
Figure 3.12 CFD analysis boundary conditions.	62
Figure 3.13 Domain mesh.	64
Figure 3.14 Boundary layer mesh along the edges of a chamber cross section view.	65
Figure 3.15 Convergence plots for the independence mesh study.	67

Figure 3.16 Non-dimensional distance to cell center for the coarse mesh.	68
Figure 3.17 Computational time required in the cluster Vega for two different meshes..	69
Figure 3.18 Rectangular cuboid, CFD fluid flow domain with dimensions of the wind tunnel test section.....	74
Figure 4.1 Canopy model 1, Ware & Hassell with multiple deformations.....	77
Figure 4.2 Canopy model 2 (Coe & LeBlanc, 2016).....	78
Figure 4.3 Canopy model 3 (Coe & LeBlanc, 2016).....	79
Figure 4.4 Canopy model 4 (Coe & LeBlanc, 2016).....	80
Figure 4.5 Non-dimensional distance to cell center for the canopy surfaces of Case 1 at 4° angle of attack.	82
Figure 4.6 CL versus α of the numerical simulations of Case 1 in comparison with experimental data available from literature.	84
Figure 4.7 CD versus α of the numerical simulations of Case 1 in comparison with experimental data.	85
Figure 4.8 CL versus CD of the numerical simulations of Case 1 in comparison with experimental data.	86
Figure 4.9 CL versus α of the numerical simulations of Case 2 in comparison with Case 1 and the experimental data.....	88
Figure 4.10 CD versus α of the numerical simulations of Case 2 in comparison with the Case 1 and the experimental data.....	89
Figure 4.11 CL versus CD of the numerical simulations of Case 2 in comparison with the Case 1 and the experimental data.....	90
Figure 4.12 Internal surface pressure on the canopy normalized with the free-stream dynamic pressure for the Case 1 and Case 2 at 4° angle of attack.....	91
Figure 4.13 CL versus α of the numerical simulations of Case 3, Case 3 Compressible and Case 4 in comparison with Case 1 and the experimental data.	93
Figure 4.14 Contour pressure plots in a cross section plane at the center rib of the canopies along the flow direction for Case 1 and Case 4 at an angle of attack of 4°, normalized by the dynamic pressure.	95
Figure 4.15 CD versus α for the numerical simulations of Case 3, Case 3 Compressible and Case 4 in comparison with the Case 1 and the experimental data.	96
Figure 4.16 Velocity vectors normalized with respect to the free-stream airspeed in a plane located one chord length downstream from the TE of the canopies for Case 1 and Case 4 at an angle of attack of 4°.	98
Figure 4.17 Velocity vectors normalized with respect to the free-stream dynamic pressure in a plane located one chord length downstream from the TE of the canopies for Case 1 and Case 4 at an angle of attack of 4°	100

Figure 4.18 CL versus CD of the numerical simulations of Case 3, Case 3 Compressible and Case 4 in comparison with the Case 1 and the experimental data.	101
---	-----

SYMBOLS

Symbols

a	3D Lift Curve Slope
a_o	2D Lift Curve Slope
a_o'	2D Lift Curve Slope Corrected for Low AR
A	Human Body Frontal Area
A_{Du}	Human Body Surface Area, DuBois Area
A_{ts}	Cross-Section Area of the Test Section
b	Canopy Span Length
c	Rib Chord Length
C_D	3D Drag Coefficient
C_{Dcor}	Corrected 3D Drag Coefficient
C_{Dl}	Suspension Line Drag Coefficient
C_{DO}	Profile Drag Coefficient
$C_{D,i}$	Induced Drag Coefficient
C_{Ds}	Payload Drag Coefficient
CF	Conversion Factor for the Force and Balance Design
C_l	2D Lift Coefficient
C_L	3D Lift Coefficient
C_{Lmax}	Maximum 3D Lift Coefficient
d	Mean Diameter of the Suspension Lines
D	3D Drag Force
D_{ave}	Average 3D Drag Force of Different Tests of a Single Trial
D_{sc}	3D Drag Force for a Scaled Canopy Model
F_1	Vertical Load Cell Force in the Cell Arrangement
F_2	Horizontal Load Cell Force in the Cell Arrangement
H	Human Being Height
k	Correction Factor for Low AR
k_1	Correction Factor for Non-Linear Effects
L	3D Lift Force
L_{sc}	3D Lift Force for a Scaled Canopy Model
L/D	Lift to Drag Ratio
L/D_{max}	Maximum Lift to Drag Ratio
M	Mach Number
n	Number of Suspension Lines
P	Static Pressure
P_{atm}	Atmospheric Pressure
$P_{corrected}$	Corrected Measurement for a Single Load Cell
P_{gauge}	Gauge Pressure
P_{load_cell}	Load Measurement of a Single Load Cell
P_O	Total Pressure
P_{offset}	Offset for a Single Load Cell

P_R	Resultant Force for the Force and Balance Design
q_∞	Free Stream Dynamic Pressure
q_{cor}	Corrected Dynamic Pressure
R	Mean Length of the Suspension Lines
R_{gas}	Specific Gas Constant for Dry Air
Re	Reynolds Number
S	Canopy Planform Area
S_p	Canopy Projected Area in the Cross-Section of the Test Section
T	Ambient Temperature
V	Total Velocity Magnitude
V_{out}	Output Voltage from a Single Load Cell
u	Velocity Component in the x Direction
v	Velocity Component in the y Direction
w	Velocity Component in the z Direction
W	Exit Weight
W_B	Human Body Weight
W/S	Canopy Wing Loading
x	Direction aligned to the x axis
y	Direction aligned to the y axis
z	Direction aligned to the z axis

Greek Symbols

α	Angle of Attack
α_1	Upper Limit for the Opening Inlet
α_2	Lower Limit for the Opening Inlet
α_{cor}	Angle of Attack Corrected
α_{ZL}	Zero Lift Angle of Attack
β	Anhedral Angle
θ	Inclination Angle of the Resultant Force
$k - \epsilon$	K-Epsilon Turbulence Model
$k - \omega$	K-Omega Turbulence Model
γ	Glide Angle
γ_{air}	Ratio of Specific Heats for Dry Air
ρ	Air Density
τ	Oswald Efficiency Factor
μ	Air Dynamic Viscosity

ABBREVIATIONS

2D	Two-Dimensional
3D	Three-Dimensional
AoA	Angle of Attack
AR	Aspect Ratio
CPU	Central Processing Unit
CFD	Computational Fluid Dynamics
CAD	Computer-Aided Design
CG	Center of Gravity
DAQ	Data Acquisition System
DNS	Direct Numerical Simulation
FEA	Finite Element Analysis
FSI	Fluid-Structure Interaction
LE	Leading Edge
LES	Large Eddy Simulation
Ni	National Instruments
PADS	Precision Aerial Delivery System
PC	Personal Computer
RAM	Random-Access Memory
RANS	Reynolds-Averaged Navier-Stokes
SA	Spalart-Allmaras Turbulence Model
SST	Shear-Stress Transport Turbulence Model
TE	Trailing Edge
W&H	Ware & Hassell

NOMENCLATURE

Chordwise Direction	Direction aligned with the canopy chord line
Spanwise Direction	Direction aligned with the canopy span line
Longitudinal Direction	Direction aligned with the chordwise direction
Lateral Direction	Direction aligned with the spanwise direction

ABSTRACT

Christian A. Guzman Zurita MSAE, Embry-Riddle Aeronautical University, May 2019.

Preliminary Test Predictions for Scale Ram-Air Parachute Testing

The present thesis proposes a preliminary analysis to predict the aerodynamic performance for experimental tests of ram-air parachutes in a wind tunnel. A scaled experimental test setup is developed for determining the aerodynamic coefficients of lift (C_L) and drag (C_D) conducted in a wind tunnel. Additionally, a CFD approach where a steady-state parachute shape defined based on experiments, photographs, and literature, is presented. The accuracy of the simulation depends considerably on the ability to resolve the canopy geometry. Therefore, a CAD geometry generation is implemented for flexible control of the canopy structure by implementing design parameters, e.g., chord, span and planform shape. Distortions caused by inflation and suspension line tensions on the canopy structure are simulated by the manipulation of the surfaces in the CAD design. The numerical results compared with experimental data from the literature under similar flow conditions showed good agreement for the values of C_L and a relative constant offset for the values of C_D for the range of angles of attack analyzed. The difference for the values of C_D was attributed mainly to effects of the geometry deformation and suspension lines drag during the experimental tests. Additionally, simulations with a domain size equal to the dimensions of a wind tunnel test section showed an increase of 26% in the lift curve slope and strong wing tip vortices compared to the baseline model because of wall interaction effects. Finally, experimental tests using correction factors to compensate lift and drag measurements are recommended to directly validate the numerical results.

1. Introduction

1.1. Introduction to Ram-Air Parachutes

Parachutes have a wide variety of applications from sky sports to military payload airdrops. Investigations on parachutes during the past decades have led to a ram-air type shape with certain aerodynamic characteristics. This ram-air parachute type is capable of producing higher glide ratios and directional control as compared with traditional airdrop systems, e.g., hemispherical shell type parachutes (Ghoreyshi, et al., 2016). These characteristics make ram-air parachutes feasible for precision aerial delivery and payload recovery (Uddin & Mashud, 2010).

In 1958, Pierre Lemoigne designed one of the first kite-type parachutes with several aerodynamic features and exhaust slots producing a glide ratio close to one (Ghoreyshi, et al., 2016). In 1964, Damina Jalbert's design based on cell divided, triangulated canopy shape, bottom air inlet, and rear outlet slots, was the first parachute that achieved a glide ratio over one (U.S. Washington, DC Patent No. US3131894A, 1964). Contemporary ram-air parachutes follow Jalbert's concept with improvements on the cell dividing canopy structure, air inlets, suspension line arrangement, and payload position. These changes provide larger airdrop altitude ranges, better controlled descend and safe landing. A generic ram-air parachute with suspension lines and payload is shown in Figure 1.1.

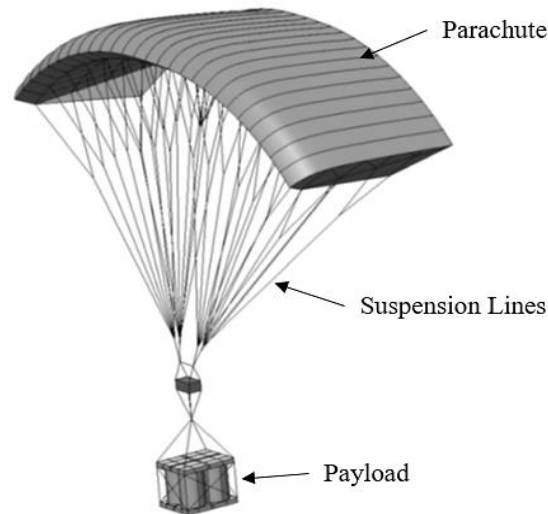


Figure 1.1 Ram-air parachute. Adapted from (Ortega, Flores, & Pons-Prats, 2017).

Ram-air parachutes are made of nonporous nylon fabric to avoid internal pressure losses as well as to provide a smooth-rigid structure when inflated (Lingard, 1995). Similar to an airplane wing, the canopy has ribs along the spanwise direction with an airfoil shape. The ribs divide the structure into several chambers and two consecutive chambers form a cell. Each chamber has an opening cut at the leading edge (LE), letting ram-air inflate the canopy. In addition, the opening cut divides the canopy structure into upper and lower surfaces, which join at the trailing edge (TE) (Fonseca, 2018).

The airfoil shape formed between two ribs is considered as a longitudinal cross section of a canopy and the opening inlet at the LE differentiates the cross-section from a rib. Typical rib designs are based on low speed airfoils with high aerodynamic performance, e.g., CLARK-Y and NASA LS1-0417 (Lingard, 1995). In addition, ribs may have several small hole cuts in the chordwise direction. The purpose of the holes is to maintain a homogenous internal pressure distribution on every cell when the canopy is inflated.

Braided nylon suspension lines connect the canopy and the payload. The bottom

portion of the lines, or primary lines, merge into a single point where the payload is attached. The top portion of each line divides into two or more branches called secondary lines. The group of branches forms a “cascade” of lines, which are sewed to ribs at the bottom surface of the canopy (Lingard, 1995). Additionally, steering lines are placed at the sides to provide maneuverability.

The canopy ribs are classified into loaded and non-loaded, depending if there are lines attached to the rib. On one hand, loaded ribs have the lines sewed to the bottom edge of the rib at different locations along the chordwise direction. Tension forces at these locations keep the rib stretched, ensuring the canopy inflation. Additionally, maneuverability and directional control of the canopy are achieved by applying different tension forces to the lines. On the other hand, the non-loaded ribs do not have lines sewed; hence, the ribs experience a small translation and rotation. As a result of pressure force at the LE of the canopy, the non-loaded ribs tend to translate in the upward direction, perpendicular to the longitudinal axis. Moreover, the non-loaded ribs rotate nose-up between the chord line and longitudinal axis, which creates an angle known as the incidence angle (Fonseca, 2018).

Airflow around a longitudinal cross section and a rib of an inflated canopy behaves similar to an airfoil. Figure 1.2 shows a schematic of the airflow around a cross section of a canopy. Point A represents airflow in the upstream approaching to the LE of the canopy. A stagnation region is formed at point B, close to the LE, as the airflow slows down. Once the canopy is fully inflated, this region behaves as a wall for the opening sections, allowing the canopy pressurization. Additionally, at point B the airflow is redirected towards the upper and lower surfaces of the canopy. Points C and D represent

the upper and lower surfaces of the canopy, respectively. Pressures on both sides of these surfaces, internal and external pressures, maintain the inflated canopy structure. The internal pressures at points C and D are approximately the same because the fluid has negligible motion inside each cell. Moreover, the internal pressures are considerably higher as compared with the external pressures, maintaining the inflation of the canopy. The external pressures at points C and D follow the same behavior as a conventional airfoil, low pressure at the upper surface and high pressure at the lower surface (Sobieski, 1994).

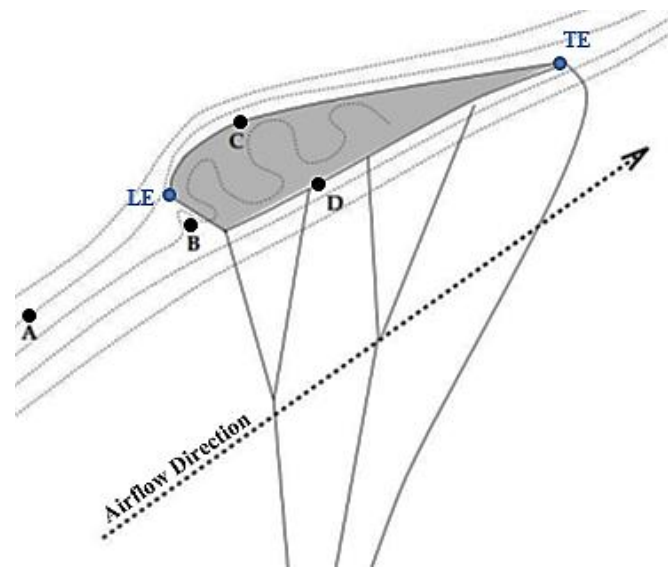
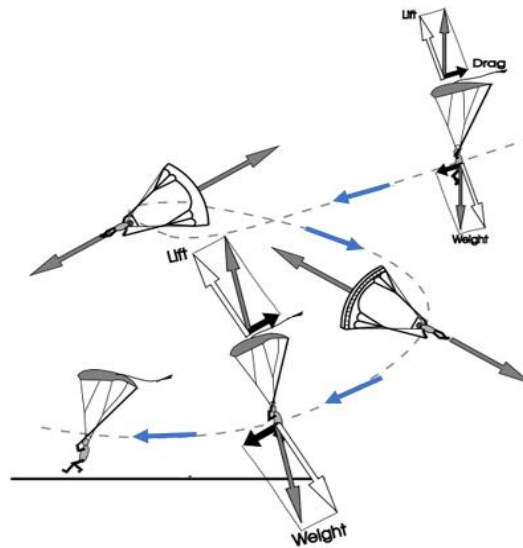


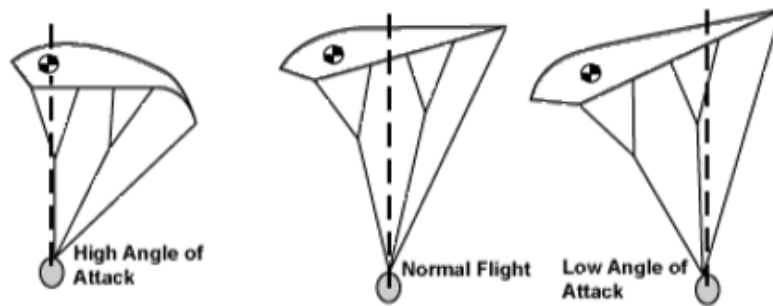
Figure 1.2 Airflow around a canopy cross section. Adapted from (Sobieski, 1994).

Maneuverability, longitudinal and lateral stability of the canopy is highly dependent on the payload position with respect to the canopy center of gravity (CG) (Uddin & Mashud, 2010). Figure 1.3 shows the influence of different positions of the payload on maneuverability and stability of the canopy. Left and right turns are achieved by pulling asymmetrically steering lines and placing the payload at the opposite turning side with respect to the vertical axis. Moreover, the payload tends to move to the left side when the

canopy is turning to the right as shown in Figure 1.3a. Similarly, fore and aft displacements of the payload with respect of the canopy CG modify the angle of attack (AoA). For instance, Figure 1.3b shows the payload location aft the canopy CG inducing a low angle of attack (nose-down).



a) Payload position in a right turn.



b) Payload position with respect to the canopy CG.

Figure 1.3 Schematic of maneuverability and stability of the canopy. Adapted from (McConnel, 2017).

Finally, complex structure designs may include features to increase the canopy performance. For example, pennants or “flares,” stabilizer panels, cross-bracers, and spoilers provide additional support for load distribution and partially channel the flow into a 2D pattern along the chordwise direction of the canopy (Lingard, 1995).

1.2. Motivation for this Study

Aerodynamic performance of ram-air parachutes has been subject of extensive studies during past decades, mainly because of the strong interaction of the airflow with the canopy structure. Starting in the early 60s, prediction of the canopy performance was limited to only experimental and flight tests. Wind tunnel experiments of scaled and full-scaled canopy models have contributed to aerodynamic data under simulated flight conditions. In fact, wind tunnel experiments have been the main source to corroborate tests under similar conditions. However, wall effects and limited range of motion are concerns during the experiments. Expensive and time-consuming flight tests have also provided data, leading mostly to an empirical canopy design approach (Ghoreyshi, et al., 2016).

The accelerated technology growth in the past years has led to numerical approaches of the canopy performance by using different computational tools. Advantages of numerical analysis are the ability to predict fluid parameters, provide flow field visualization, and determine structure displacement and deformation. Although drawbacks of this approach are the high computational time and computer resources needed, numerical analysis provide a full range of outcomes for design criteria, which are very limited with experimental tests. Therefore, the implementation of computational tools provides the parachute industry with a powerful design tool (Fonseca, 2018).

The need to predict the fluid and the structure behavior of canopies has led to the implementation of different types of numerical analysis. For instance, Computational Fluid Dynamics (CFD) analyzes the fluid flow behavior around a rigid body by solving the Reynolds-Averaged Navier-Stokes equations (RANS) in a domain. Similarly, Finite

Element Analysis (FEA) performs a structured analysis by predicting stresses and deformations of a body. Fluid and Structure Interaction (FSI) is a combination of CFD and FEA, which analyzes the interdependence between the fluid flow and the structure of a body (Burnett, 2016). These numerical approaches provide an approximate solution of the canopy performance by providing an understanding of the airflow and structure behavior under simulated flight conditions.

The accuracy of the simulation depends on the ability to resolve the canopy geometry. Computer-Aided Design (CAD) is a computational tool capable of modeling any geometry accurately (Fonseca, 2018). For instance, a canopy can be modeled in a CAD software by using points, lines and surfaces connected to each other by using different constraints. The geometry is later analyzed under fluid flow conditions by CFD software to determine the aerodynamic characteristics.

Although experimental results are used to corroborate numerical solutions under similar conditions, wind tunnel experiments and CFD analysis have been developed independently to study the interaction between the flow field and the canopy. Therefore, implementation of a methodology with a combination of both approaches will determine more accurately the performance of ram-air parachutes.

1.3. Thesis Objectives

The present thesis is a preliminary analysis in advance of wind tunnel experiments by performing CFD analysis of scaled and full-scaled canopy models under similar flight conditions. Based on a full-scaled canopy geometry from the literature, several numerical simulations are assessed and validated to determine the feasibility and accuracy of the results. Additionally, the accuracy of the simulations depends on the ability to resolve the

canopy geometry. Therefore, the thesis has the following objectives:

- Implement a semi-automatic canopy CAD generation tool with interface to CFD using design parameters based from the literature, and to allow inclusion of canopy deformations.
- Evaluate the aerodynamic performance (C_L , C_D and C_L/C_D) of the canopy at various conditions, as well as flow and pressure fields.
- Validate the numerical results with experimental studies, where possible, and determine sources of discrepancy.
- Perform CFD simulations at different Reynolds numbers, domain sizes and angles of attack to determine the feasibility of experiments in a low speed wind tunnel.
- Design, build and calibrate a 2D force balance to determine the components of a resultant load applied at a specific angle.

1.4. Thesis Outline

The present thesis is divided into the following chapters:

- *Chapter 2 Literature Review:* This chapter provides an overall view of the different design parameters and their influence on the performance of the canopies during flight. Additionally, previous results from experimental and numerical analysis as well as different testing methodologies are presented.
- *Chapter 3 CAD Methodology and CFD Approach:* This chapter describes the design parameters and the methodology followed to develop a semi-automatic CAD generation of a canopy and the CFD approach and setup. The chapter begins with an overview of the CAD software used and its capabilities. Additionally, the interface that models different deformations on the canopy when in flight at a

steady state is presented. Finally, the benchmark geometry is defined for the numerical simulations. This chapter also presents an overview of the CFD software used and its capabilities for the numerical analysis. Furthermore, boundary conditions, flow parameters and mesh independence analysis are presented along with the simulation setup. Finally, the test matrix with different scenarios of Reynolds number and domain size is presented.

- *Chapter 4 Results and Analysis:* This chapter starts with the CAD generation interface along with its limitations. Additionally, various canopy models are presented created using the CAD generation methodology. Finally, this chapter presents the computational results, comparison with experimental data from the literature, and a discussion of possible sources of error.
- *Chapter 5 Conclusions and Recommendations:* This chapter summarizes the main outcomes. Additionally, recommendations for future work are provided.

2. Literature Review

2.1. Introduction

Approaches to predict the aerodynamic characteristics of ram-air parachutes are limited because of the high interaction of the fluid flow with the canopy structure. However, the canopy performance can be approximated similar to an airplane wing by using wing theory because of the airfoil shape formed in a cross-section of the canopy when inflated (Uddin & Mashud, 2010). Consequently, geometry characteristics, e.g., airfoil shape, chord (c) and span (b) length have similar effects on the parameters used to determine the parachute design.

2.2. Design Parameters

Designers focus on three main parameters to determine the canopy performance namely planform shape, canopy trim and wing loading (Burke, 1997). These design parameters are closely related to the geometric characteristics and the canopy payload interaction.

Planform shape is defined by the airfoil thickness and aspect ratio (AR) (Burke, 1997). The airfoil thickness is the ratio between the maximum airfoil high and chord length. Parachute industries commonly use a CLARK-Y airfoil shape with a range of 15–18% thickness (Lingard, 1995). Although thick airfoils can provide of large amount of lift, these airfoils have more profile drag coefficient (C_{D0}). Therefore, early canopy designs tend to implement a low-speed airfoil section as a NASA LS1-0417 with a thickness to chord ratio of approximately of 10% (Burke, 1997).

Similar to a finite wing, the aspect ratio (AR) is the ratio between the square of the canopy span and planform area (S), expressed as $AR = b^2/S$. In particular, for a

rectangular planform shape, the aspect ratio is given by $AR = b/c$. Canopies create tip vortices caused by differences of pressure between the upper and lower surfaces, producing induced drag ($C_{D,i}$). This type of drag is inversely proportional to AR , as given in Equation (2.1) for an elliptical planform shape.

$$C_{D,i} = \frac{C_L^2}{\pi AR} \quad (2.1)$$

Therefore, the higher the canopy AR , the less induced drag is produced (Anderson, 2010). Although high wing performance is achieved by increasing the AR , the flexible canopy structure presents several problems. For instance, the higher the canopy AR the less homogenous is the internal pressure within the end cells. Moreover, additional ribs and lines are necessary to maintain a smooth canopy shape, increasing considerably the drag. Therefore, an AR limit of 3 to 1 is commonly found in parachute designs (Burke, 1997).

Longitudinal stability is related with the canopy trim and interaction with the payload. A trimmed canopy locates the payload at the CG of the system to maintain the canopy in equilibrium at a certain angle of attack (Lingard, 1995). For instance, a negative trim angle (nose-down) increases the descent rate and stability. Whereas a positive trim angle (nose-up) increases glide range but the possibilities of canopy collapse (Burke, 1997).

In the same manner, the design trim angle is affected by the length and manipulation of the steering lines. For instance, long or short steering lines limit the ability of the parachutist to maneuver (Burke, 1997). Therefore, parachute designs include lines with very low elasticity (Lingard, 1995).

The design parameter of wing loading (W/S) emphasizes the relation between the payload and the canopy. This parameter is the ratio between the total amount of weight of

the system, also known as exit weight (W), with the planform area of the canopy (Burke, 1997). Therefore, the wing loading has the units of pounds per square foot (lb/ft^2) or kilograms per meter square (kg/m^2) for USCS and SI units, respectively.

The wing loading has a strong influence on the design because of the canopy performance and maneuverability. Variations of exit weight are reflected with changes of air speed around the canopy. For instance, a decrease of the exit weight leads to a slower landing and low maneuverability response. An increase of the exit weight gives a higher descent and turning rate (Burke, 1997). Therefore, the higher the exit weight, i.e., wing loading, for a particular canopy design, the higher the performance and maneuverability (Sobieski, 1994).

Although increasing the wing loading is reflected with a higher canopy performance, excessive increment of wing loading leads to possible flow separation and loss of glide air speed. Therefore, parachute industries have determined ranges of wing loadings depending on the canopy applications and exit weight. For instance, canopies designed for parachutists have typically wing loadings from 0.7 to 1.6 lb/ft^2 (Burke, 1997), while for Precision Aerial Delivery System (PADS) a common range is between 3 to 4 lb/ft^2 (Lingard, 1995).

Planform shape, canopy trim and wing loading provide with an overall layout for the design of the structure and different features of the canopy. Multiple studies have provided empirical or semi-empirical approaches to approximate the influence of the structure on the canopy performance.

2.3. Aerodynamic Characteristics

Lingard provided a compilation of approximations for individual geometry

features to determine the canopy performance. Although lifting line theory provides an approximation for planar wings with an AR higher than 5, various researches have adapted the lifting line theory for wings with an AR lower than 5 (Lingard, 1995).

Starting with the analysis of lifting line theory, the total lift and drag coefficients (C_L and C_D , respectively) for a finite planar wing and general planform shape can be expressed by the Equations (2.2) and (2.3) (Anderson, 2010), i.e.,

$$C_L = \frac{dC_L}{d\alpha} (\alpha - \alpha_{ZL}) \quad (2.2)$$

$$C_D = C_{DO} + \frac{C_L^2}{\pi AR e} \quad (2.3)$$

Where α is the angle of attack, α_{ZL} is the angle of attack of zero lift, C_{DO} is the profile drag, $e = \frac{1}{(1+\tau)}$ is the Oswald efficiency factor and $a = \frac{dC_L}{d\alpha}$ is the lift curve slope per radian (1/rad) for a finite wing given by Equation (2.4), i.e.,

$$a = \frac{\pi AR a_o}{\pi AR + a_o e} \quad (2.4)$$

Where a_o is the lift curve slope of a 2D airfoil shape.

In Equation (2.3), the first term is the profile drag of the airfoil shape, which represents the combination of skin friction and pressure drag of a 2D airfoil (Anderson, 2010). In case of the canopy, the profile drag is produced by the airfoil thickness, irregularities and smoothness of the fabric (Ware & Hassell, 1969). The second term in Equation (2.3) is the induce drag, which represents the 3D effects at the wingtips on a finite wing with a generic planform shape.

An investigation conducted by Hoerner and Borst (1985) provided with a correction factor k for the lift curve slope (a_o) expressed as $a_o' = k a_o$. The investigation proposed that for a low aspect ratio finite wing, the 2D lift curve slope decreases by a factor of k

(Hoerner & Borst, 1985). The value of k is determined with Equation (2.5).

$$k = \frac{2\pi AR}{a_o} \tanh\left(\frac{a_o}{2\pi AR}\right) \quad (2.5)$$

Therefore, implementing the correction factor k into Equation (2.4), the lift curve slope for a low aspect ratio wing is given by Equation (2.6).

$$a = \frac{\pi AR a_o'}{\pi AR + a_o'(1+\tau)} \quad (2.6)$$

Furthermore, the arched shape of the canopy when inflated, also known as anhedral, reduces the lift term from Equation (2.2). The main reason of this decrement is because the lift produced towards the end cells have a component in the lateral direction of the canopy (Fonseca, 2018). The greater the anhedral of the canopy, the higher the lateral component of the lift. Therefore, Hoerner and Borst provide with an approximation of the lift coefficient accounting the anhedral effect as presented in Equation (2.7), i.e.,

$$C_L = a(\alpha - \alpha_{ZL}) \cos^2 \beta \quad (2.7)$$

Where β is the anhedral angle of the canopy.

Additionally, Hoerner and Borst suggested a term for lift and drag to compensate the non-linear effects caused by low aspect ratio, end cells shape, and components of the velocity normal to the wing near the end cells, which are given in Equations (2.8) and (2.9) (Hoerner & Borst, 1985), i.e.,

$$\Delta C_L = k_1 \sin^2(\alpha - \alpha_{ZL}) \cos(\alpha - \alpha_{ZL}) \quad (2.8)$$

$$\Delta C_D = k_1 \sin^3(\alpha - \alpha_{ZL}) \quad (2.9)$$

Where k_1 is a correction factor from experimental data presented as follows:

$$k_1 = 3.33 - 1.33AR \quad 1 < AR < 2.5$$

$$k_1 = 0 \quad AR > 2.5$$

The influence of suspension lines and payload on the overall drag is significantly.

Thus, different semi-empirical approaches provide approximations for the contribution of these features (Lingard, 1995). For instance, Lingard presents an approximation to the drag coefficient because of the suspension lines, expressed in Equation (2.10), assuming a constant line length and inclination angle with respect to the airflow velocity, i.e.,

$$C_{Dl} = \frac{nRd\cos^3\alpha}{S} \quad (2.10)$$

Where R is the average line length, d is the diameter, and n is the total number of lines.

In the same manner, the payload is estimated by approximating size dimensions and the surface area of the body. Research by Mkrtchyan and Johari suggests a semi-empirical relation to estimate the drag force for a standing human body. This is done by approximating the surface and frontal area, as presented in Equations (2.11) and (2.12), i.e.,

$$A_{Du} = 0.0769W_B^{0.425}H^{0.725} \quad (2.11)$$

$$A \approx 0.35A_{Du} \quad (2.12)$$

Where A_{Du} is the DuBois or surface area, W_B is the weight in Newtons, H is the height in meters, and A is the frontal area of a human body in squared meters. Additionally, the investigation provides from experimental tests the drag coefficient with respect to the front area of the human body as $C_D = 1.17$ (Mkrtchyan & Johari, 2011). Therefore, the drag coefficient estimated for a human body with respect to the canopy area can be expressed in Equation (2.13), i.e.,

$$A C_D = 1.17 A$$

$$A C_D = 1.17 A_{Du} \frac{A}{A_{Du}}$$

$$A C_D = (0.35)(1.17) A_{Du}$$

$$C_{Ds} = \frac{A C_D}{S} = (0.35)(1.17) \frac{A D u}{S} \quad (2.13)$$

The aerodynamic characteristics of the system can be estimated by implementing the effects of different geometric features. Therefore, the overall lift and drag coefficients may be writing as Equations (2.14) and (2.15) (Lingard, 1995), i.e.,

$$C_L = a(\alpha - \alpha_{ZL})\cos^2\beta + k_1\sin^2(\alpha - \alpha_{ZL})\cos(\alpha - \alpha_{ZL}) \quad (2.14)$$

$$C_D = C_{D0} + C_{Di} + C_{Ds} + \frac{C_L^2}{\pi A R e} + k_1\sin^3(\alpha - \alpha_{ZL}) \quad (2.15)$$

Where the C_L for the induced drag in Equation (2.15) is given by Equation (2.2).

The aerodynamic efficiency of the canopy is referred to the lift to drag ratio (L/D) produced as the canopy descends (Anderson, 2010). At steady level flight, the canopy descends at a constant rate, where the airspeed and L/D are given by Equations (2.16) and (2.17) (Lingard, 1995), i.e.,

$$V = \left(\frac{2W}{\rho S} \frac{1}{(C_L^2 + C_D^2)^{0.5}} \right)^{0.5} \quad (2.16)$$

$$\frac{L}{D} = \frac{C_L}{C_D} = \frac{1}{\tan(\gamma)} \quad (2.17)$$

Where ρ is the air density and γ is the glide angle.

Finally, the horizontal and vertical components of the airspeed are given by the following equations (Lingard, 1995),i.e.,

$$u = V\cos(\gamma) \quad (2.18)$$

$$v = V\sin(\gamma) \quad (2.19)$$

2.3.1. Distortions on the Canopy Structure

Although the canopy resembles an airplane wing when inflated, flexibility of the fabric leads structure distortions caused by the surrounding fluid pressure and tension forces from the suspension lines. Distortions on the structure produce effects such as

airflow channel, flow separation and fabric displacements, modifying the flow pattern over the surfaces of the canopy. Therefore, distortions have a strong influence in the aerodynamic performance of the canopy, which has been subject of extensive studies within the past decades.

Figure 2.1 presents an underside view of a canopy when in flight. The canopy structure experiences an inflation effect caused by the air pressure inside each cell. For instance, the top and bottom surfaces tend to curve in between the ribs, as indicated with blue arrows in Figure 2.1, creating channels where the ribs are sewed along the chordwise direction. Moreover, the seams along the spanwise direction and the attachments of the suspension lines create multiple bulges at the top and bottom surfaces of the canopy, as indicated with red arrows in Figure 2.1. These irregularities are increased when the parachutist exerts tension on the steering lines.

Additionally, the inflation of the canopy increases substantially the thickness of the canopy cross-section, i.e., the airfoil shape in between the ribs. The stretch of the fabric in the vertical direction decreases the canopy span length, causing a reduction of the total lift produced (Fonseca, 2018).



Figure 2.1 Underside view of an inflated ram-air parachute (Adapted from Tactical Parachute Delivery Systems Inc., retrieved from <http://tpdsairborne.com/products/parachutes/hlt-r/>)

Figure 2.2 shows rear view of a canopy when in flight, where the internal pressure of the cells stretches the fabric at the trailing edge, forming a round shape between the ribs where the seam joins the top and bottom surfaces of the canopy, as shown with the red circle.



Figure 2.2 Rear view of an inflated ram-air parachute (Adapted from Air Freshener, retrieved from <https://airfreshener.club/quotes/ram-air-parachute-dimensions.html>)

Similar to a blunt body, the round shape at the TE produces flow separation causing pressure drag. Additionally, tension forces on the steering lines to maintain maneuverability and stability causes deflections near the TE, as shown with the blue circle in Figure 2.2. Finally, Figure 2.3 shows deformations at the opening inlet and the displacements of the canopy ribs.

As explained in the previous chapter, the ribs can be classified as loaded and non-loaded ribs, depending if there are lines sewed at the bottom edge of the rib. Therefore, tension forces on the suspension lines cause the loaded ribs to maintain their position, as shown by the red arrow in Figure 2.3. Whereas the non-loaded ribs would experience a displacement in the upward direction perpendicular to the longitudinal axis, as shown by the yellow arrow in Figure 2.3. Additionally, the internal pressure exerted over the upper and lower surfaces of the canopy stretches the ribs, causing the non-loaded ribs to move in the upward direction perpendicular to the longitudinal axis.

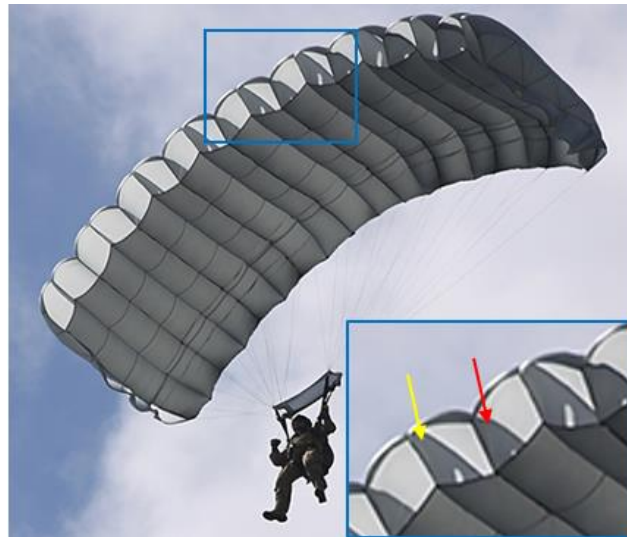


Figure 2.3 Rib displacement and opening section of a ram-air parachute (Adapted from Tactical Parachute Delivery Systems Inc., retrieved from <http://tpdsairborne.com/products/parachutes/hlt-r/>)

Finally, the ram air at the LE causes pressure force at the upper and lower lips of the opening sections, pushing aft the lips and forming a round shape at the LE, as shown in Figure 2.3. Additionally, the pressure forces on the upper lip of the opening section induce the non-loaded ribs to rotate nose-up between the chord line and longitudinal axis.

Although the canopy resembles into a low AR wing when inflated, performance analysis using Prandtl lifting-line theory is limited in this case because of the arched shape of the canopy (Belloc, 2015). Research conducted by Iosilevskii (1996) showed an extension of the lifting line theory for arched wings, by applying Prandtl's theory if the wing sweep angles were small enough. In his investigation, Iosilevskii demonstrated that the lift distribution is similar for an arched wing as compared with a planar wing with similar geometry characteristics, e.g., chord and span length (Iosilevskii, 1996). Additionally, Iosilevskii indicates that an arched wing will produce less lift towards the tips of the canopy as compared to planar wings. Therefore, extensive experimental studies have analyzed the canopy performance with the intention of validating analytical and computational approaches.

2.4. Experimental Studies

For decades, wind tunnel experiments have provided data under simulated flight, becoming a reliable source and cost-effective tool to predict the aerodynamic performance of ram-air parachutes (Barber & Johari, 2001). Investigations conducted by Nicolaidis (1971), Ware & Hassell (1969), Belloc (2015), Uddin & Mashud (2010), Barber & Johari (2001), Lee & Li (2007) and Carney (2007) have concentrated their attention on predicting the in flight geometry and the aerodynamic performance of sub-scaled and full-scaled canopy models. Furthermore, different experimental techniques

have led to a wide range of simulated flight conditions such as flow velocities, angles of attack and canopy aspect ratios.

Early in 1964, Nicolaidis conducted experimental tests of scaled and full-scaled canopy models under different conditions to determine the aerodynamic performance, longitudinal and lateral stability of ram-air parachutes. The tests included several rigid, semi-rigid and flexible rectangular canopies with aspect ratios ranging from 0.5 to 3.0. Additionally, test conditions consisted of airspeed range from 20 ft/s to 60 ft/s and angles of attack from 0° to 25° (Nicolaidis, 1971). The tests were performed in two subsonic wind tunnels: University of Notre Dame and NASA Langley Full Scale wind tunnel. Several rigid and semi-rigid scaled canopy models were tested at the University Notre Dame wind tunnel, which has a rectangular test section of 2 ft x 2ft and 6 ft long. Figure 2.4 shows a schematic of the experimental set-up for the rigid wings.

During the tests, the models were suspended on a force and balance system in the yaw plane, i.e., vertically to avoid the influence of the gravity on the measurements, using two rods that allowed the change of angle of attack (Nicolaidis, 1971). Additionally, two cameras were placed at the bottom and top of the test section to record the angular motion and the angle of attack, respectively, as shown in Figure 2.4.

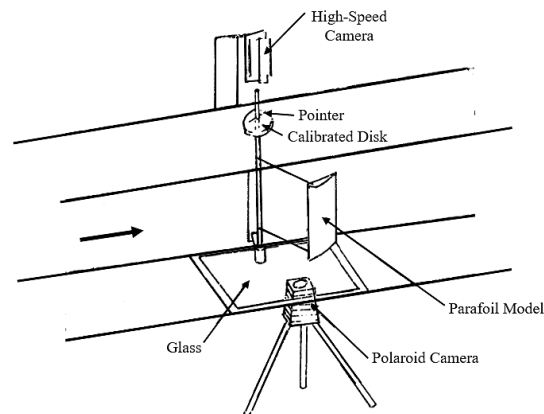


Figure 2.4 Notre Dame experimental set-up. Adapted from (Nicolaidis, 1971).

The flexible models were tested at NASA Langley Full Scale wind tunnel, which had an elongated hole test section of 30 ft x 60 ft and 56 ft long. Figure 2.5 presents an overall view of the NASA Langley wind tunnel.

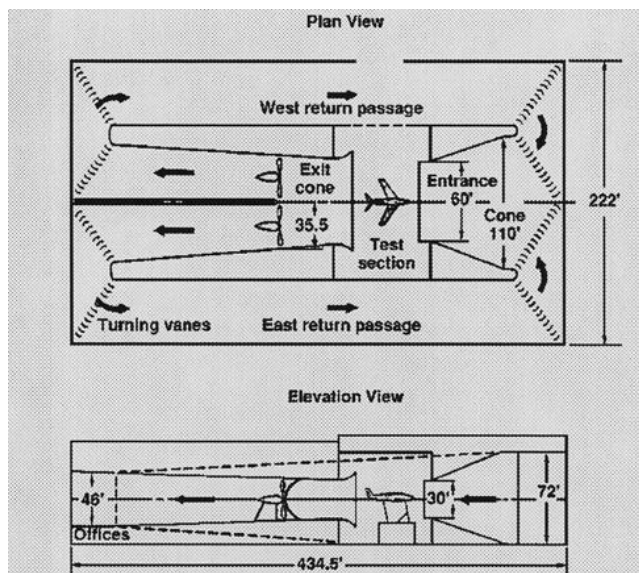


Figure 2.5 NASA Langley wind tunnel schematic (Adapted from National Aeronautics and Space Administration, retrieved from <https://www.nasa.gov/centers/langley/news/factsheets/30X60.html>)

The canopy models were tested using two different methods, namely tether and center-post, which provide with measurements of the aerodynamic characteristics, as well as the longitudinal and lateral stability. The tether method consisted on attaching the canopy model to a force balance using suspension lines. Figure 2.6 presents a schematic of the set-up for a tether test. Notice that testing equipment placed upstream, e.g., as the floor of the test section, covered a certain length of the lines, affecting the drag measurements. Therefore, Nicolaides presented an empirical correction factors to approximation the drag of the unexposed lines. Additionally, the canopy was placed in the centerline of the test section using “guide” lines, which were released once the canopy was inflated (Nicolaides, 1971). A photograph was taken from the side of the wind tunnel to

determine the angle of attack (Nicolaidis, 1971).

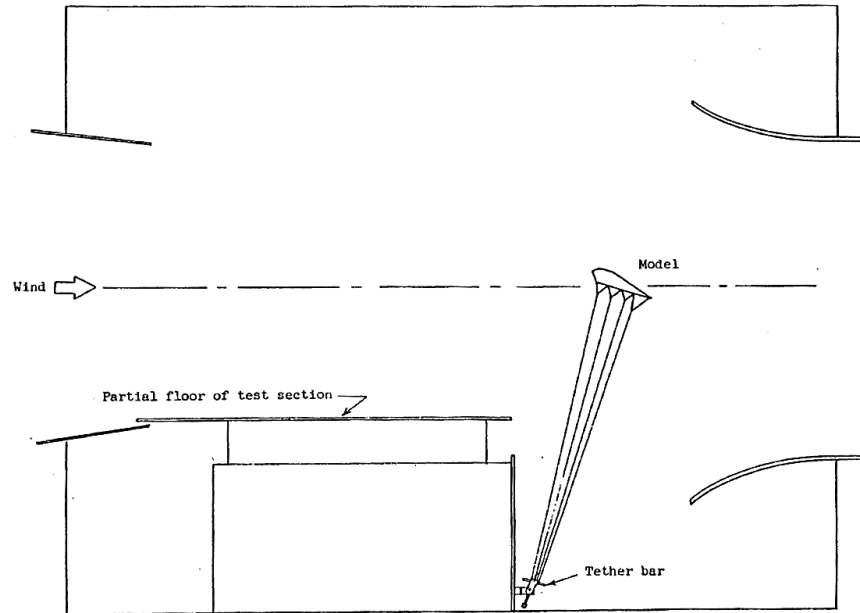
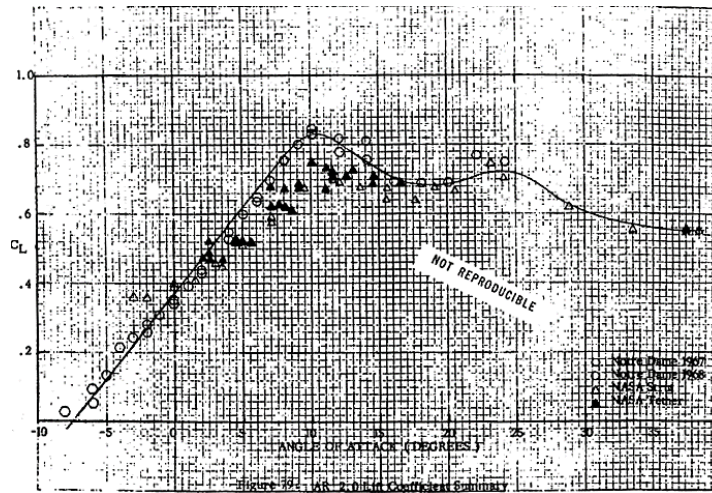


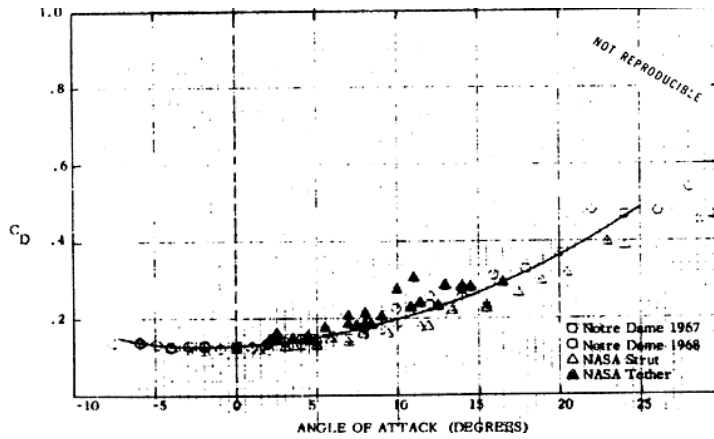
Figure 2.6 Tether test schematic set-up. Adapted from (Ware & Hassell, 1969).

The center-post test, also known as strut test, consisted on connecting the suspension lines to a metal grid framework. Therefore, a portion of the lines was cut to maintain the canopy in the centerline of the test section. The grid was connected to a strut mounting system with various strain gages at the base of the mounting to measure the forces and moments. Finally, previous tests were performed with the grid and the mounting to calibrate the system (Nicolaidis, 1971).

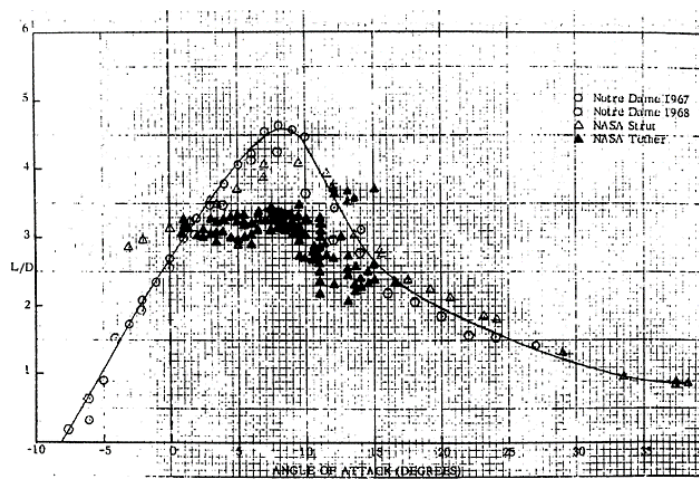
Results of the investigation showed that the lift curve was approximately linear for a large range of angles of attack, from 7.5° to 15° , with maximum lift coefficients ($C_{L\max}$) from 0.751 to 1.005. Moreover, the lift curve slope of a cross-section of the canopy was lower as compared with a 2D conventional airfoil section. Figure 2.7 shows the C_L , C_D and C_L/C_D versus α for a rectangular flexible canopy with AR of 2 and 8.57 ft chord length.



a) C_L versus α .



b) C_D versus α .



c) C_L/C_D versus α .

Figure 2.7 C_L , C_D and C_L/C_D versus α for a rectangular canopy with AR of 2. Adapted from (Nicolaidis, 1971).

The maximum lift to drag ratio (L/D_{\max}) ranged from 1.83 to 6.40. The experiments also showed that the canopies did not maintain steadiness because of the downstream location of the tether mounting, leading flow disturbances at the rear part of the test section affect the canopy stability and performance (Nicolaidis, 1971).

A similar investigation conducted by Ware and Hassell (W&H) in 1969 determined the aerodynamic characteristics and stability of ram-air parachutes under simulated flight conditions. The experiments consisted of wind tunnel experiments of eleven flexible canopy models: five models with constant-wing area, five models with constant-wing chord and one full-scale canopy model. The aspect ratio for the canopies of constant-wing area and constant-wing chord ranged from 1.0 to 3.0, whereas for the full-scale canopy the aspect ratio was 1.5. Additionally, the tests included different airspeeds between 30 ft/s to 60 ft/s along with different angles of attack.

In the same manner, the experiments were tested at NASA Langley Full Scale wind tunnel using the tether and center-post methods. During the tests, photographs taken from the side of the test section were used to determine the angle of attack. Additionally, visual inspection determined that there was no twist angle towards the end cells of the canopy. Therefore, the angle of attack seen by the side rib was assumed for the overall canopy (Ware & Hassell, 1969).

Results of the experiments showed the significantly influence of the suspension lines on drag measurements, e.g., for a canopy with aspect ratio of 3 the drag presented a difference from 28% to 41% for the constant-chord and constant-area series, respectively. Additionally, the maximum lift to drag ratio of the canopy alone ranged from 2.7 to 4.4 as the aspect ratio increased from 1.0 to 3.0. The experiments determined that the

maximum lift to drag ratio of the canopy was lower compared with a rigid wing with a conventional airfoil shape. The low lift to drag ratio is associated with multiple drag effects caused by the opening inlet and the suspension lines. Figure 2.8 shows the C_L versus α and the drag polar for a rectangular canopy with AR of 2 and a chord length of 8.57 ft.

Finally, Ware and Hassell mentioned that the equipment used during the experiments had no interference effects with the testing model. Therefore, the data presented had no wind-tunnel jet-boundary corrections applied (Ware & Hassell, 1969).

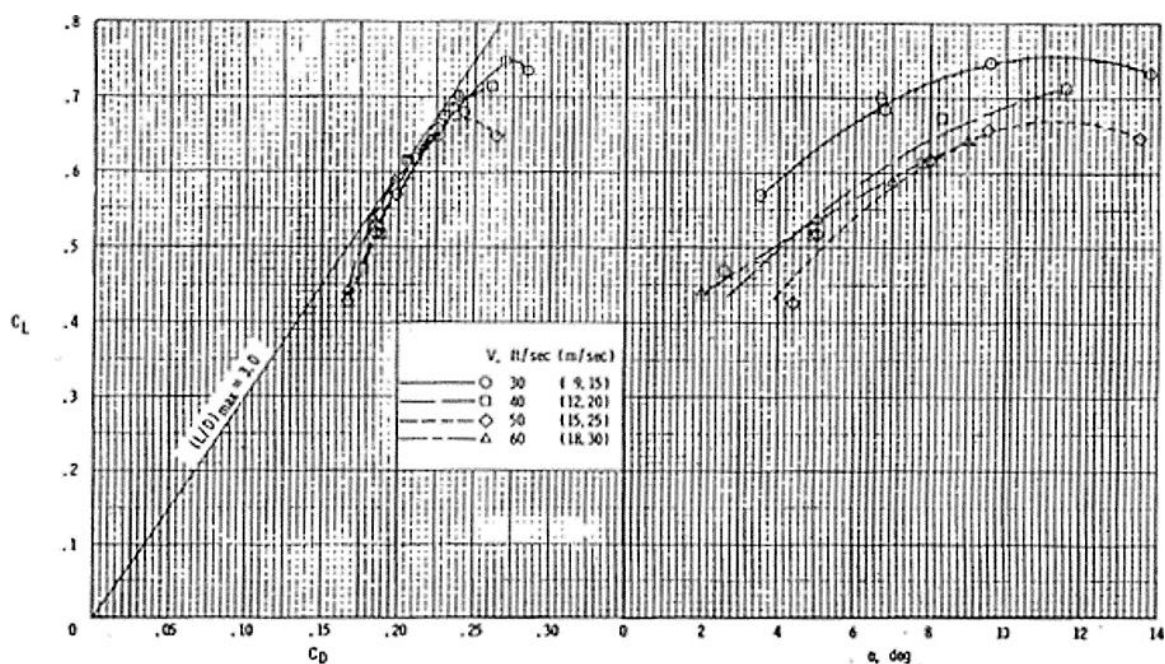


Figure 2.8 C_L versus α and drag polar for a rectangular canopy with AR of 2. Adapted from (Ware & Hassell, 1969).

Experiments conducted by Belloc in 2015 with a rigid arched wing demonstrated the effects of a spanwise arched shape in the longitudinal and lateral stability. The wing, which had a NACA 23015 airfoil shape in cross-section, was tested in an elliptical open test section of 9.8 ft x 6.6 ft (3 m x 2 m) at an airspeed of approximately 131 ft/s (40 m/s).

Additionally, the arched wing had a central chord length of 9.2 ft (2.8 m) and an AR of 6.52. The wing was placed at the centerline of the test section on top of a dynamometer, leaving a distance of 1.6ft (0.5m) from the wingtips to the walls. Figure 2.9 shows the experimental set-up and the location of the rigid canopy in the wind tunnel.

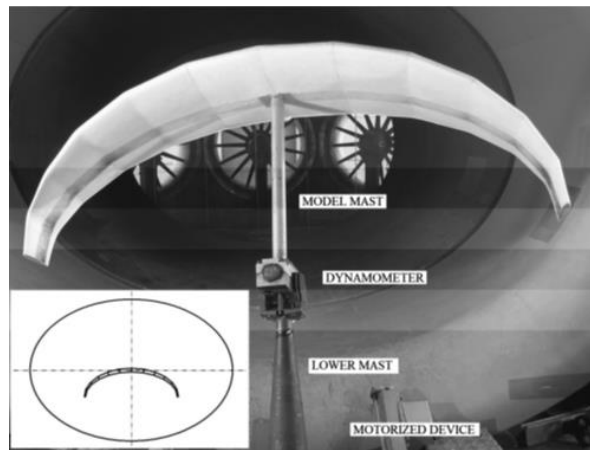


Figure 2.9 Rigid arched wing experimental set-up. Adapted from (Belloc, 2015).

Belloc implemented correction factors to the angle of attack and coefficient of drag for a flat wing with the same projected area as to correct the effects of wind on the dynamometer measurements, given by Equations (2.20) and (2.21) (Belloc, 2015), i.e.,

$$\alpha_{cor} = \alpha - 0.71C_L \quad (\text{deg}) \quad (2.20)$$

$$C_{Dcor} = C_D - 0.012C_L^2 \quad (2.21)$$

Additionally, Belloc mentioned that the half-scale Reynolds number of 9.6×10^5 obtained for the tests was high enough to expect a similar boundary layer behavior, with spanwise lift and induce drag distributions as compared with the full-scaled model conditions. According to Belloc, effects of low Reynolds number affected measurements of the friction drag and $C_{L \max}$.

Results of the investigation showed the presence of lateral force because of the lift generated at the arched sides of the wing. Additionally, the lift curve remained linear for

angles of attack up to 16° approximately with a $C_{L\max}$ of 0.8 for a sideslip angle (β) of 0° . Figure 2.10 shows the C_L and C_L vs C_D for the multiple angles of attack tested.

Finally, the lateral forces and lift produced in the arched wing induce pitch down, yawing and rolling stable effects (Belloc, 2015).

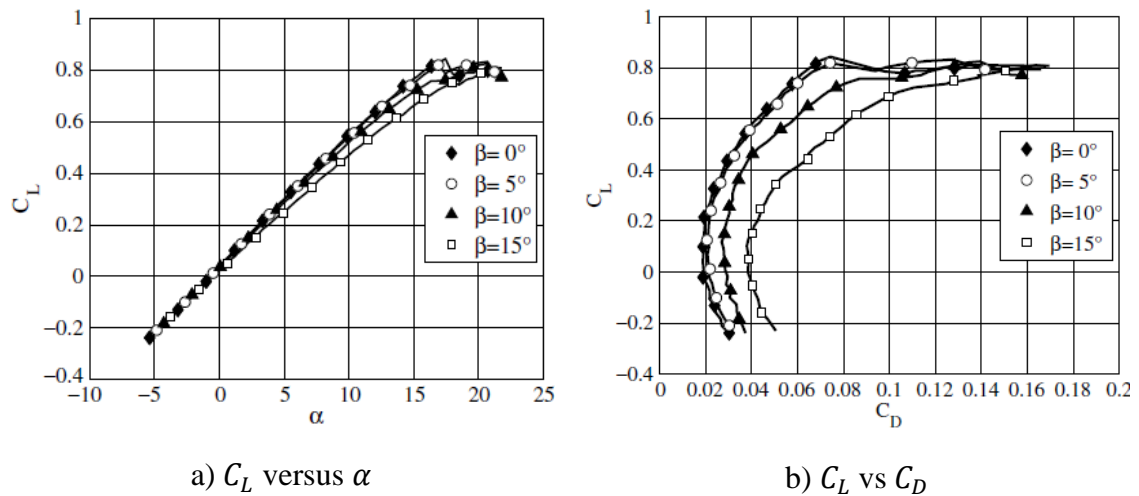


Figure 2.10 C_L and C_L vs C_D for experimental tests of a rigid arched wing. Adapted from (Belloc, 2015).

Uddin and Mashud (2010) performed pseudo 2D experimental tests measuring the internal and external pressure of a single canopy chamber. The tests were conducted at various Reynolds numbers and angles of attack at the wind tunnel of Khulna University, which had a test section of 0.34 m x 0.40 m x 0.985 m. The model consisted of 0.002 m thick acrylic ribs, a simplified opening inlet geometry and different fabric materials for the upper and lower surfaces, allowing deformations along the chordwise direction.

Figure 2.11 shows a schematic of the experimental set-up for the pseudo 2D canopy test.

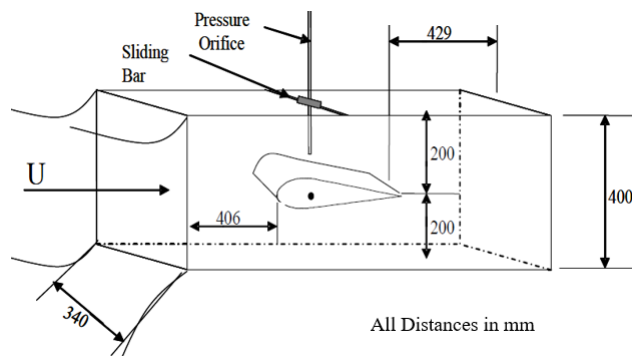


Figure 2.11 Schematic of an experimental set-up for a pseudo 2D test. Adapted from (Uddin & Mashud, 2010).

The pressure distribution was measured using a pressure port mounted on a mechanical transverse system. Additionally, the upper and lower data points were located at the center of the chamber along the chordwise direction to avoid 3D flow effects. Figure 2.12 shows the variation of the internal pressure of the chamber when increasing the angle of attack.

The experimental results showed that the internal pressure was approximately constant for high angles of attack maintaining the chambers inflated, as shown for angles of attack higher than 10° in Figure 2.12. For low angles of attack the leading edge of the chamber tended to collapse preventing the ram-air enter to the chamber. The main reason of this effect was attributed to the location of the simplified opening inlet at the leading edge and the ram-air necessary to inflate the chamber.

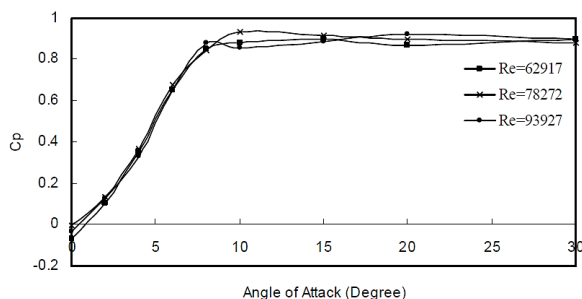
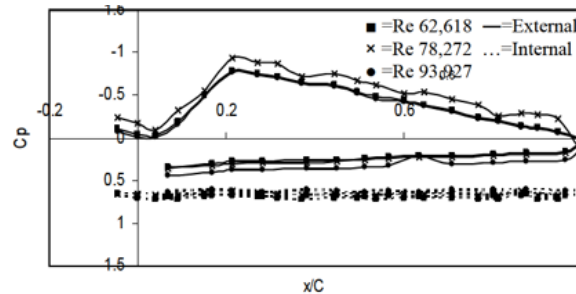
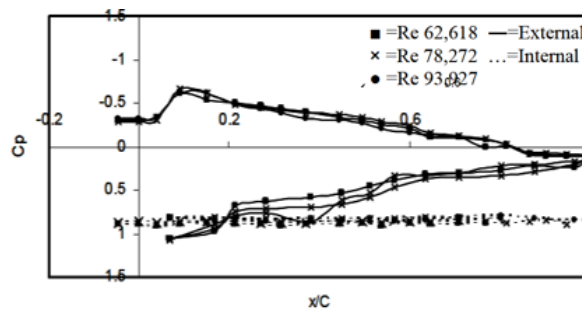


Figure 2.12 Variation of internal pressure with angle of attack of a pseudo 2D experimental test. Adapted from (Uddin & Mashud, 2010).

Figure 2.13 presents the external and internal pressure distribution for 6° and 20° angle of attack. Additionally, the investigation concluded that changes of Reynolds number did not have major effects on the external pressure distribution of the chamber as compared with the angle of attack effect, as shown in Figure 2.13.



a) Pressure distribution for 6° angle of attack.



b) Pressure distribution for 20° angle of attack.

Figure 2.13 Internal and external pressure distribution of a pseudo 2D experimental test. Adapted from (Uddin & Mashud, 2010).

In 2001, Barber and Johari conducted experimental tests on hemispherical shape parachutes to determine the influence of the fabric porosity and canopy geometry on the steady-state stability and drag generated. The experiments were performed at the Worcester Polytechnic Institute wind tunnel, whose test section had 2 ft x 2 ft and 8 ft long. The flow conditions varied with airspeeds from 6 m/s to 17 m/s, corresponding to Reynolds numbers from 200,000 to 500,000.

The authors emphasized the importance of proper scaling parameters such as Reynolds numbers and correction factor because of the porosity of the fabric. Additionally, the authors analyzed an increment of the dynamic pressure near the tested body inside the test section caused by wall effects. Therefore, the investigation implemented Maskell's empirical correction equation for the dynamic pressure given by Equations (2.22) and (2.23), i.e.,

$$q_{cor} = q_{\infty} \left(1 + 1.85 \left[\frac{C_D S_p}{A_{ts}} \right] \right) \quad (2.22)$$

$$C_D S_p = \frac{D_{ave}}{q_{\infty}} \quad (2.23)$$

Where q_{∞} is the free stream dynamic pressure with no correction, C_D is the drag coefficient of the canopy, A_{ts} is the cross-section area of the wind tunnel, S_p is the projected area of the canopy in the cross-section of the test section and D_{ave} is the average drag of all the tests of the same trial.

Equations (2.22) and (2.23) are applicable mainly to bluff bodies, e.g., circular and conical canopies, for a blockage area up to 22%, where the wall effects start to influence on the canopy geometry (Macha & Buffington, 1990).

An investigation conducted by Lee and Li presented a 3D scanning methodology to determine the geometry of different scaled model parachutes, including round, ring-slot and parafoil parachutes. The experiments were performed at the Tropic Climatic Chamber at the NSC, whose test section had 15 ft x 11 ft and 22 ft long (4.6 m x 3.3 m x 6.7 m). Additionally, the flow conditions for all the experiments were: Reynolds number of 447,000 with an airspeed of 22 ft/s (6.7 m/s) at 70°F approximately.

The experiments consisted on inflating the canopy vertically in a frame using suspensions lines. Additionally, for scanning purposes, the parachutes were maintained

stable using lines attached to the corners of the canopy. The scanning apparatus consisted on four scan heads placed diagonal to each other, which emitted a laser light, allowing the triangulation of the light on the canopy surface (Lee & Li, 2007). Figure 2.14 shows the experimental set-up for the geometry scanning of an inflated canopy model.

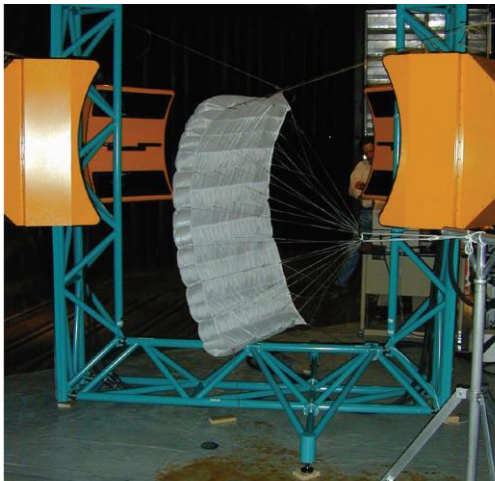
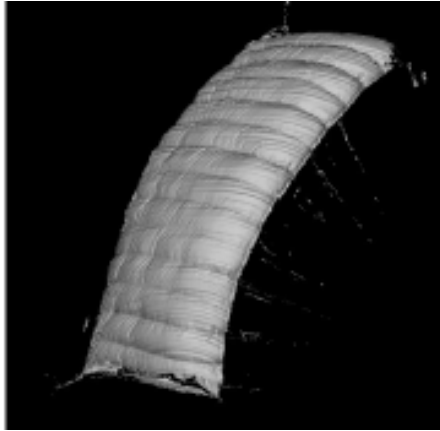
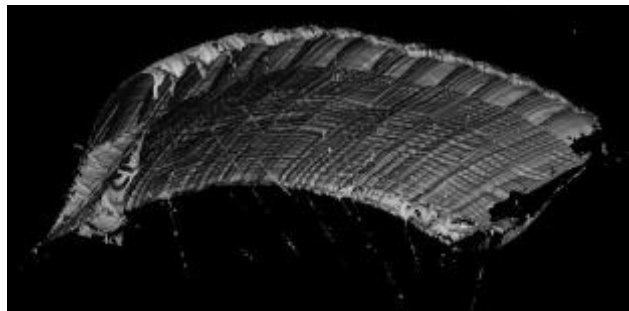


Figure 2.14 Experimental set-up for laser scanning of an inflated canopy model. Adapted from (Lee & Li, 2007).

Figure 2.15 shows 3D scan views of the canopy geometry when inflated, displaying the different distortion on the upper and lower surfaces along with trailing edge deflections. Notice the round shape and the multiple bulges created at the top surfaces along the spanwise direction of the canopy in Figure 2.15a. Moreover, the canopy presents an airfoil shape as a cross-section when inflated, as shown in Figure 2.15b. Lee and Li concluded on the feasibility of implementing a 3D scanning to determine the flexible geometries and deformation of canopy models when in flight.



a) Top view of the canopy inflated



b) Bottom view of the canopy inflated

Figure 2.15 3D Scan views of the canopy inflated. Adapted from (Lee & Li, 2007).

In 2007, Carney conducted multiple structural tests on F1-11 nylon fabric, low porosity parachute material, to determine the strain and deformation under different load conditions. Additionally, a photogrammetry test was performed using a 3D image correlation system capable to determine a 3D shape and displacements, along with in-plane and out of plane strains of a body (Carney, 2007). The experiments concluded that the 3D correlation system was capable to record shape and deformation measurements of a field of view (Carney, 2007). Finally, the experiments provided strain and deformation data to validate FEA and CFD analysis.

Experimental investigations of a wide variety of canopy models have contributed with data to predict accurately the aerodynamic characteristics, stability and geometry of

inflight ram-air parachutes. However, the high cost, time consuming, interference effects and physical limitations to set-up the experiments have led to numerical approaches. For instance, numerical analysis such as CFD and FSI present new tools, e.g., fluid flow and pressure field plots for better understanding of the canopy performance.

2.5. Computational Studies

Numerical approaches have provided multiple analysis to determine the aerodynamic performance of parachutes under simulated flight conditions, complementing the different outcomes from experimental tests. For instance, analysis such as CFD, FEA and FSI have been conducted for the last two decades providing reliable approximations of the fluid flow and the canopy structure, starting from a 2D to a 3D approach analysis. Therefore, investigations from Mohammadi & Johari (2010), Ghoreyshi et al. (2016), Fonseca (2018), Fogell (2014), Burnett (2016), Peralta & Johari (2015), and Ortega et al. (2017) have focused on performance analysis and structure behavior for different flight scenarios.

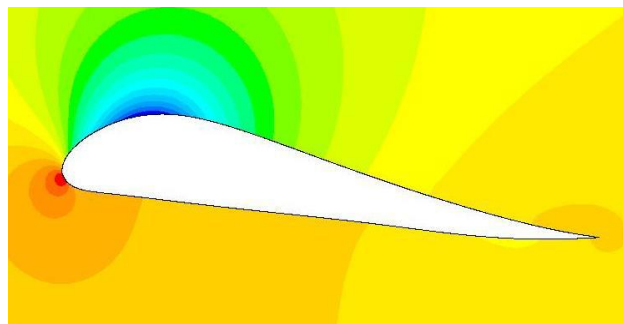
Mohammadi and Johari conducted a 2D CFD analysis of a rib and a cross-section of a canopy to determine the effect of the opening inlet on the aerodynamic characteristics. The computational analysis solved the RANS equations along with Spalart-Allmaras (SA) as turbulence model. Additionally, the analysis applied boundary conditions, such as no-slip condition for the airfoil edges, free-slip condition for the wall domains, uniform inlet velocity and no viscous stresses at the outlet.

A mesh independence study was performed using a CLARK-Y at a Reynolds number of 500,000 to determine the domain size necessary to prevent differences on the results. The lift and drag coefficients were within the uncertainty of the experimental data, using

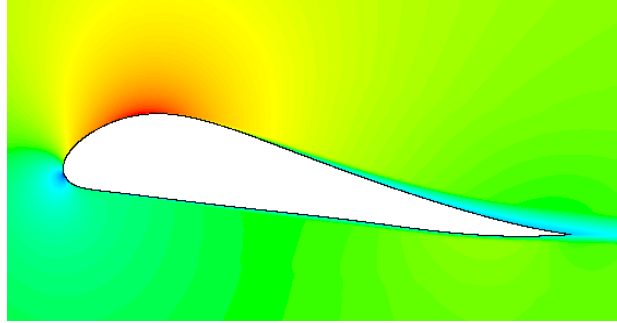
a domain with the following sizes: 5 chords lengths upstream, 11 chords length downstream and 10 chords length in the transverse direction (Mohammadi & Johari, 2010). Additionally, the mesh for the airfoil consisted on a structure form with a thick boundary layer mesh. Whereas for the cross section airfoil, the mesh consisted on an unstructured form with a thin boundary layer mesh.

The simulations were conducted using a baseline airfoil model for angles of attack ranging from -3.5° to 14.5° and three different freestream velocities: 31, 49 and 69 ft/s (9.4, 15 and 20.9 m/s). Moreover, the airfoils were assumed rigid, with smooth edges and no porosity (Mohammadi & Johari, 2010). Figure 2.16 shows the pressure field and the velocity magnitude around the baseline airfoil model for 7° angle of attack.

The results showed that there was high pressure at the LE of the airfoil, denoted by the red region in Figure 2.16a, causing the flow to decelerate, as shown by the blue region in Figure 2.16b. Similarly, there was a low pressure at the top edge of the airfoil causing high flow velocity.



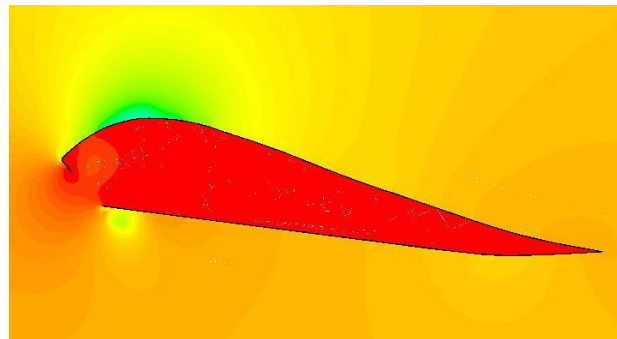
a) Pressure field.



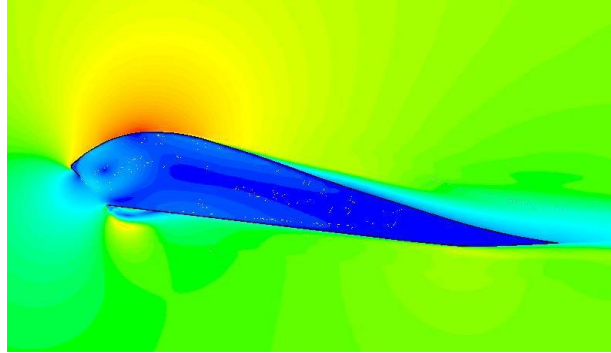
b) Velocity magnitude.

Figure 2.16 Pressure field and velocity magnitude around the baseline airfoil model for 7° angle of attack. Adapted from (Mohammadi & Johari, 2010).

Figure 2.17 shows the pressure field and the velocity magnitude around a cross section airfoil for 7° angle of attack. The results showed that there was high internal pressure, maintaining low flow velocity. Additionally, a stagnation wall was created at the opening inlet, redirecting the flow towards the upper and lower edges, causing pressurization and inflation of the cross section airfoil. Moreover, there was a low-pressure region at the top edge of the cross section airfoil causing high velocity magnitude.



a) Pressure field.



b) Velocity magnitude.

Figure 2.17 Pressure field and velocity magnitude around the cross section airfoil model for 7° angle of attack. Adapted from (Mohammadi & Johari, 2010).

Figure 2.18 shows the vorticity contours of the baseline and the cross section airfoil models for 7° angle of attack. The results showed the boundary layer effects especially at the TE of the baseline airfoil model, as shown in Figure 2.18a. The cross section airfoil model presented more evident flow separation at the TE, as shown in Figure 2.18b. Additionally, the low velocity inside the cross section model caused several vortices, as shown near the LE. Finally, a flow separation bubble and flow reattachment was noticeable at the bottom lip of the opening inlet of the cross section model.



a) Vorticity contour for baseline model



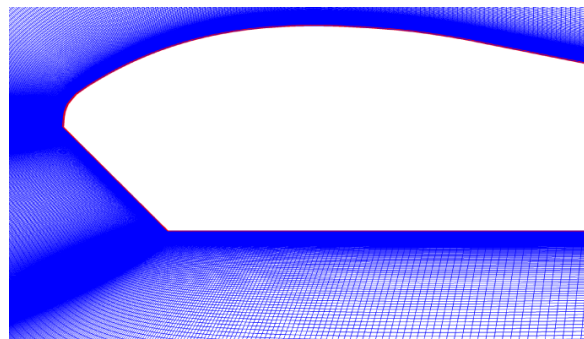
b) Vorticity contour for cross section model

Figure 2.18 Vorticity contours for the baseline and cross section airfoil models for 7° angle of attack. Adapted from (Mohammadi & Johari, 2010).

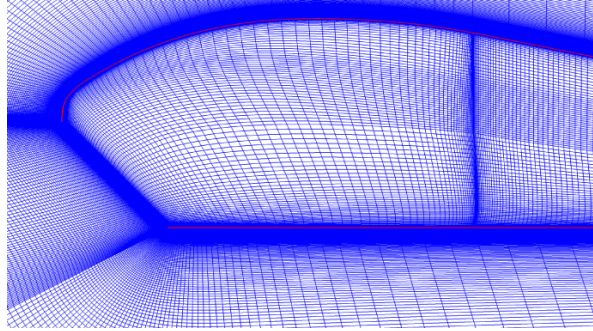
Although the lift coefficient showed a linear increment for the cross section model, the lift curve slope showed a decrement of 8% compared to the baseline model for the range of 2.5° to 8.5° angles of attack. This effect was attributed to the velocity and pressure variations because of the opening inlet. Additionally, the lift curve presented a stall angle of 8.5° . Finally, the opening inlet affected the drag significantly because of a bluff leading edge shape, producing twice the amount of drag as compared to the baseline model (Mohammadi & Johari, 2010).

Ghoreyshi et al. (2016) conducted a 2D and 3D CFD analysis of various airfoil shapes and a straight rigid wing to determine the influence of the opening inlet and trailing edge deflection on the aerodynamic characteristics of ram-air parachutes. The analysis consisted on solving for steady and unsteady state with the RANS equations using Spalart-Allmaras turbulence model.

Figure 2.19 presents the mesh structure of a low speed airfoil (NSRDEC) for the 2D analysis. The 2D analysis consisted on different airfoil shapes including a CLARK-Y M15 and a NASA LS(1)-0417 airfoil. The computational domains were circular with 50 chords length size, structured meshes in the domain, and a boundary layer mesh. The 3D analysis consisted on multiple straight rigid wings with a CLARK-Y M15 airfoil shape, and the results were compared with 2D analysis and experimental data.



a) Airfoil with closed leading edge.



b) Airfoil with opened leading edge.

Figure 2.19 Structure mesh for 2D CFD analysis of an opened and closed NSRDEC airfoil shape. Adapted from (Ghoreyshi, et al., 2016).

The 2D analysis showed that the drag created for the opened leading edge airfoil was significantly larger than the airfoil with closed leading edge. Additionally, the lift produced by the opened airfoil was smaller than the closed airfoil shape. A counterclockwise vortex near the LE inside the open airfoil was attributed to the decrement of the total lift (Ghoreyshi, et al., 2016).

Figure 2.20 shows the lift and drag coefficient versus angle of attack for the 3D analysis of the straight wing. The 3D analysis presented a higher stall angle of attack for the wing as compared with the 2D airfoil (Figure 2.20a). Additionally, the significantly amount of drag created after stall was reflected in greater reduction of L/D values than the 2D airfoil (Figure 2.20b). Finally, the pressure inside the 2D airfoil reached the stagnation pressure, whereas for the wing the internal pressure was below the stagnation pressure value (Ghoreyshi, et al., 2016).

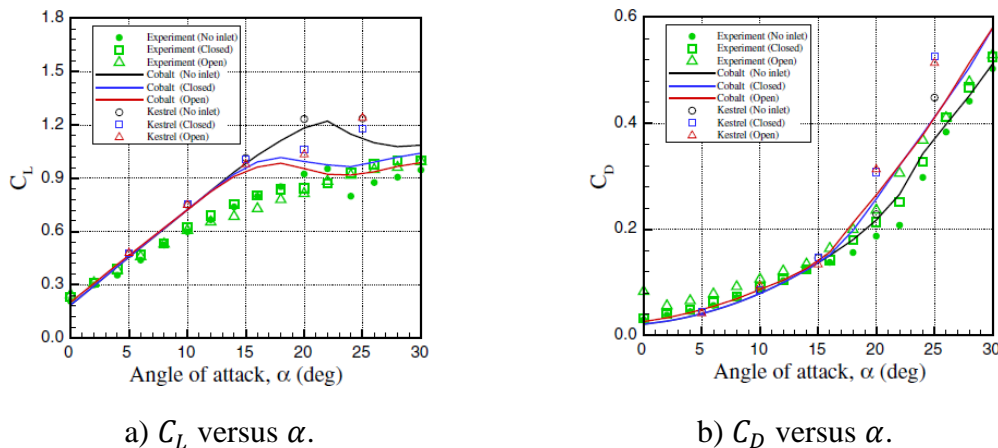


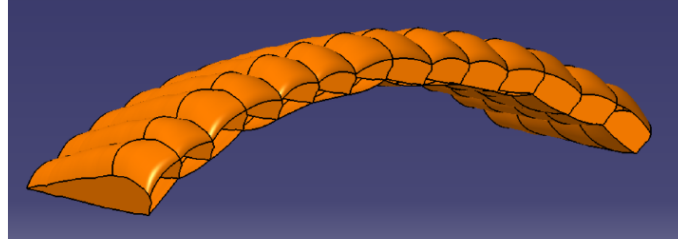
Figure 2.20 Lift and Drag coefficients versus angle of attack curves for different CFD analysis and experiments for a straight wing. Adapted from (Ghoreyshi, et al., 2016).

In 2018, Fonseca performed a CFD research on 2D airfoils and 3D arched rigid wings to determine the influence of different geometry distortions on the aerodynamic performance. Moreover, the longitudinal stability was analyzed with the implementation of suspension lines and a payload. The simulations consisted of solving the steady state RANS equations using the shear-stress transport turbulence model (SST). The domain size had 16 x 10 chords length as suggested from the literature (Fonseca, 2018). In addition, the models were tested for different angles of attack and Reynolds numbers.

Figure 2.21 shows a 2D airfoil and a seven-cell canopy geometry with various distortions. The models presented multiple geometry characteristics such as chord and span lengths, planform shapes, airfoil thickness and aspect ratios, as given in Figure 2.21. Additionally, the geometry distortions were included directly from the CAD software using different semi-empirical criteria and maintained rigid during the CFD simulations.



a) 2D distorted airfoil shape



b) Seven-cell canopy geometry

Figure 2.21 2D and 3D geometries with distortions. Adapted from (Fonseca, 2018).

Results of the simulations showed 45% of L/D reduction for the 2D distorted opened airfoil, where 28% was caused by the opening inlet and the remaining by geometry distortions. Moreover, the incidence angle and translation of the non-loaded ribs increased the lift coefficient as compared with the 3D baseline model. The surfaces inflation and the span shrinkage presented a reduction on the lift coefficient.

The drag polar presented a difference of 23% for all the angles of attack as compared with the experimental data available. This discrepancy was attributed to differences during the experiments from the literature, additional irregularities on the canopy surfaces and numerical model approaches.

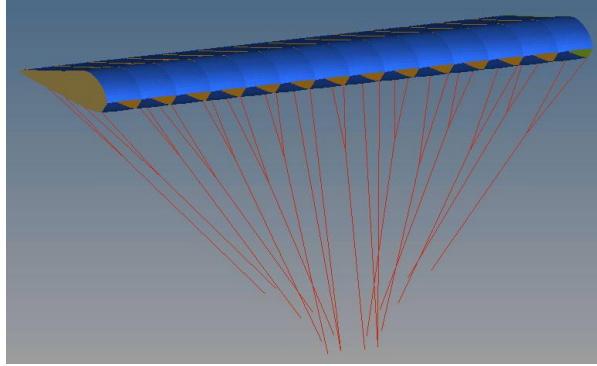
Figure 2.22 shows the internal surface pressure obtained for the numerical simulations of the seven-cell canopy at 0° angle of attack. The internal surface pressure obtained for the seven-cell canopy showed a homogeneous distribution with a maximum value approximately of 0.0214 psi, as shown in Figure 2.22.



Figure 2.22 Internal surface pressure for the seven-cell canopy at 0° angle of attack, top view. Adapted from (Fonseca, 2018).

A robust finite element analysis performed by Peralta and Johari (2015) determined the fully inflight canopy geometry using LS-DYNA as FE software. The simulation consisted on simulating a MC-4 ram-air parachute, including suspension lines, with a rectangular planform shape, a chord and span lengths of 13 ft and 28.5 ft, respectively.

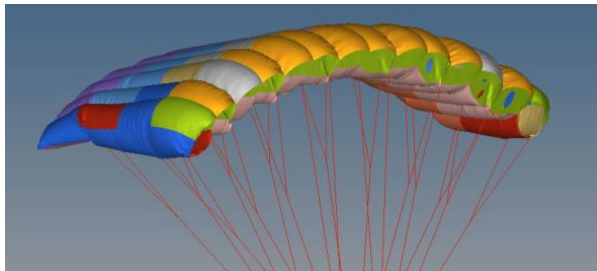
Figure 2.23 presents the undeformed canopy structure and the deformations caused after applying multiple external surface pressure distributions. The FE analysis predicted deformations of the surfaces starting from an undeformed canopy shape, as shown in Figure 2.23a, by using material properties of a low permeability F111 ripstop nylon fabric. In addition, the simulations applied various boundary conditions including internal and external surface pressures from previous numerical analysis. For instance, a constant internal surface pressure of 0.0138 psi (90 Pa corresponding to an airflow velocity of 12.2 m/s) was applied, assuming the internal pressure was approximately equal to the stagnation pressure (Peralta & Johari, 2015). Moreover, constant and variable surface pressures were applied to the external surfaces of the canopy along the chordwise and spanwise directions, as shown in Figure 2.23b and Figure 2.23c.



a) Non-deformed canopy structure.



b) Deformations of the canopy structure caused by external surface pressure, variation along the chordwise direction.



c) Deformations of the canopy structure caused by external surface pressure, variation along the chordwise and spanwise directions.

Figure 2.23 Non-deformed and deformation on the canopy structure by different external surface pressures. Adapted from (Peralta & Johari, 2015).

The authors concluded that for a general design of the canopy structure, the implementation of various external pressure distributions did not significantly affect the end geometry. Contrarily, length of the suspension lines and material properties of the fabric produced major effects on the canopy deformations. Finally, the authors mentioned that a relative accurate geometry structure could be generated for a steady flight regime.

Fogell (2014) developed a simplified FSI approach to determine the equilibrium state of a canopy geometry under the influence of the fluid flow. The investigation consisted on 3D analyzing the fluid flow over a single canopy cell by solving the steady RANS equations, using the $k - \varepsilon$ turbulence model. The simulations were performed at a Reynolds number of 2.1×10^6 with a flow velocity of 108 ft/s (33 m/s).

Figure 2.24 shows a schematic representation of a cross section of the CFD domain along with the boundary conditions applied at each wall. The domain was created with a half cylinder with a diameter of five chords length connected to a parallelepiped of 10 chords length.

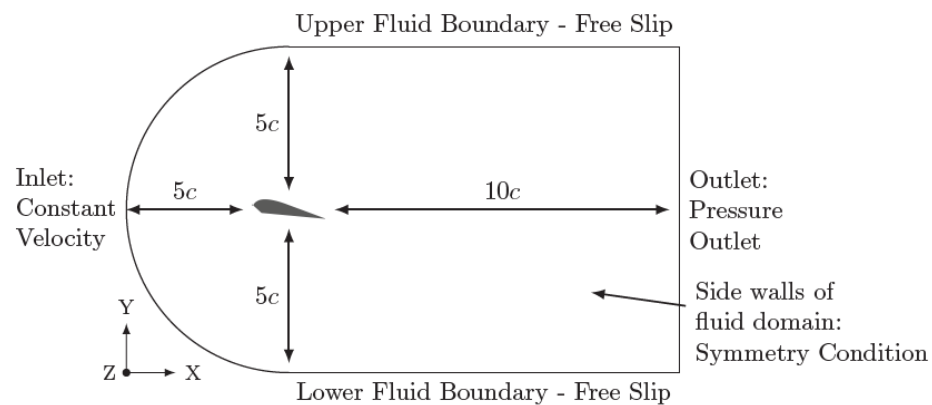


Figure 2.24 Cross section of the 3D CFD domain and boundary conditions applied to the walls. Adapted from (Fogell, 2014).

Additionally, boundary conditions were applied to the wall of the domain such as constant velocity at the side of the cylinder, free slip condition at the top and bottom walls of the parallelepiped, no-slip condition for the canopy surfaces and pressure outlet at the back face of the parallelepiped, as shown in Figure 2.24.

Figure 2.25 shows 3D streamlines around the bottom surfaces of the inflated single cell, creating flow separation at the bottom lip of the opening inlet. The results showed that high internal pressure, i.e., stagnated air, provided rigidity to the canopy structure.

Although the stagnation region at the opening inlet led to cell pressurization, there was a small amount of flow circulating near the bottom lip of the opening inlet, creating areas of high flow separation at the bottom surfaces of the canopy.

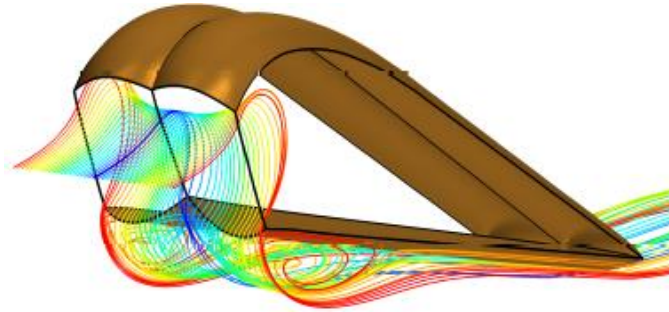


Figure 2.25 3D streamlines around the bottom surface of an inflated single cell canopy geometry. Adapted from (Fogell, 2014).

Although the results showed a difference of lift and drag coefficients of 12% approximately, the author concluded the need for further research to determine a more reliable model to validate CFD and FSI simulations. One possible reason for the difference was prediction of flow separation by using the $k - \varepsilon$ turbulence model.

Burnett (2016) determined a simplified FSI approach to solve for the aerodynamic characteristics and geometry shape of a single cell canopy structure. The CFD analysis consisted on solving the RANS equations along with the SST $k - \omega$ turbulence model to solve for the flow around the single cell. Different ANSYS toolboxes were used for the investigation such as ANSYS Fluent and ICEM. Therefore, an interface, known as mapping zone, enabled the data exchange between the CFD and FEA analysis.

Figure 2.26 shows the computational domain for the CFD analysis of the single canopy cell. A truncated cone domain shape was chosen for the CFD simulations with dimensions of 10 chords length upstream, 15 chords length downstream and a radio of 5 chords length at the location of the cell canopy.

Additionally, experimental tests were conducted for a full-scaled single cell canopy in collaboration with the parachute company, Performance Designs, to validate the numerical results.

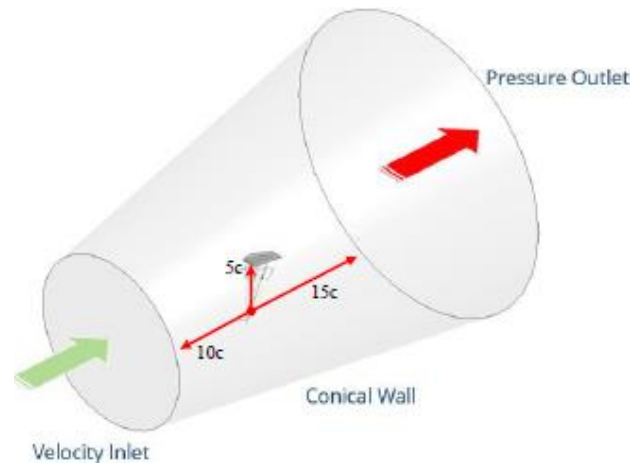


Figure 2.26 Truncated cone CFD domain schematic representation. Adapted from (Burnett, 2016).

Figure 2.27 shows the experimental tests of the single cell canopy in a wooden test section with dimensions of 2.35 ft x 4 ft and 8 ft long. Multiple measurements techniques were applied, including velocity and displacement by using flowmeters and photographs. Additionally, various deformations were simulated at the opening inlet, top and bottom surfaces and non-loaded rib. However, a limitation of the experiment of fixing the fabric ribs to the walls caused inconsistency with the simulation constraints.



Figure 2.27 Experimental test of a single cell canopy. Adapted from (Burnett, 2016).

The investigation concluded that the geometry shape from the FSI analysis followed similar trends as compared to the experimental tests. However, Burnett mentioned a difference of 25% of the numerical analysis because of the limitations during the experiments and the different boundary conditions applied to the analysis.

Ortega et al. (2017) implemented a low-cost and low-fidelity numerical approach to determine the steady descent characteristics of the parachute using panel method with low-order doublets and sources. A computer program called PARACHUTES was used for the analysis of two different scenarios of descending: free-flight with no deflection and symmetrical deflection of the steering lines while descending, which were compared with experimental data available.

The numerical analysis showed a difference on the lift and drag coefficients as compared with experimental values, mainly because the software used potential flow solver, neglecting friction forces. Additionally, the authors emphasized on the possible implementation of semi-empirical models accounting for flow separation to improve the accuracy of the results at low cost (Ortega, Flores, & Pons-Prats, 2017).

Overall, computational studies have provided a better understanding of the aerodynamic performance and geometry behavior of ram-air parachutes under simulated flight conditions, leading to new design techniques. For instance, airflow visualization, deformation and displacement approximations could accurately predict the inflight behavior of a flexible parachute. Consequently, multiple investigations including 2D, pseudo 2D and 3D analysis have been performed for a wide range of flight conditions. However, most of the investigation aim to predict the free flight behavior of the parachute, i.e., in an opened environment, as compared to an enclosure domain such as the test section of a wind tunnel. Therefore, the implementation of preliminary test predictions to determine the aerodynamic performance of ram-air parachutes in wind tunnel test sections have not been subject of study to the author's knowledge.

3. CAD Methodology and CFD Approach

3.1. Parafoil Geometry Development

Ram-air parachutes resemble low aspect ratio, arched wings when inflated because of the airflow interaction with the canopy structure. The flexible canopy shape is highly dependent on surface pressures and tension forces in the lines, increasing the complexity of the geometry. Therefore, modeling techniques concentrate their efforts on approximating the deformations of the canopy geometry by using scan heads, photographs and mathematical models.

The ability to generate the canopy geometry implementing design parameters and deformations of the structure provides a more accurate prediction of the aerodynamic performance of the parachute. Additionally, the need of a canopy generation to create repeatedly different models allows a wide range of analysis in a short amount of time.

Consequently, a semi-automatic geometry process is presented in this section, which is capable of generation the parachute surfaces using multiple design parameters and modeling deformations.

3.1.1. Introduction to CATIA V5

CATIA V5 is a software for 3D computer-designed used in multiple engineering fields such as automobile, mechanical, electric and especially aerospace (Daneshjo, Korba, & Eldojali, 2012). The available tools within the various CATIA workbenches facilitate the geometry modeling depending its complexity. For instance, part design workbench allows to model solid geometries, while the generative shape design workbench permits the modeling of surfaces and panels such as the fuselage and wing structure of an airplane. Additionally, this CAD software enables a parametric modeling option

improving the efficiency and time of the design (Daneshjo, Korba, & Eldojali, 2012). Consequently, the present investigation employed CATIA V5 as the CAD design software to model the canopy geometry using primarily the generative shape design workbench.

3.1.2. Programming Interface Approach

The CAD methodology started from a 2D airfoil shape and design characteristics such as chord length and thickness, which information was implicit in a cloud of points or raw data. The post processing of these data along with the implementation of other design parameters such as span length, number of ribs and opening inlet height, determined the general structure of the 3D canopy. Therefore, the CAD methodology employed different software, e.g., Excel and MATLAB, for data collection and organization before the geometry design in CATIA. Figure 3.1 gives a schematic of the different software used and the process for the canopy CAD generation.

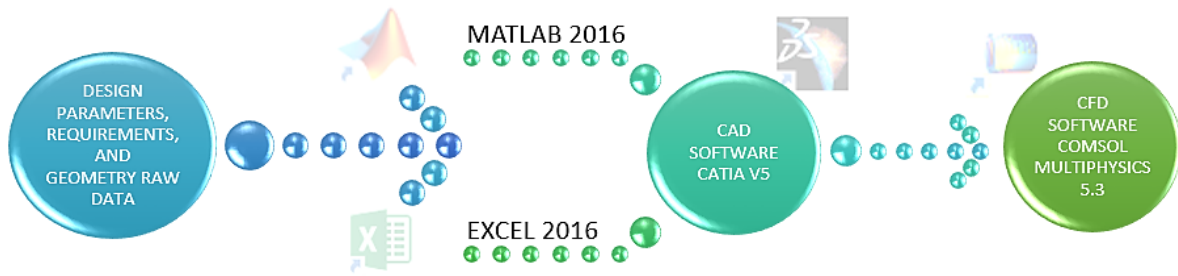


Figure 3.1 Schematic for the CAD generation process.

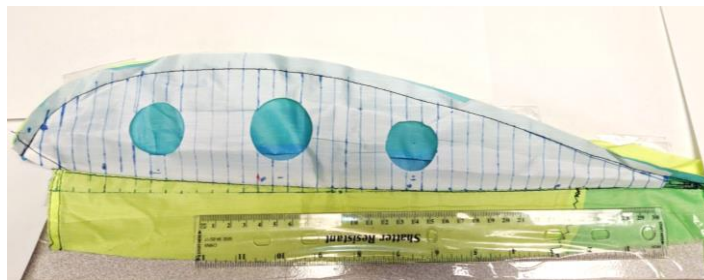
The raw data of the 2D airfoil design was analyzed with two different methods, depending the number of ribs provided, as illustrated in Figure 3.1. On one hand, if the provided raw data contained one single airfoil shape, a MATLAB script was developed to process the cloud of points and generate the remaining canopy ribs, including design

parameters such as planform shape, number of ribs and anhedral angle. Later, the script imported the cloud of points into CATIA to generate the canopy surfaces. If the raw data contained the multiple canopy ribs, an Excel macros was developed to import directly into CATIA and generate the canopy surfaces.

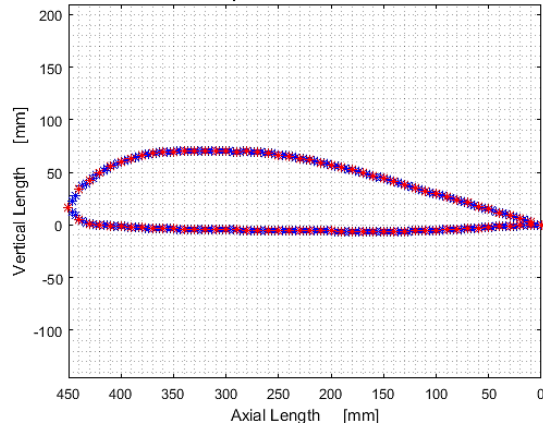
A macros script coded in Visual Basic generated the basic canopy structure in CATIA, implementing an incidence angle to the non-loaded ribs and inflation of the surfaces by using points and splines. The surfaces were created manually to prevent possible deformations and warnings messages on the CAD software. Finally, the canopy geometry was imported into the CFD software for numerical simulations.

3.1.3. CAD Design Methodology

The CAD generation methodology started with the digitalization of a well-known 2D airfoil by extracting the point coordinates of the upper and lower edges. During the post process in MATLAB, design parameters such as chord length, airfoil thickness and number of points were implemented. For instance, a scaling factor that modified the point coordinates determined the required chord length and airfoil thickness. Figure 3.2 presents a fabric airfoil rib of a scaled kite model and the digitalized cloud of points.



a) Fabric kite airfoil.



b) Digitalized cloud of points.

Figure 3.2 2D airfoil shape of a scaled kite model.

The multiple canopy ribs were created by reproducing the point coordinates at different span locations. At this stage, design parameters such as anhedral angle, number of ribs, span length and planform shape were implemented to design the general structure of the canopy. Figure 3.3 shows the canopy ribs for the scaled kite model.

Although the MATLAB script was capable of reproducing the full number of ribs, the ribs of a half canopy were necessary for the geometry creation in CATIA. Additionally, noticed in Figure 3.3 that the end cell consisted on a single sewing connection between the upper and lower surfaces.

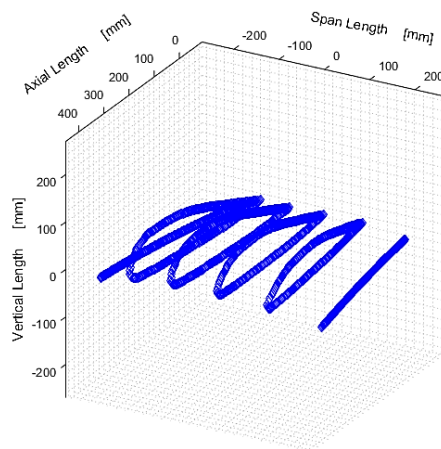


Figure 3.3 Full number of canopy ribs generated with a MATLAB script.

The point coordinated of the ribs for a half side of the canopy were imported into CATIA using an Excel macros. Figure 3.4 shows the imported point coordinates in CATIA of the ribs for a half kite canopy model.

In the case to be provided of a cloud of points with the multiple canopy ribs, the point coordinates had to reflect implicitly all design parameters previously mentioned. Therefore, the post-process in MATLAB was omitted and the points were imported directly into CATIA.

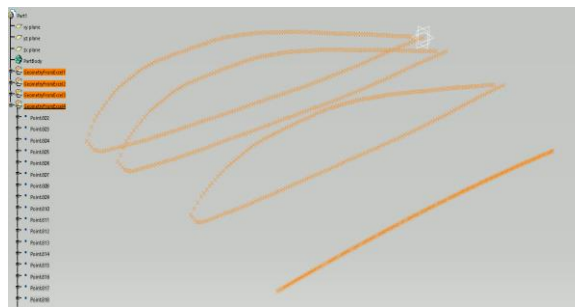


Figure 3.4 Rib coordinate points imported into CATIA for a half kite canopy model.

The general structure of the canopy, consisted of splines and additional points, was created using the macros in CATIA. These geometry features enabled the user to modify the surfaces of the canopy. For instance, an increment of a spline curvature would lead to a more pronounced surface curvature. Figure 3.5 shows the multiple points and splines generated by the macros for the kite model.

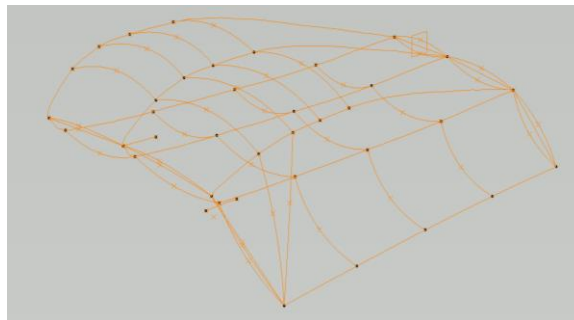


Figure 3.5 General structure of the scaled canopy kite.

Additionally, multiple parameters were implemented within the code such as the translation and incidence angle of the non-loaded ribs, opening inlet height and curvature of the upper and lower surfaces of the canopy. Figure 3.6 shows a 2D airfoil shape with the location of the opening inlet.

The opening inlet design was defined by the angles α_1 and α_2 according to the chord line and the point A, which was located one tenth of the chord length from the LE, shown in Figure 3.6. The macros performed an iterative process to determine the location of the points for the opening inlet corresponding to the required angles of α_1 and α_2 .

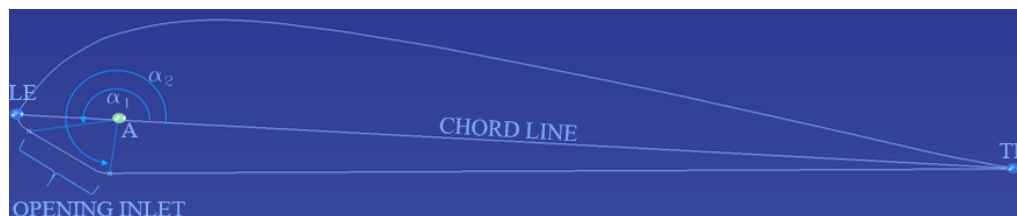


Figure 3.6 Location of the opening inlet in a 2D airfoil shape.

The *Multi-Section Surfaces* and *Fill* tools available in the generative shape design workbench in CATIA created the canopy surfaces (Dassault Systèmes, 2006). In addition, the *Mirror* tool enabled to project the other half of the canopy model. Notice that the surfaces created had no thickness to represent the non-porous thin fabric and facilitate the mesh creation for the numerical simulations. Figure 3.7 shows the canopy with the surfaces for the kite model simulating the structure inflation by curving the upper and lower surfaces of the canopy. Moreover, different design features such as the crossports in the airfoil ribs, as illustrated in Figure 3.7, and the round shape at the TE are represented at this stage.

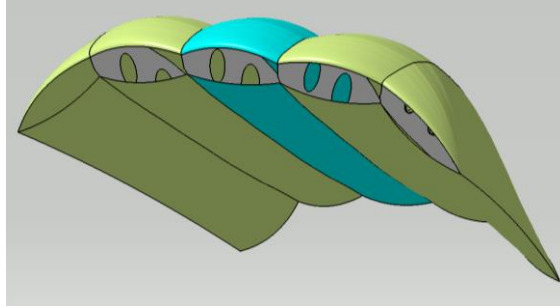


Figure 3.7 Canopy surfaces for the kite model simulating a structure inflation.

3.1.4. Benchmark Geometry Models

This investigation focused on the geometry of two canopy models, which were created using the methodology explained in the previous section. The first canopy model was a small flexible kite, as illustrated in Figure 3.7. The second canopy model was a scaled flexible parachute from Ware & Hassell (1969) and Nicolaides (1971), which was tested in the NASA Langley wind tunnel.

Scaled Kite Model

The scaled kite model was a canopy made of non-porous fabric with a trapezoid planform shape approximately. Additionally, the kite had five chambers and the end cells had a single sewing attachment between the upper and lower surfaces. The kite model was purchased considering the size dimensions of the wind tunnel test section at Embry-Riddle.

Figure 3.8 shows the top view of the kite model that was acquired. Notice the trapezoid planform shape with a curvature shape at the LE and TE of the canopy.



Figure 3.8 Top view of the flexible scaled kite model.

The CAD geometry of the scaled kite was created as explained in the previous section.

The various geometry parameters and dimensions are presented in Table 3.1 .

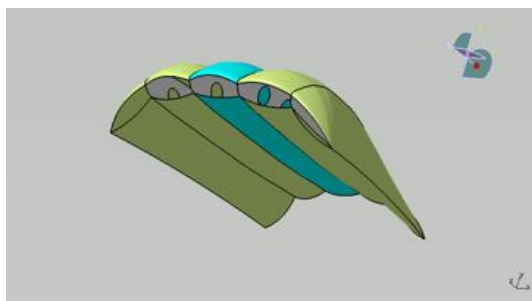
Table 3.1

Geometry characteristics of the scaled kite model.

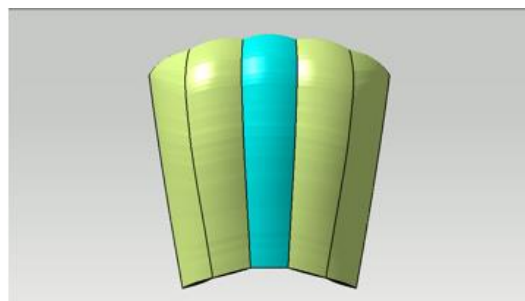
DESCRIPTION	PARAMETER	VALUE
CHORD LENGTH	c	1.48 ft
MEAN SPAN LENGTH	b	1.44 ft
PLANFORM AREA	S	2.12 ft ²
ASPECT RATIO	AR	0.97

The isometric and top views of the CAD model of the kite are shown in Figure 3.9.

Notice that the upper and lower surfaces are simulating inflation. However, for the numerical analysis, the surfaces of the canopy were modeled as completely flat, i.e., no inflation to neglect any effect of the deformation in the analysis.



a) Isometric view



b) Top view

Figure 3.9 CAD model representation of the kite.

Ware & Hassell Parachute Model

The scaled canopy tested by Ware and Hassell in 1969, referred as the canopy from W&H, was made of a non-porous acrylic-coated nylon fabric with a rectangular planform shape. The canopy has 16 chambers and the end cells had a rib attaching the upper and lower surfaces. The canopy model was attached to various suspension lines at the bottom edge of the loaded ribs during the tests to maintain a homogenous shape and rigidity of the fabric (Ware & Hassell, 1969).

Geometric characteristics and coordinate points of the airfoil shape were provided from the published investigation. Therefore, the CAD model of the parachute was created following the methodology presented in the previous section.

The various geometry characteristics and dimensions are presented in Table 3.2.

Coordinates of the airfoil shape for this canopy are provided in Table A.1 in Appendix A.

Table 3.2

Geometry characteristics of the canopy model from Ware & Hassell.

DESCRIPTION	PARAMETER	VALUE
CHORD LENGTH	c	8.57 ft
SPAN LENGTH	b	17.15 ft
PLANFORM AREA	S	147 ft ²
ASPECT RATIO	AR	2

The isometric and top views of the CAD model of the canopy from Ware & Hassell are presented in Figure 3.10. Notice that the upper and lower surfaces of the canopy were maintained flat during the CAD generation. The main purpose of the geometry with flat surfaces was to isolate the effects caused by the different deformations presented in the fabric, which were out of scope for the present investigation.

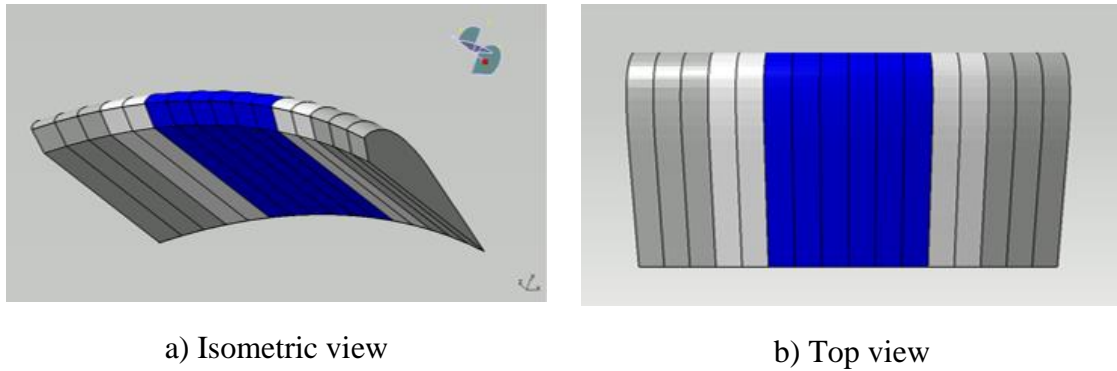


Figure 3.10 CAD model representation of the canopy from Ware & Hassell.

The numerical analysis to determine the performance of the canopies were conducted using the kite model and the canopy of Ware & Hassell. Analysis set-up and results are presented in Chapters 5 and 6, respectively.

3.2. Computational Modeling Approach

The technology growth during the past years has facilitated the implementation of numerical approaches to determine the aerodynamic performance of ram-air parachutes. For example, strong advantages of CFD analysis are the multiple results obtained for flow visualization, vorticity, pressure and velocity fields along with calculation of flow characteristics around a rigid body under simulated conditions. Therefore, CFD simulations are able to provide a wide range of outcomes and determine the flow behavior with no geometry limitations essentially (Ghoreyshi, et al., 2016).

However, majority of the numerical investigations aim to predict the free flight behavior of the parachute, i.e., in an opened environment, as compared to an enclosure domain such as the test section of a wind tunnel. Consequently, preliminary test predictions to determine the aerodynamic performance of ram-air parachutes in a wind tunnel test section are presented in this chapter.

The canopy tested by Ware & Hassell, presented in the previous chapter, was investigated for multiple cases under similar flow conditions to determine the feasibility of experimental tests in the low speed subsonic wind tunnel test section at Embry-Riddle.

3.2.1. COMSOL 5.3 Multiphysics Introduction

Numerous computer software offer CFD modules to perform simulations such as ANSYS Fluent, STAR CCM+ and COMSOL Multiphysics. The CFD software used in this investigation was COMSOL 5.3 Multiphysics because of low cost industry software (Fonseca, 2018). In addition, the ability of this software to implement different physic analysis, e.g., thermal and fluid flow analysis, predicts accurately real world aspects and facilitate further numerical studies including FSI.

Furthermore, the present investigation required two modules to perform the analysis using COMSOL: CAD Import and the Fluid Flow CFD modules. The canopy geometry created in CATIA was imported into COMSOL as .stp or .igs file type using the CAD Import module. Later, the CFD module enable the fluid flow analysis for different regimes such as laminar or turbulent flow (COMSOL, 2017).

The simulation setup, run parameters and mesh independence study are described in the following sections. Additionally, the optimum time for cluster computations and different cases of the test matrix are also presented in this chapter.

3.2.2. Governing Equations, Turbulence Modeling and Wall Treatment

The fluid flow behavior is described by the momentum equations, also known as Navier-Stokes equations, given by Equations (3.1), (3.2) and (3.3) for unsteady state, incompressible, three dimensional, Newtonian flow with no external forces (Anderson, 2010). Additionally, the continuity equation describing the mass conservation is

presented in Equation (3.4).

$$\rho \left(u \frac{\partial u}{\partial x} + v \frac{\partial u}{\partial y} + w \frac{\partial u}{\partial z} \right) = -\frac{\partial p}{\partial x} + \mu \left(\frac{\partial^2 u}{\partial x^2} + \frac{\partial^2 u}{\partial y^2} + \frac{\partial^2 u}{\partial z^2} \right) \quad (3.1)$$

$$\rho \left(u \frac{\partial v}{\partial x} + v \frac{\partial v}{\partial y} + w \frac{\partial v}{\partial z} \right) = -\frac{\partial p}{\partial y} + \mu \left(\frac{\partial^2 v}{\partial x^2} + \frac{\partial^2 v}{\partial y^2} + \frac{\partial^2 v}{\partial z^2} \right) \quad (3.2)$$

$$\rho \left(u \frac{\partial w}{\partial x} + v \frac{\partial w}{\partial y} + w \frac{\partial w}{\partial z} \right) = -\frac{\partial p}{\partial z} + \mu \left(\frac{\partial^2 w}{\partial x^2} + \frac{\partial^2 w}{\partial y^2} + \frac{\partial^2 w}{\partial z^2} \right) \quad (3.3)$$

$$\frac{\partial u}{\partial x} + \frac{\partial v}{\partial y} + \frac{\partial w}{\partial z} = 0 \quad (3.4)$$

Where ρ is the air density, μ is the air dynamic viscosity, P is the static pressure and u , v and w are the velocity components in the x, y and z directions, respectively.

The unsteadiness and the effects of the turbulence on the fluid flow increase the complexity while solving the Navier-Stokes equations. Therefore, multiple approaches were developed to solve the aforementioned equations depending on the computational resources and time available. For instance, Direct Numerical Simulation (DNS) provides solution for the equations with high fidelity by solving the full range of the turbulent eddy scales. Large Eddy Simulation (LES) provides a great approximation of the solution for the equations by solving medium to large turbulence eddy scales (Fogell, 2014).

Although DNS and LES solve accurately the Navier-Stokes equations, the CPU time and resources required for the computation are the primarily limitations. Therefore, a more feasible solution is provided by the Reynolds-Averaged Navier-Stokes (RANS) approach, which approximates the full range of turbulence eddy scales by implementing a statistical model (Fogell, 2014). Consequently, the present investigation solves the RANS equations to determine the fluid flow behavior in an enclosed domain.

The present investigation employed the Shear Stress Transport (SST) turbulence model to solve for the fluid flow at the boundary layer and the free stream. This

turbulence model is a combination of the $k - \epsilon$ model in the free stream and boundary layer wake region, and the $k - \omega$ model near the walls in the buffer and log layers (Fonseca, 2018).

Additionally, a strong advantage of the SST turbulence model is its effectiveness to solve for flow separation because of adverse pressure gradient (Burnett, 2016). Therefore, researches performed by Burnett and Fonseca used the SST model to approximate the turbulence behavior of the flow.

Finally, the turbulence effects on the boundary layer near the wall, also known as viscous sublayer region, were considered into account by implementing a low Reynolds number wall treatment.

3.2.3. General Model Setup

The 3D canopy was placed in an enclosed domain of a rectangular cuboid shape with the following dimensions: 10 chords length upstream from the canopy TE, 20 chords length from the canopy TE and 10 chords length to each side from the center canopy rib. Similar domain shape and size were used for the numerical analysis conducted by Fonseca for the 3D canopy simulations. Figure 3.11 presents the CFD fluid flow domain along with its dimensions.

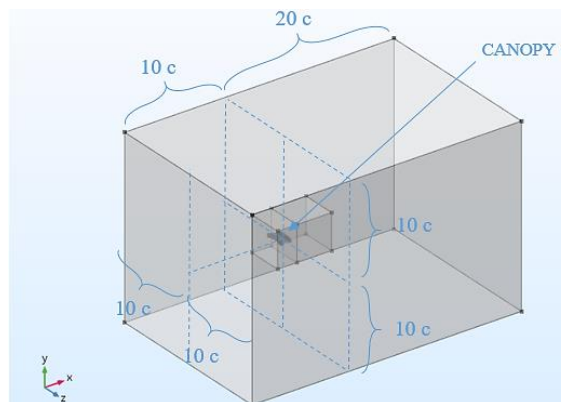


Figure 3.11 Rectangular cuboid, CFD fluid flow domain.

Moreover, a scaled rectangular cuboid was created containing the canopy, as illustrated in Figure 3.11, to provide more flexibility during the mesh generation process.

3.2.4. Boundary Conditions

Figure 3.12 presents the boundary conditions applied, which are described as follow:

- Upstream boundary domain wall. Inlet velocity field $f(x, y, z)$ as function of the angle of attack α .

$$x = V\cos(\alpha)$$

$$y = V\sin(\alpha)$$

$$z = 0$$

Where V is the free-stream velocity.

- Downstream boundary domain wall. Open boundary with normal stress $f_0 = 0$.
- Top and Bottom boundaries domain walls. Wall free-slip boundary condition with $\vec{V} \cdot \vec{n} = 0$. Where \vec{V} is the velocity vector and \vec{n} is the normal unit vector to the domain walls.
- Side boundaries domain walls. Open boundary with normal stress $f_0 = 0$.
- Canopy surfaces. Interior wall no-slip condition with $\vec{V} = 0$. Impermeable, rigid walls and no thickness.

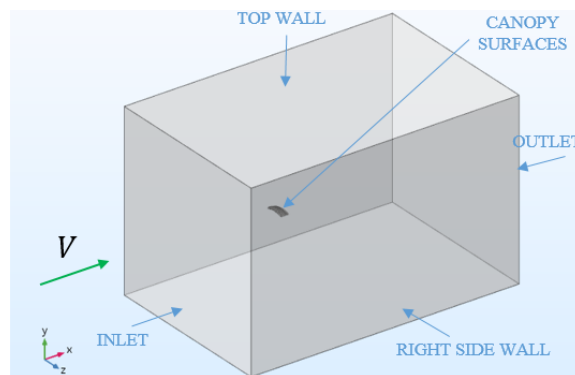
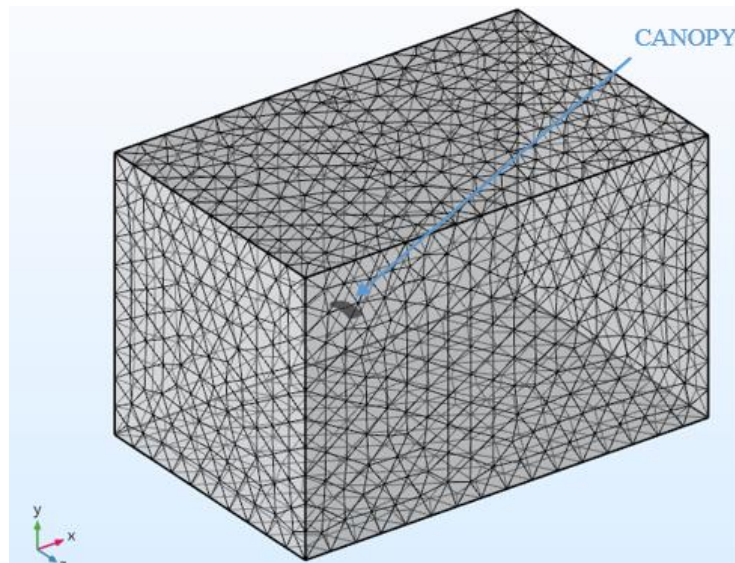


Figure 3.12 CFD analysis boundary conditions.

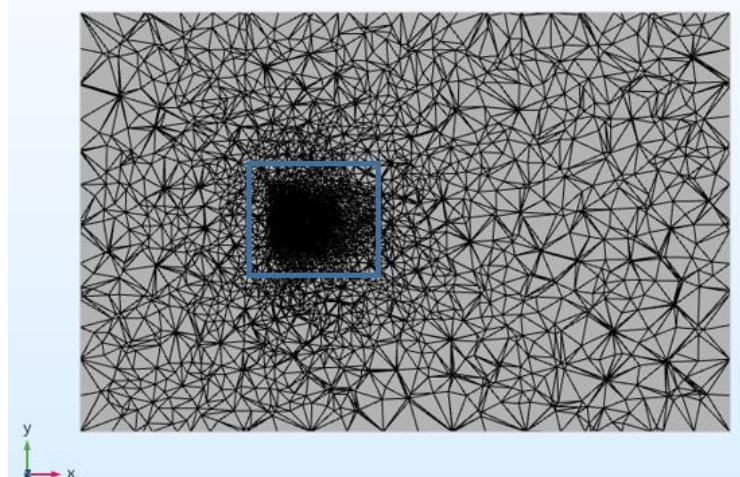
3.2.5. Mesh Independence Study

The Ware & Hassell canopy model was employed to perform the mesh analysis. The mesh grid for all simulation cases consisted on an unstructured tetrahedral mesh elements within all the domains and triangular mesh elements on the canopy surfaces. For locations near the canopy surfaces, the element size was small and increased gradually as the elements were located far in the stream flow. A mesh independence study was conducted to determine the optimum number of elements and size for the CFD simulations. The succeeding mesh was employed for the numerical analysis in this investigation.

Figure 3.13a shows the isometric view of the mesh created for the entire domain. Additionally, a cross section of the domain along the mid canopy, as presented in Figure 3.13b, rib illustrates the mesh in a 2D view. Notice the concentration of the mesh elements located near the canopy, as shown with the blue rectangle in Figure 3.13b.



a) Isometric view of domain with mesh



b) Cross section of the domain mesh.

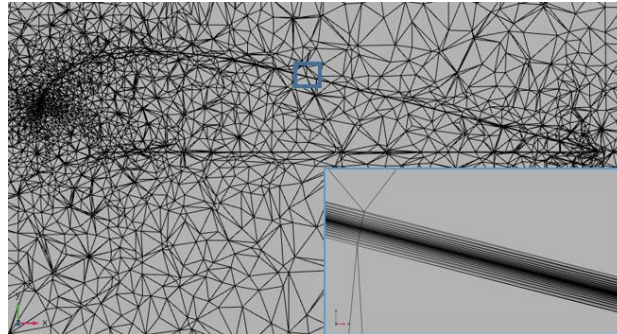
Figure 3.13 Domain mesh.

The boundary layer effects were captured by creating prism layers, i.e., structured boundary layer mesh, adjacent to the canopy surfaces. A total number of 12 layers were necessary to solve for the boundary layer thickness, which was approximated based on turbulent flow on a flat-plate theory (Fonseca, 2018).

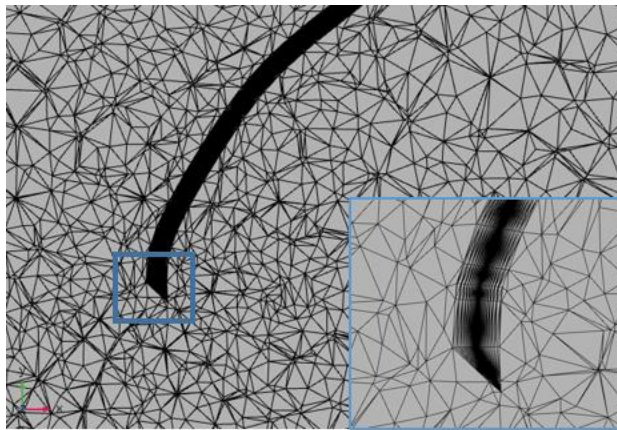
The need of the appropriate height for the prism layers to solve accurately for the boundary layer effects ensures the non-dimensional distance to cell center to be close to 1. This parameter is similar to the y^+ value in other CFD software. Therefore, the closer the value of this parameter to 1, the more accurately the boundary layer is solved (COMSOL, 2017). Consequently, the height of the first layer was estimated to be 7×10^{-5} ft, the consecutive layers increased in height with a stretching factor of 1.2.

Figure 3.14a presents a view of the cross section of a chamber, where the boundary layer mesh is visualized around all the edges, as shown with the blue rectangle. Additionally, Figure 3.14b presents a view of the top lip of the opening inlet, where the prism layers grow from the canopy surface, as shown with the blue rectangle. Multiple

challenges were faced creating the mesh at the sharp corners such as the TE and at the lips of the opening inlet.



a) Chamber cross section view.



b) Top lip of the opening inlet.

Figure 3.14 Boundary layer mesh along the edges of a chamber cross section view.

The presented mesh, denominated as baseline mesh in this investigation, had a total number of elements of 5.1 million approximately, including tetrahedral, triangular and prism elements. The size of the baseline mesh was increased twice using scale factors of 1.4 (medium mesh) and 1.2 (coarse mesh) to reduce the computational time. Consequently, the medium and the coarse mesh had a total number of elements approximately of 2.6 million and 1.8 million, respectively.

Various criteria determine the quality of the elements in the mesh such as the

skewness and growth rate. For this investigation, the element quality was calculated using the skewness measurement, which is commonly employed to evaluate the mesh. The closer of the quality value is to 1, the more accurate the mesh solves the physics (COMSOL, 2017).

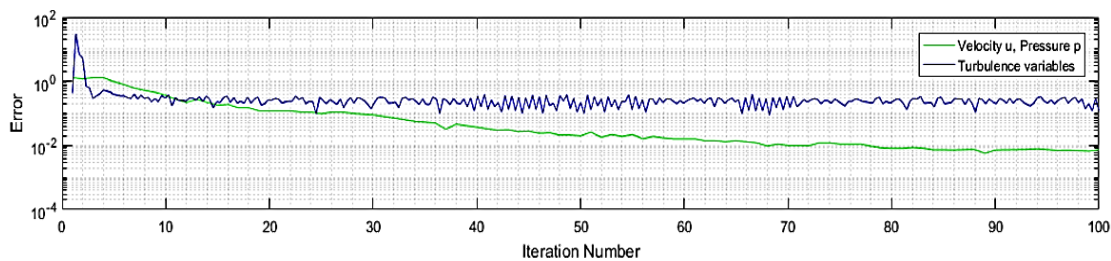
The independence mesh study was conducted comparing the baseline, the medium and coarse meshes. The optimum mesh was determined using the following criteria: highest element quality, lowest number of elements, distance to cell center and residual errors during the simulations.

The study was conducted with the same run parameters for the three cases. Table 3.3 presents the run parameters for the simulations to determine the optimum mesh.

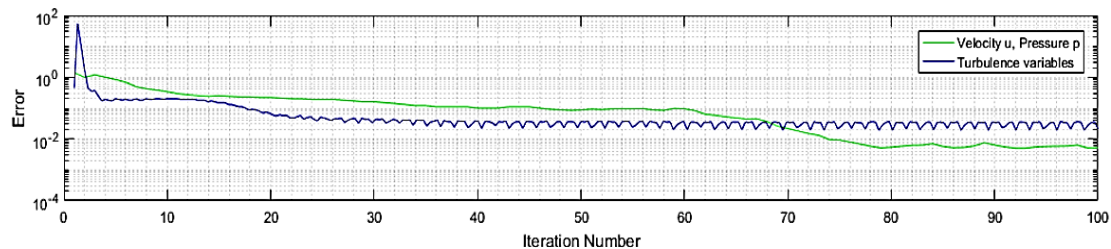
Table 3.3
Run parameters for mesh independence study.

DESCRIPTION	PARAMETER	VALUE
FLOW VELOCITY	V	50 ft/s
AIR DENSITY	ρ	0.002378 slug/ft ³
REYNOLDS NUMBER	Re	2.727×10^6
AIR DYNAMIC VISCOSITY	μ	3.737×10^{-7} slug/(s ft)
ANGLE OF ATTACK	α	4°
MESH SIZE	----	VARIABLE
NUMBER OF ITERATIONS	----	100

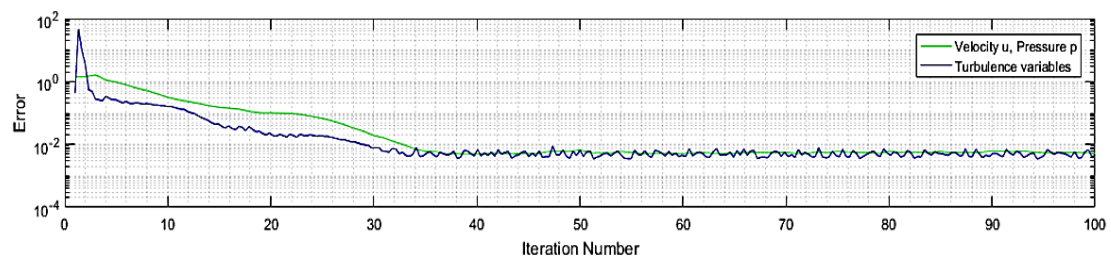
Figure 3.15 shows the residual errors of the velocity, pressure along with the turbulence variables for the three cases. Notice that for all the cases, convergence was achieved after 80 iterations. However, the numerical results presented an offset because the aforementioned variables did not decrease below 10^{-3} as expected. A detailed discussion is presented in Chapter 6 about the possible sources of different in the results. Although convergence of the results are achieved for the three different cases, the coarse mesh presented the lowest residual errors, as presented in Figure 3.15c.



a) Baseline mesh



b) Medium mesh



c) Coarse mesh

Figure 3.15 Convergence plots for the independence mesh study.

Figure 3.16 presents the non-dimensional distance to cell center, i.e., similar to the y^+ value, over the canopy surfaces for the coarse mesh. The canopy surfaces had an overall distance to cell center less than two. Notice the highest values were presented at the sharp corners such as the TE and LE at the end cells and top surfaces adjacent to the LE, as presented with the blue rectangles in Figure 3.16.

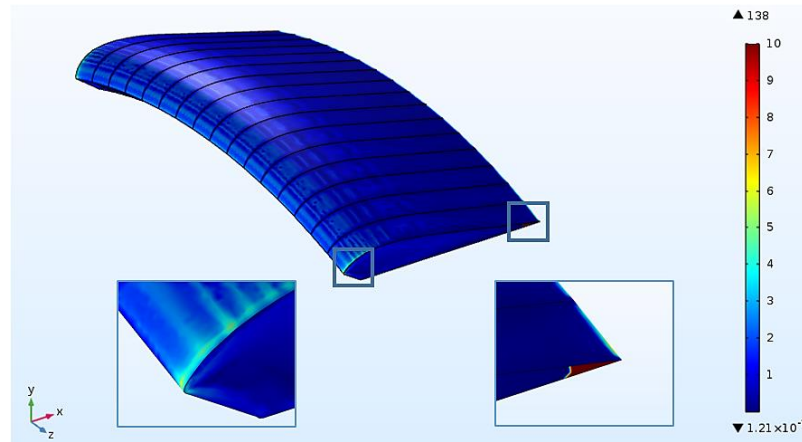


Figure 3.16 Non-dimensional distance to cell center for the coarse mesh.

Finally, the coarse mesh presented an overall element quality of 0.617, while for the prism layers the local element quality was 0.802 approximately. The study concluded that the coarse mesh presented better results compared with the other mesh sizes. Consequently, further simulations for the multiple cases employed meshes with similar characteristics as the coarse mesh presented.

3.2.6. Computational Time

The multiple simulations were conducted using the high performance supercomputer Vega from Cray Inc. Vega is composed of four-cabinet Cray CS400 with 3024 cores, i.e., processors, distributed in 84 nodes. The cluster is capable to solve complex computational problems such as weather and atmospheric dynamics, subsonic and supersonic aerodynamics among other numerical simulations (Pinholster, 2017).

The required time for the supercomputer to solve the numerical simulations was determined using the coarse and medium meshes presented in the previous section solved using different amount of processors.

The study was conducted with the same run parameters for the two cases. Table 3.4 presents the run parameters for the simulations to determine the optimum computational

time in the cluster.

Table 3.4

Run parameters for computational time study in the cluster Vega.

DESCRIPTION	PARAMETER	VALUE
FLOW VELOCITY	V	50 ft/s
AIR DENSITY	ρ	0.002378 slug/ft ³
REYNOLDS NUMBER	Re	2.727×10^6
AIR DYNAMIC VISCOSITY	μ	3.737×10^{-7} slug/(s ft)
ANGLE OF ATTACK	α	4°
MESH SIZE	----	VARIABLE
NUMBER OF PROCESSORS	----	VARIABLE
NUMBER OF ITERATIONS	----	50

Figure 3.17 shows the computational time required to solve the numerical problem for the two meshes at different combinations of nodes in the cluster.

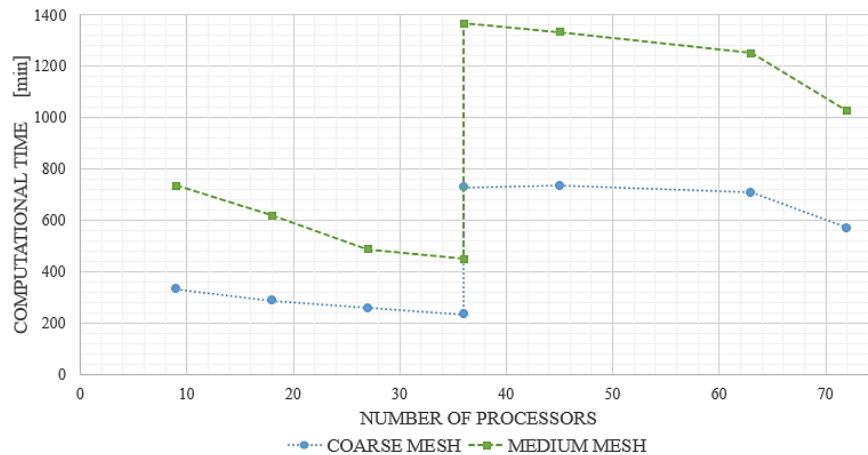


Figure 3.17 Computational time required in the cluster Vega for two different meshes.

Results of the study showed that the lowest computational time was achieved using one full node with 36 processors. This configuration reduces the amount of time between processors and avoids communication bottlenecks between multiple nodes. Additionally, the time increased drastically when using multiple nodes for the same amount of elements in the mesh. Finally, although the increase of mesh elements would demand multiple nodes, the best performance was achieved when the simulation was running

approximately from 50,000 to 75,000 elements per processor in one single node.

Consequently, further simulations for the multiple cases employed one single node with 36 processors.

3.2.7. Test Cases and Flow Parameters

The numerical analysis consisted on five different scenarios using the canopy of Ware & Hassell to validate the feasibility of experimental tests in a low speed subsonic wind tunnel. The first case consisted on the analysis of the canopy tested by Ware & Hassell with the same geometry characteristics and flow conditions from literature to validate the numerical with the experimental results from the literature.

The geometry characteristics for the canopy were previous presented in Table 3.2. Additionally, the domain size selected had the same dimensions as presented in Figure 3.11 to simulate the fluid flow behavior with no wall effects. Finally, the flow conditions for this case, corresponding to standard sea level conditions, are presented in Table 3.5.

Table 3.5
Fluid flow conditions and run parameters for the analysis of Case 1.

DESCRIPTION	PARAMETER	VALUE
FLOW VELOCITY	V	50 ft/s
AIR DENSITY	ρ	0.002378 slug/ft ³
REYNOLDS NUMBER	Re	2.727×10^6
AIR DYNAMIC VISCOSITY	μ	3.737×10^{-7} slug/(s ft)
ANGLE OF ATTACK	α	$0^\circ \leq \alpha \leq 12^\circ$
TOTAL PRESSURE	P_O	1 atm
AMBIENT TEMPERATURE	T	293.15 K
MACH NUMBER	M	0.044

Notice the total pressure (P_O) was the sum of the atmospheric pressure (P_{atm}) and the gauge pressure (P_{gauge}).

The second case consisted on the analysis of the canopy by Ware & Hassell with the

same geometry characteristics. However, the canopy was simulated at a lower fluid flow velocity, thus the Reynolds number decreased.

The main objective of this case was to determine the effects on the canopy performance caused by low Reynolds number. Therefore, the velocity was selected considering an average airflow velocity that the kit would experience in an opened environment, 10 ft/s. In addition, this case determined the feasibility of experimental tests in the low speed wind tunnel from Lehman Building at Embry-Riddle.

As a recall from Chapter 4, the geometry characteristics for the canopy were presented in Table 3.2. Additionally, the domain size selected had the same dimensions as presented in Figure 3.11 to simulate the fluid flow behavior with no wall effects. Finally, the flow conditions for this case, corresponding to standard sea level conditions, are presented in Table 3.6.

Table 3.6
Fluid flow conditions and run parameters for the analysis of Case 2.

DESCRIPTION	PARAMETER	VALUE
FLOW VELOCITY	V	10 ft/s
AIR DENSITY	ρ	0.002378 slug/ft ³
REYNOLDS NUMBER	Re	5.46×10^5
AIR DYNAMIC VISCOSITY	μ	3.737×10^{-7} slug/(s ft)
ANGLE OF ATTACK	α	$0^\circ \leq \alpha \leq 12^\circ$
TOTAL PRESSURE	P_o	1 atm
AMBIENT TEMPERATURE	T	293.15 K
MACH NUMBER	M	0.009

The third case consisted on the analysis of the canopy by Ware & Hassell with the same chord length as the kite model. Therefore, the chord length of the canopy was reduced by a factor of 5.82, approximately. The Reynolds number was maintained as the first case by increasing the airflow velocity to 290 ft/s.

The main objective of this case was to determine the effects caused by scaling the

canopy model. Additionally, notice that the increment of the velocity from 50 ft/s to 290 ft/s was reflected in an increment of the Mach number from 0.04 to 0.26, approximately.

This effect was subject for the analysis of the next case.

The domain size selected had the same dimensions as presented in Figure 3.11 to simulate the fluid flow behavior with no wall effects. Finally, the canopy geometry dimensions along with the flow conditions for this case, corresponding to standard sea level conditions, are presented in Table 3.7.

Table 3.7

Canopy geometry dimensions, fluid flow conditions and run parameters for the analysis of Case 3.

CANOPY GEOMETRY		
DESCRIPTION	PARAMETER	VALUE
CHORD LENGTH	c	1.48 ft
SPAN LENGTH	b	2.95 ft
PLANFORM AREA	S	4.37 ft ²
ASPECT RATIO	AR	2
FLOW CONDITIONS		
DESCRIPTION	PARAMETER	VALUE
FLOW VELOCITY	V	290 ft/s
AIR DENSITY	ρ	0.002378 slug/ft ³
REYNOLDS NUMBER	Re	2.727×10^6
AIR DYNAMIC VISCOSITY	μ	3.737×10^{-7} slug/(s ft)
ANGLE OF ATTACK	α	$0^\circ \leq \alpha \leq 12^\circ$
TOTAL PRESSURE	P_o	1 atm
AMBIENT TEMPERATURE	T	293.15 K
MACH NUMBER	M	0.258

The fourth case, denominated in this investigation as Case 3 Compressible, was a variation of the third case presented. The main objective of this case was to determine the effects of the Mach number, i.e., compressibility effects, of the third case on the canopy.

The canopy of Ware & Hassell with the same geometric characteristics as the third case was employed for this analysis, the geometry dimensions were presented in Table

3.7. However, for this analysis the Reynolds and Mach number were maintained similar as the first case by changing the air density and dynamic viscosity. Consequently, a total pressure of approximately $P_o = 4.763$ atm (70 psi) and an ambient temperature of $T = 294.26$ K (70 °F) were determined to change the fluid properties of the air.

From literature, dry air has a critical pressure of 37.36 atm (549 psi) (Air - Thermophysical Properties, 2019). Therefore, differences of the air density using the Ideal Gas Law, presented in Equation (E.3), were neglected.

According with a technical report by Crane, the Sutherland's formula determines the air dynamic viscosity with a difference less than 10% for pressure changes up to 35 atm (514 psi), approximately (Crane, 1982). Therefore, the air dynamic viscosity was calculated using Sutherland's formula, presented in Equation (E.5). Table 3.8 presents the flow conditions for this case.

Table 3.8
Fluid flow conditions and run parameters for the analysis of Case 3 Compressible.

DESCRIPTION	PARAMETER	VALUE
FLOW VELOCITY	V	53 ft/s
AIR DENSITY	ρ	0.01343 slug/ft ³
REYNOLDS NUMBER	Re	2.730×10^6
AIR DYNAMIC VISCOSITY	μ	3.848×10^{-7} slug/(s ft)
ANGLE OF ATTACK	α	$0^\circ \leq \alpha \leq 12^\circ$
TOTAL PRESSURE	P_o	4.763 atm
AMBIENT TEMPERATURE	T	294.26 K
MACH NUMBER	M	0.047

The fifth case consisted on the analysis of the canopy with the same geometry dimensions and flow parameters as the third case. However, for this case the domain size was adjusted to the dimensions as the wind tunnel test section. The main objective of this case was to determine the effects caused by the walls of the test section. Figure 3.18 shows the domain size for this case.

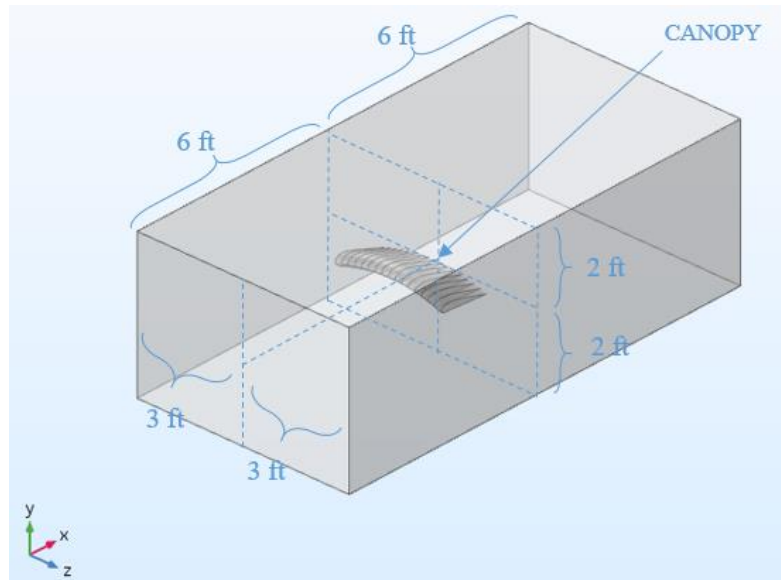


Figure 3.18 Rectangular cuboid, CFD fluid flow domain with dimensions of the wind tunnel test section.

In addition, the following boundary conditions were changed for the analysis:

- Upstream boundary domain wall. Inlet velocity field $f(x, y, z)$ as function of the angle of attack α .

$$x = V$$

$$y = 0$$

$$z = 0$$

Where V is the freestream velocity.

- Top, Bottom and Side domain walls. Walls with no-slip condition, $\vec{V} = 0$.

To simulate the change of angle of attack in the velocity, the canopy geometry was rotated for each angle of attack. Finally, the canopy geometry dimensions along with the flow conditions for this case, corresponding to standard sea level conditions, are presented in Table 3.7.

3.2.8. Test Matrix

A summary of the test cases for the CFD analysis is presented in Table 3.9.

Table 3.9
CFD test matrix.

ANALYSIS TYPE	SIMULATION CASE	CANOPY MODEL		REYNOLDS NUMBER		DOMAIN SIZE		OBJECTIVE
		WARE & HASSELL	WARE & HASSELL WITH KITE CHORD LENGTH	HIGH	LOW	10 CHORDS LENGTH	WIND TUNNEL TEST SECTION	
				2.73×10^6	5.46×10^5			
REYNOLDS NUMBER SENSITIVITY	1	✓		✓		✓		VALIDATION
	2	✓			✓	✓		COMPARISON
DOMAIN SIZE SENSITIVITY	3		✓	✓		✓		COMPARISON
	3 COMPRESSIBLE		✓	✓		✓		COMPARISON
	4		✓	✓			✓	COMPARISON

The multiple simulation cases were compared as follow:

- Case 1 with experimental data from literature for validation.
- Case 2 with Case 1 to determine the effects caused by low Reynolds number.
- Case 3 with Case 1 to determine the effects caused by scaling the canopy geometry.
- Case 3 Compressible with Case 3 to determine the effects of fluid flow compressibility.
- Case 4 with Case 1 to determine the effects caused by the walls of the wind tunnel.

Finally, each one of the cases was compared with experimental data from the investigation of (Nicolaidis, 1971), who tested a canopy with similar geometry characteristics and fluid flow conditions as compared with (Ware & Hassell, 1969).

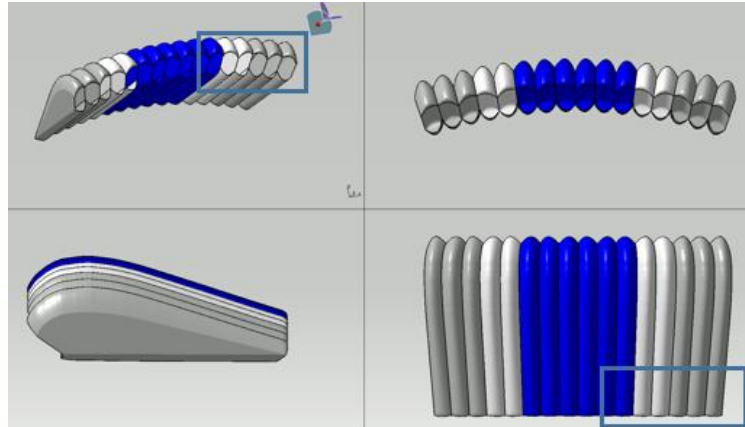
4. Results and Discussion

4.1. Introduction

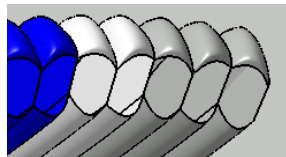
The present chapter summarizes the main outcomes obtained for the different studies performed in this investigation. The chapter starts with various canopy models presented as result of the CAD geometry development, including different design features, structure deformations and CAD development limitations. Additionally, results of the CFD analysis for the different cases of the test matrix in Table 3.9 are presented, including a comparison with experimental data from the literature and possible sources of differences.

4.2. Geometry Creation

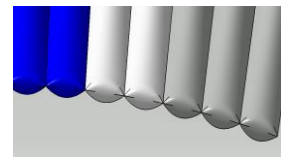
The CAD generation methodology presented in Chapter 4 was employed to develop multiple canopies with different structures implementing design parameters and surface deformations. Figure 4.1 presents the canopy of Ware & Hassell with multiple deformations on the structure. As a reminder, this canopy presented a rectangular planform shape, 16 chambers and the end cells had a rib connecting the upper and lower surfaces. Moreover, the canopy had a chord length of 8.57 ft and an *AR* of 2.



a) Isometric, front, top and side view of the canopy.



b) Opening Inlet and curved surfaces.



c) Canopy TE.

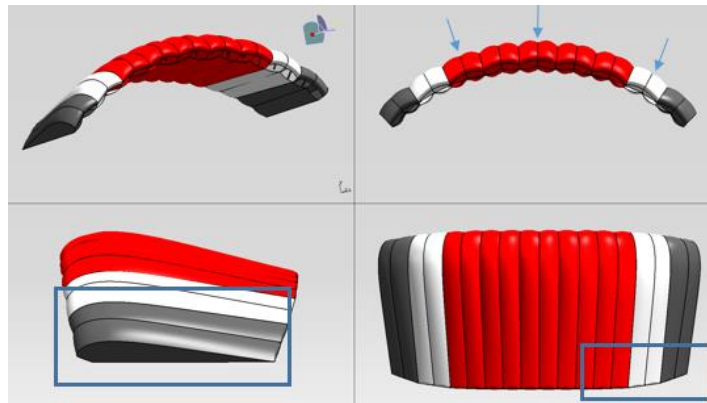
Figure 4.1 Canopy model 1, Ware & Hassell with multiple deformations.

The CAD generation enabled the modeling of different distortions in the canopy structure. For instance, the circular curvature of the canopy, i.e., the anhedral arc, as presented in the front view of the canopy in Figure 4.1a.

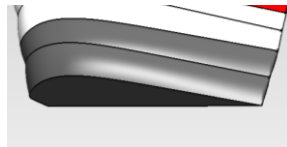
Manipulation of the splines created in between the ribs enabled the curvature of the surfaces to simulate inflation, as presented in Figure 4.1b. Additionally, the splines defined the opening inlet high along with the round shape at the LE of each chamber, as presented in Figure 4.1b. Finally, the round shape at the canopy TE was also simulated using the splines, as presented in Figure 4.1c.

A similar canopy was created using the same process, presented in Figure 4.2. This canopy had an incidence angle for the non-loaded ribs, simulating the suspension lines effects on the loaded ribs, as shown with the arrows in Figure 4.2a. Additionally, the end cells of the canopy had an airfoil rib, as presented in Figure 4.2b, similar to canopy of

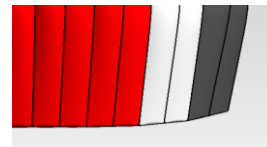
Ware & Hassell from Figure 4.1a. Moreover, this canopy presented an elliptical planform shape, which was simulated by changes of the chord length of the ribs near the canopy tips, as presented Figure 4.2c. Finally, the canopy presented in Figure 4.2 had an AR approximately of 2.6.



a) Isometric, front, top and side view of the canopy.



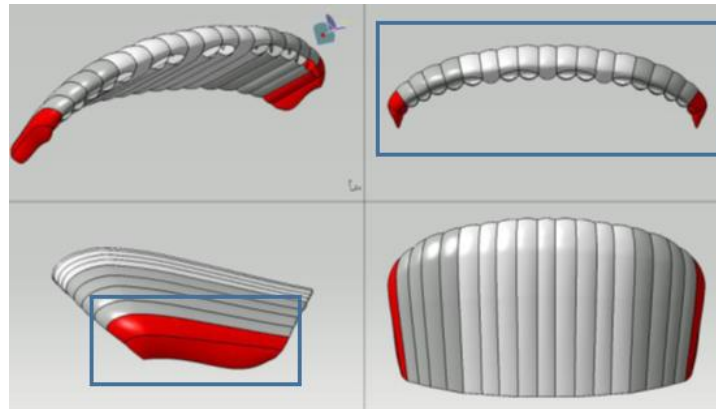
b) Canopy end cell rib.



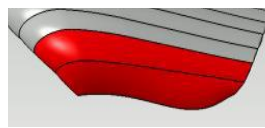
c) Canopy TE.

Figure 4.2 Canopy model 2 (Coe & LeBlanc, 2016).

A more complex canopy geometry is presented in Figure 4.3. This canopy consisted on a higher number of chambers, thus number of ribs, as presented in Figure 4.3a. Furthermore, the curvature of the canopy, as shown in Figure 4.3c, was simulated as an elliptical shape by importing the coordinate points of the ribs which implicitly contained this geometry characteristic, as compared with the circular curvature of the canopy form Figure 4.1a.



a) Isometric, front, top and side view of the canopy.



b) Canopy end cell rib.

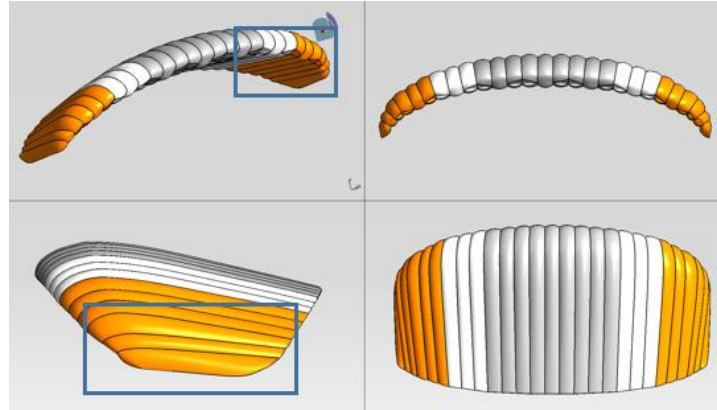


c) Front view.

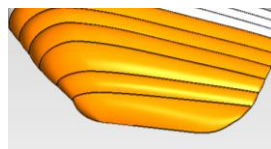
Figure 4.3 Canopy model 3 (Coe & LeBlanc, 2016).

Additionally, the end cells had a single sewing connection between the upper and the lower surfaces, which was imported from a cloud of points, as presented in Figure 4.3b. Modeling of this connection presented multiple challenges using the *Multi-Section Surfaces* tool because of the sharp corner at the LE. Additionally, the round shape at the TE of each chamber was partially modeled using the *Fill* tool because of the short clearance available to create tangency constraints between the surfaces. This canopy had an *AR* approximately of 2.6.

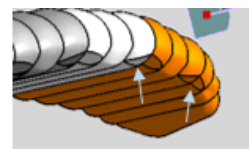
In the same manner, Figure 4.4 presents a canopy with a more complex structure. The end cells presented a smoother single sewing connection, as presented in Figure 4.4b, compared as the end cell from Figure 4.3b. Additionally, variation of the input angles α_1 and α_2 defined the high of the opening inlet, as shown with the arrows in Figure 4.4c. This canopy had an *AR* approximately of 2.8.



a) Isometric, front, top and side view of the canopy.



b) Canopy end cell rib.



c) Canopy LE.

Figure 4.4 Canopy model 4 (Coe & LeBlanc, 2016).

The methodology for the CAD generation to model the canopy structure presented in this investigation was able to implement multiple design parameters such as chord and span length, airfoil and planform shape, size of opening inlet and number of chambers and ribs. Additionally, this methodology included various distortions such as surface inflation, anhedral arc, and incidence and translation of non-loaded ribs. However, various limitations with sharp corners and smooth surface transitions were presented with the CAD tools employed. Depending on the complexity of the canopy geometry, the CAD generation of a single canopy may take from a few days up to a week for completion.

The CAD generation methodology provided a more realistic 3D shape of ram-air parachutes for further studies of the aerodynamic performance, stresses and deformations on the structure, e.g., CFD, FE and FSI analysis.

4.3. Computational Analysis

The multiple simulation cases of the CFD test matrix, presented in Table 3.9, along with results and discussion of possible sources of error are presented in this section.

In addition, the numerical results were compared with experimental data from investigations of (Nicolaidis, 1971) and (Ware & Hassell, 1969). These investigations provided the aerodynamic characteristics under similar flow conditions for a rectangular canopy with a chord length of 8.57 ft, planform area of 147 ft² and an AR of 2.

The values of C_L , C_D and L/D for various angles of attack, presented in Figure 2.7 and Figure 2.8. Curves to approximate the scattered data points were determined for comparison purposes of the trends with the numerical results. Figure B.1 in Appendix B presents the approximation curves and the experimental data points digitalized of the C_L , C_D and L/D values for the investigations conducted by Nicolaidis and Ware & Hassell. Additionally, notice that the experimental data points digitalized correspond to the tests performed with a flow velocity of 50 ft/s and the tether method employed in the investigations. These authors applied a correction for the drag to obtain the values of just the canopy because of the unexposed lines effects during the experimental tests. This correction was implemented by subtracting an empirical value determined by the authors. Consequently, Figure B.1.b presents the C_D of the canopy only, i.e., corrected for the suspension lines effects.

Finally, Figure D.1 in Appendix D presents a summary of C_L , C_D and C_L/C_D for the entire range of angles of attack simulated. Additionally, Table D.1 presents a summary of the calculated values of lift curve slope (a) along with the offset at $\alpha = 0^\circ$ and the percentage of change of a for all the simulation cases compared with Case 1.

4.3.1. Validation of Numerical Results

The first case, Case 1, corresponds to the analysis of the canopy tested by Ware & Hassell under similar flow conditions to validate the CFD methodology presented in chapter 5 and corroborate numerical results. As a reminder, the canopy geometry and the flow conditions are presented in Table 3.2 and Table 3.5, respectively.

Figure 4.5 presents the non-dimensional distance to cell center around the canopy surfaces for an angle of attack of 4° . The non-dimensional distance to cell center is a parameter that determines the accuracy of the results by solving the boundary layer mesh, similar to the y^+ value in other CFD software. The closer or lower to a value of 1, the more reliable are the boundary layer effects on the results.

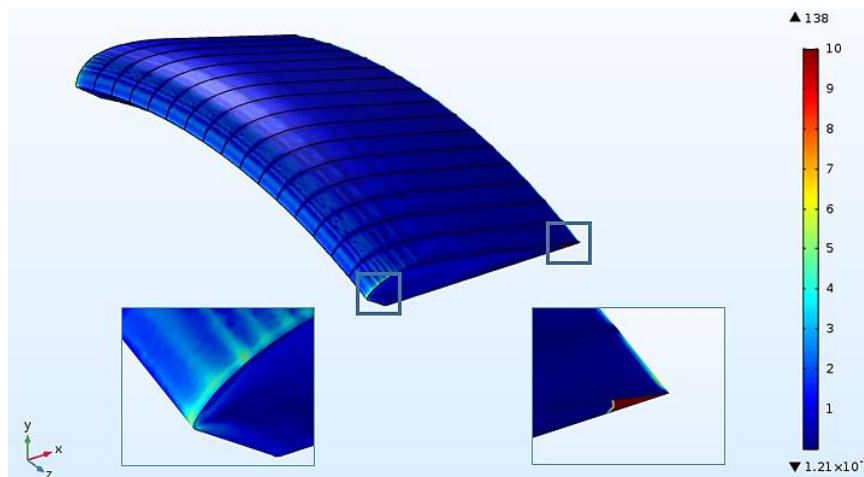


Figure 4.5 Non-dimensional distance to cell center for the canopy surfaces of Case 1 at 4° angle of attack.

The non-dimensional distance to cell center ranged approximately between 3 and 4 for locations near the LE at the top surfaces of the canopy, as shown by the rectangle at the right side in Figure 4.5. The reason of these values can be attributed to locations near the stagnation region, higher velocity gradients presented in the upper surfaces and sudden transition between the upper surface and the rib.

In addition, the highest values were found at the TE of the canopy. The reason for this can be expected because of the difficulty to create prims layers in small areas, e.g., TE corners as shown by the rectangle at the left side in Figure 4.5.

Although small areas of the canopy presented values much higher than 2 for non-dimensional distance to cell center, the canopy surfaces showed an overall value approximately from 0 to 2. Therefore, differences caused by these small areas were neglected, confirming the mesh resolution necessary to solve for the fluid flow around a 3D canopy.

Figure 4.6 shows the numerical results of C_L for various angles of attack in comparison with the experimental data available from literature. The lift curve was in good agreement with the trend of the experimental data for angles of attack up to 8° approximately. For angles of attack higher than 8° , the lift curve remained linear and did not show a stall as compared with the experimental data. The main reason for this difference in the curves was attributed to the flat surfaces at the top and bottom of the canopy for the CFD simulations. Compared to the flexible canopy structure used during the experimental tests, the numerical simulations considered the arched canopy a rigid structure with no deformation effects. Similar to the investigation conducted by Ghoreyshi et al., the C_L curve for a straight rigid canopy remained linear for angles of attack up to 15° approximately, as shown in Figure 2.20a, compared with the experimental results. Finally, parallel to the investigation conducted by Belloc for a rigid arched wing, the C_L curve increased linearly for angles of attack up to 16° with a C_{Lmax} of 0.8 approximately, as presented in Figure 2.10a.

Furthermore, the lift curve also showed an offset at 0° angle of attack compared with

experimental data. This offset in the curves was attributed to slightly differences of the flow conditions between the experimental tests. In addition, the authors mentioned possible differences on the data while measuring the canopy angle of attack by capturing photographs of the ribs at the end cells, especially at low angles of attack. Finally, the lift curve slope was calculated, giving a result of 0.0420 1/deg approximately.

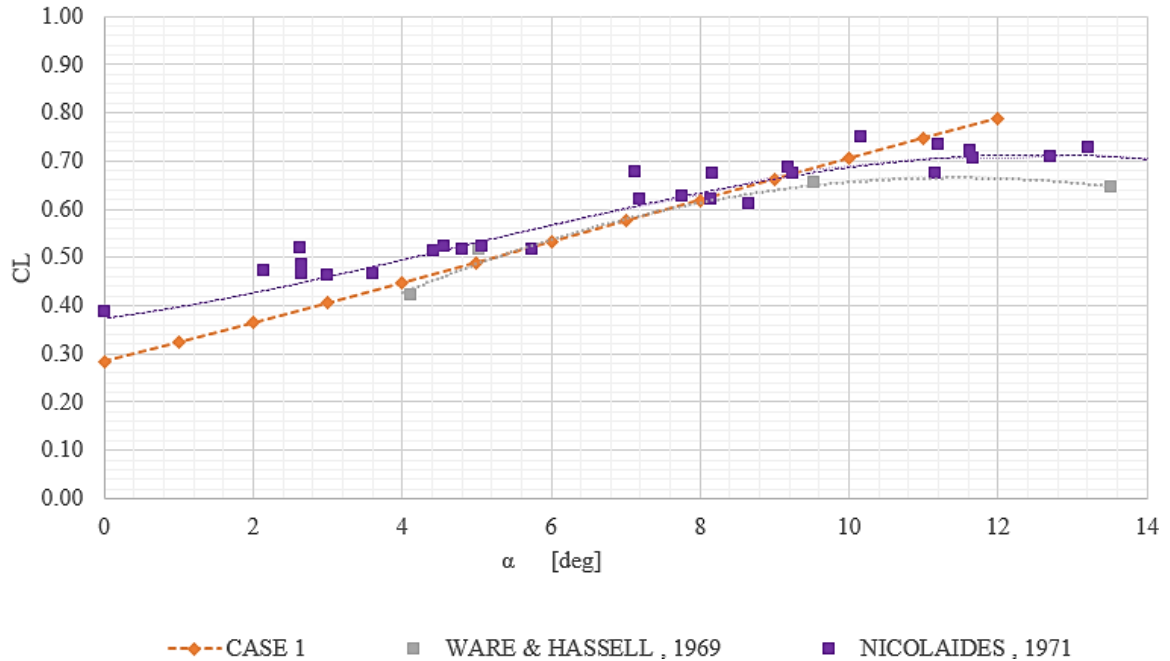


Figure 4.6 C_L versus α of the numerical simulations of Case 1 in comparison with experimental data available from literature.

Figure 4.7 presents the numerical results of C_D for various angles of attack in comparison with the experimental data available. The drag curve shown a similar trend compared with the experimental data for the entire range of angles of attack simulated. However, the numerical results showed a relatively constant offset in the C_D values as compared with the approximation curve of the experimental data. This offset in the C_D values was attributed to effects of multiple factors during the experimental tests and the numerical simulations. The implementation of an empirical approximation was used to

correct the drag values for the unexposed lines effects during the measurements. Moreover, the effects of multiple distortions and roughness in the fabric causes an increment of the pressure and profile drag of the canopy structure for the measurements during the experimental tests. Additionally, possible differences added by the equipment employed such as the guide lines to maintain the canopy stable in the test section during the measurements. Finally, differences caused by the prism layers resolution and the turbulent model selected to solve for the viscous stresses within the boundary layer around the canopy surfaces.

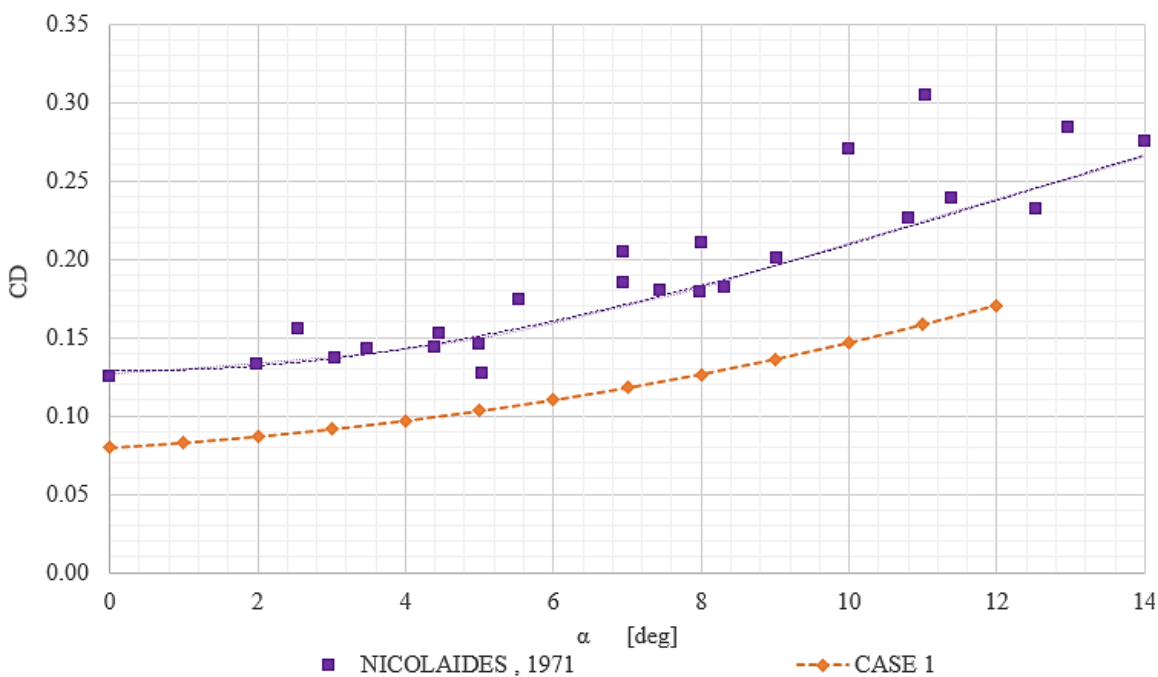


Figure 4.7 C_D versus α of the numerical simulations of Case 1 in comparison with experimental data.

Figure 4.8 C_L versus C_D of the numerical simulations of Case 1 in comparison with experimental data. The drag polar showed a similar trend compared to the experimental data. However, the numerical results showed an offset with the C_D values. The aforementioned possible sources of error in the drag values were reflected in the drag

polar with a displacement of the curve to the left side. Finally, the maximum lift to drag ratio, L/D_{\max} , was obtained at 8° angle of attack, giving a result of 4.89 approximately. According to the experimental data from the literature, for this particular canopy geometry the L/D ranged approximately between 3 and 3.5 for angles of attack tested up to 10° , as presented in Figure 2.7 and Figure 2.8. The numerical analysis showed similar values of L/D as compared with the available data.

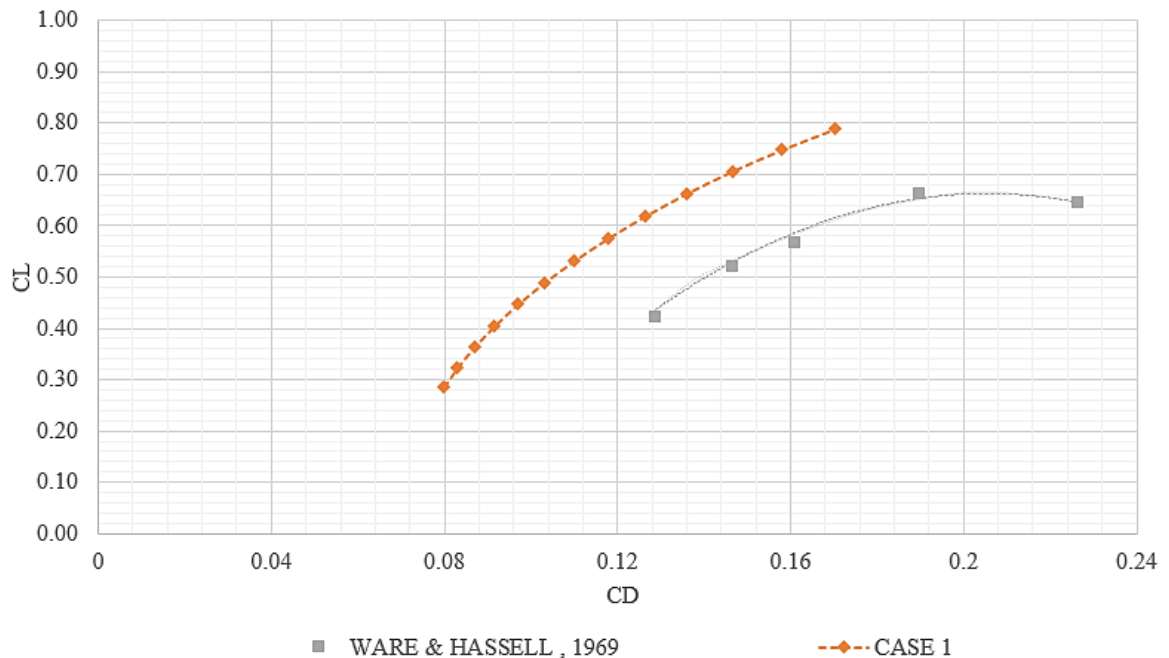


Figure 4.8 C_L versus C_D of the numerical simulations of Case 1 in comparison with experimental data.

4.3.2. Reynolds Number Sensitivity

The second case, Case 2, corresponds to the analysis of the canopy tested by Ware & Hassell for a low Reynolds number. Therefore, the flow velocity was decreased to simulate an average airflow that the kite might experience in a free environment. Additionally, the purpose of this case was to determine the feasibility of experimental tests in a low speed wind tunnel. The canopy geometry and the flow conditions are

presented in Table 3.2 and Table 3.6, respectively.

Figure 4.9 presents the numerical results of C_L for various angles of attack in comparison with Case 1 and the experimental data. The lift curve for Case 2 presented a similar trend with the experimental data for angles of attack up to 9° approximately. In the same manner, the lift curve increased linearly for angles of attack higher than 9° as compared with the experimental data. Compared to the numerical results from Case 1, the lift curve for Case 2 presented an offset of 2% at 0° angle of attack, displacing the curve downwards. Additionally, the lift curve slope was 0.0407 1/deg approximately, 3% less compared with the lift curve slope of Case 1.

Even though the analysis of this case consisted on the flow simulation at a low Reynolds number, 5.45×10^5 , the results obtained for the lift curve slope showed a small difference compared to Case 1, which was conducted at a higher Reynolds number of 2.73×10^6 . According to the investigation conducted by Belloc, a Reynolds number of 9.2×10^5 was considered high enough to predict similar boundary layer behavior without the risk of laminar flow separation at the upper surfaces of the parachute (Belloc, 2015).

Consequently, the order of magnitude of the Reynolds number for the experimental tests conducted by Belloc was approximately the same as for Case 2, providing similar results for the lift curve at both low and high Reynolds numbers.

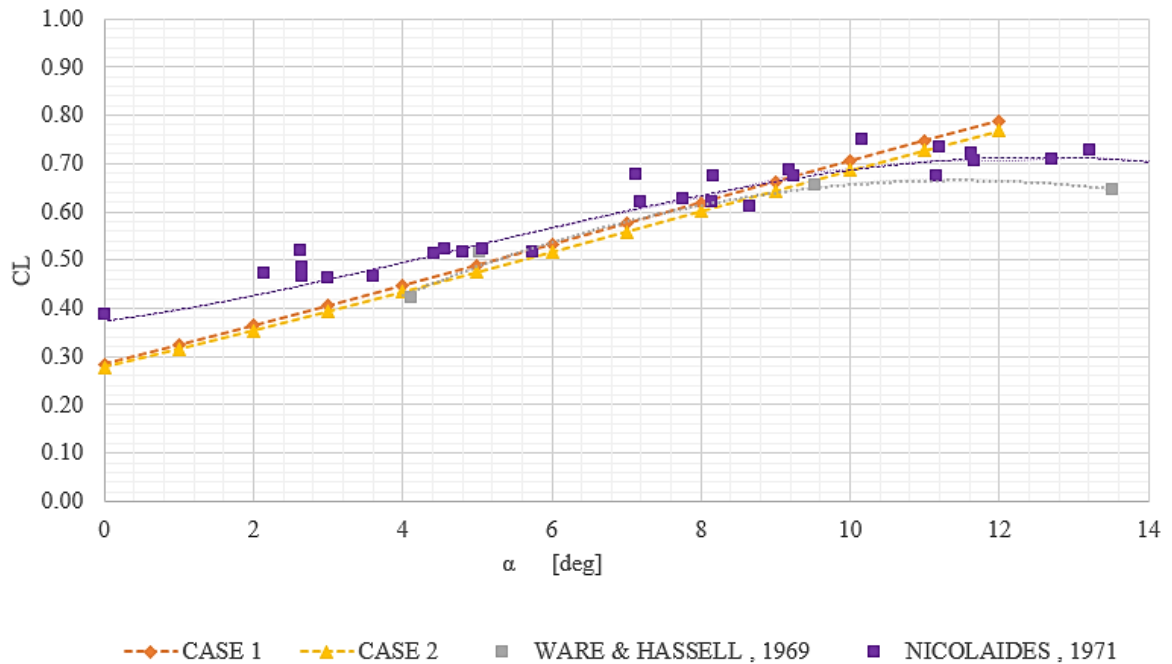


Figure 4.9 C_L versus α of the numerical simulations of Case 2 in comparison with Case 1 and the experimental data.

Figure 4.10 shows the numerical results of C_D for various angles of attack in comparison with the Case 1 and the experimental data. The drag curve presented a similar trend as compared with Case 1 and the experimental data. Similar to Case 1, the drag curve had a relative offset compared with the approximation curve of the experimental data. Additionally, the drag curve had an offset of 6.9% approximately with respect to Case 1 calculated at 0° angle of attack, shifting the curve upwards. A possible reason for this differences was attributed to the accuracy of the turbulence model and wall treatment to solve for the boundary layer effects at low Reynolds number. Finally, the effects of low Reynolds number, reflected on the friction drag around the canopy surfaces, were considered as another source of the observed differences (Belloc, 2015).

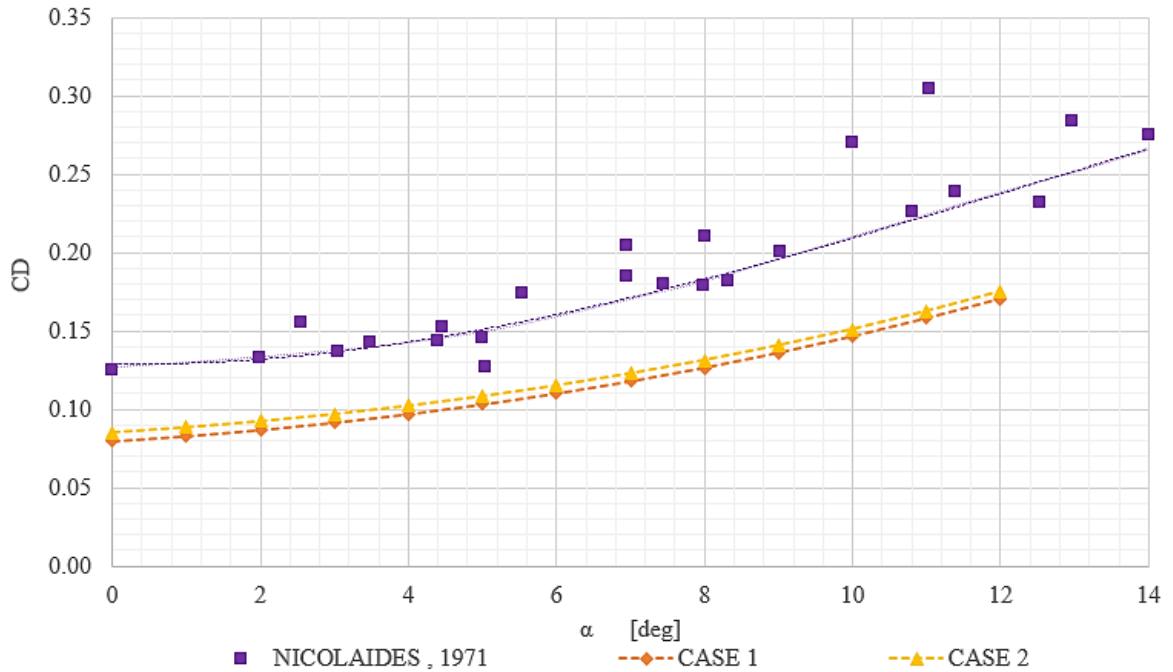


Figure 4.10 C_D versus α of the numerical simulations of Case 2 in comparison with the Case 1 and the experimental data.

Figure 4.11 shows C_L versus C_D of the numerical simulations of Case 2 in comparison with Case 1 and the experimental data. The drag polar presented a similar trend compared to Case 1 and the experimental data provided. However, the multiple variations on the lift and drag curves as compared with the Case 1 were reflected in a displacement of the lift to drag curve to the right, closer to the experimental data. Finally, the maximum lift to drag ratio, L/D_{\max} , for this case was obtained at 8° angle of attack, giving a result of 4.57, approximately 6.47% less as compared with Case 1.

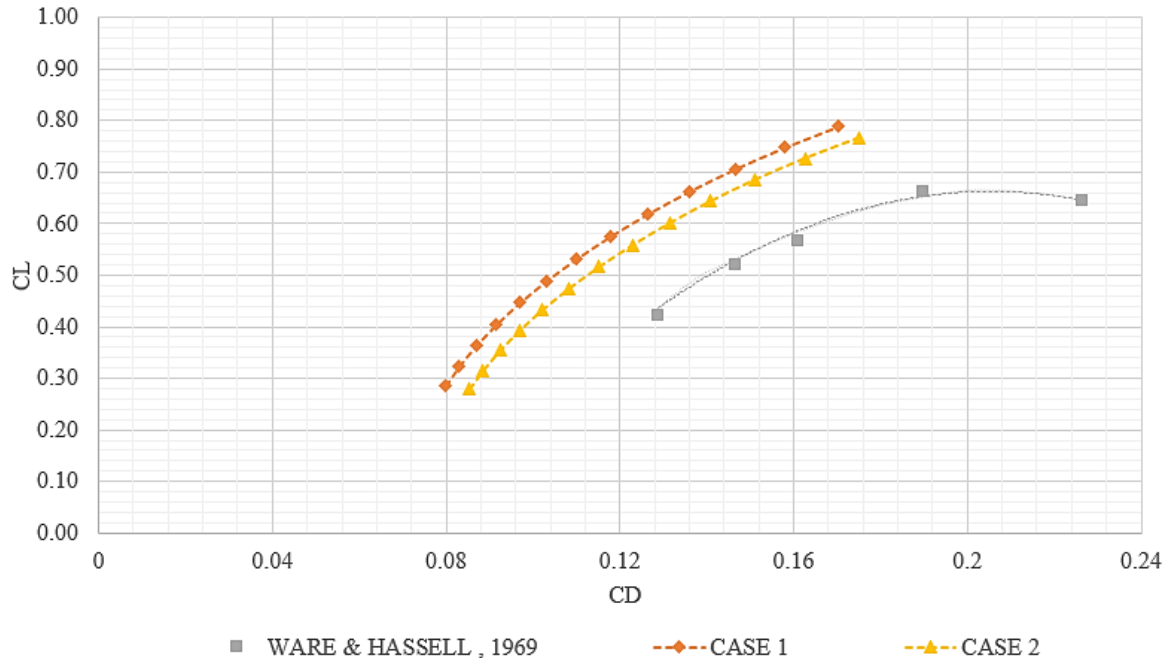


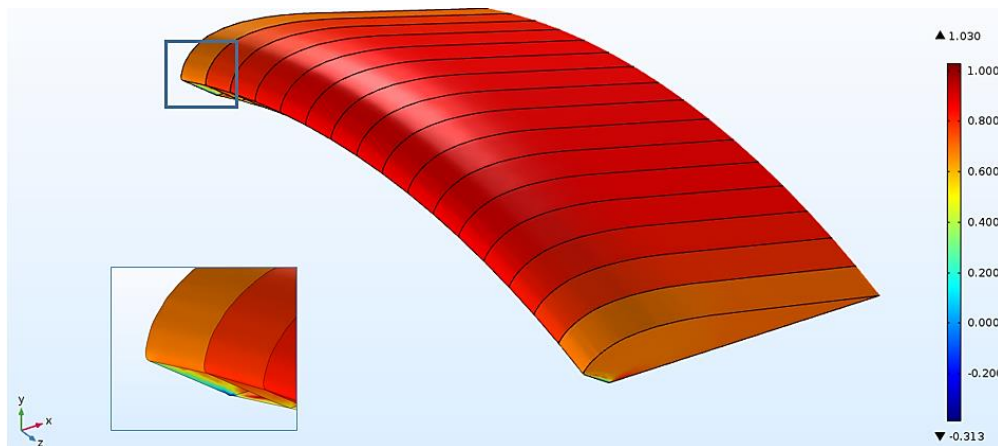
Figure 4.11 C_L versus C_D of the numerical simulations of Case 2 in comparison with the Case 1 and the experimental data.

Figure 4.12 shows the internal surface pressure on the canopy normalized with respect to the free-stream dynamic pressure for Case 1 and Case 2 at 4° angle of attack. There was a constant distribution of the internal pressure within the chambers of the canopy. According to Fogell, this internal pressure is close to the stagnation pressure, providing with rigidity to the flexible canopy structure. However, the end cells for both cases had a lower surface pressure, as shown by the rectangles in Figure 4.12a and Figure 4.12b. Therefore, parachute designs implement multiple crossports in the ribs, i.e., fabric cutoffs, for better pressure distribution along the spanwise direction. These cutoffs are primarily located in the ribs near the end cells to increase the pressure and prevent the structure from collapse.

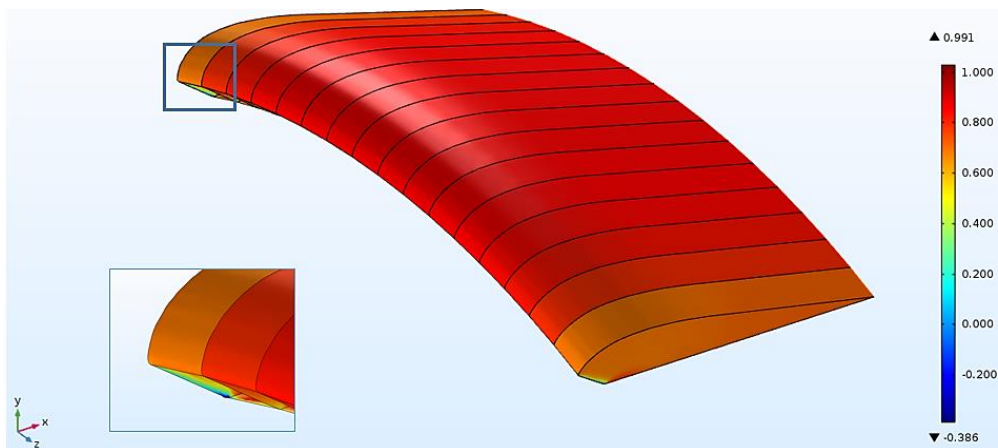
Even though the lift and drag curves for Case 2 resembled the numerical results of Case 1, the normalized values of the internal pressure surface acting on the canopies were

different. For instance, the highest normalized pressure value for Case 1 was approximately of 1.03, close to numerical results from studies using similar canopy geometries and flow conditions, e.g., investigations by Fonseca, Eslambolchi et al. and Peralta et al.

Although the numerical simulations for Case 2 considered a rigid structure, the normalized pressure value was approximately of 0.991. Consequently, the low internal pressure obtained may lead to a structure collapse of this particular canopy geometry during experimental tests under the simulated flow conditions.



a) Canopy for Case 1.



b) Canopy for Case 2.

Figure 4.12 Internal surface pressure on the canopy normalized with the free-stream dynamic pressure for the Case 1 and Case 2 at 4° angle of attack.

4.3.3. Domain Size Sensitivity

The remaining numerical analysis: Case 3, Case 3 Compressible and Case 4, were performed using the canopy tested by Ware & Hassell scaled to match the same chord length of the kite model. Additionally, Case 4 consisted on changing the computational domain with the same dimensions of a wind tunnel test section. The main purpose of these simulations was to determine the feasibility of experimental tests in a low speed subsonic wind tunnel. As a remainder, the geometry characteristics and flow conditions for the various cases are given in Table 3.7 and Table 3.8. Finally, dimensions of the two computational domains are given in Figure 3.11 and Figure 3.18.

Figure 4.13 shows the numerical results of C_L for Case 3, Case 3 Compressible and Case 4 for various angles of attack in comparison with Case 1 and the experimental data available from literature. The lift curves for the three cases resembled as the lift curve obtained for Case 1 and the numerical data. Additionally, the values of lift increased linearly for angles of attack up to approximately 8° for all three cases. However, the curves showed differences of both the lift curve slope and an offset value as compared to the numerical results of Case 1. Moreover, the lift curves for the Case 3 and Case 3 Compressible showed a slower increment rate for angles of attack higher than 8° .

Case 3 considered only Reynolds number similarity to compare the performance of the scaled canopy model directly with the results of Case 1 by increasing the flow velocity. However, the numerical results of Case 3 showed a decrease of the lift curve slope by 17.4% as compared with Case 1. Therefore, Case 3 Compressible considered Reynolds and Mach number similarities to model the compressibility effects because of scaling the canopy dimensions.

Results of the lift curve slope for Case 3 Compressible did not show a major change compared with Case 3, as expected. Consequently, the aforementioned behavior of the lift curve may be attributed to multiple geometry scaling and non-linear effects of the flow around the canopy structure. For instance, the presence of effects caused by the low AR of the canopy and components of the velocity normal to the wing near the end cells, as explained in investigations by (Lingard, 1995), (Iosilevskii, 1996) and (Hoerner & Borst, 1985). Finally, further investigations of these non-linear effects may corroborate the presented results between Case 3 and Case 3 Compressible.

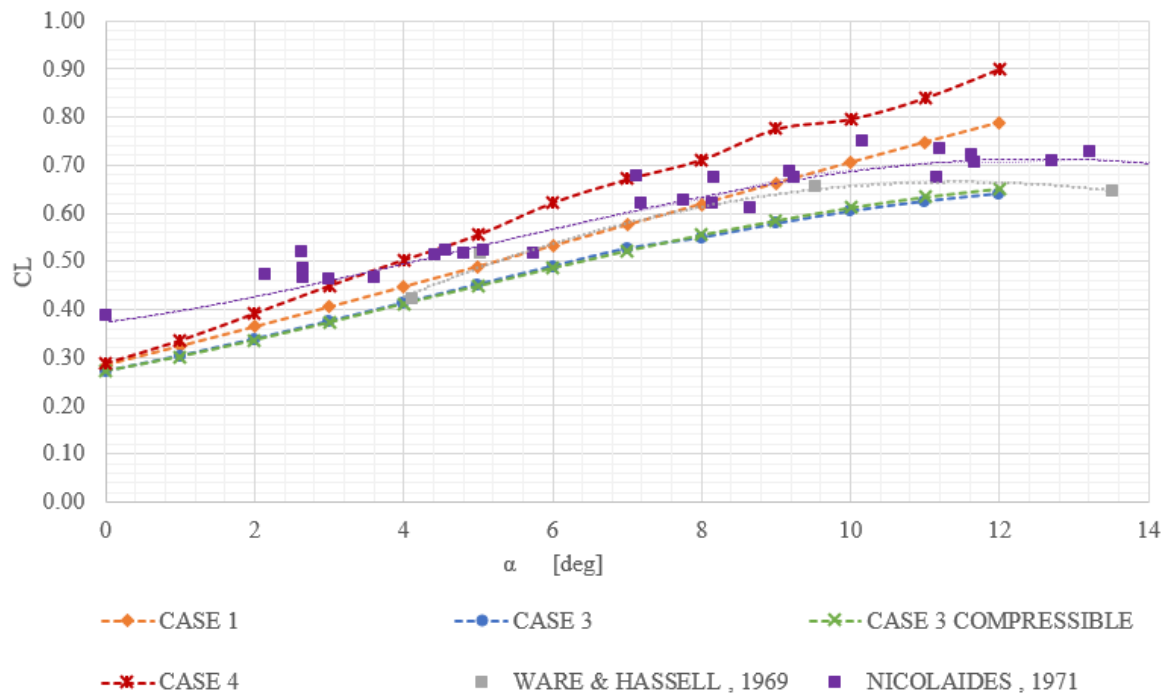
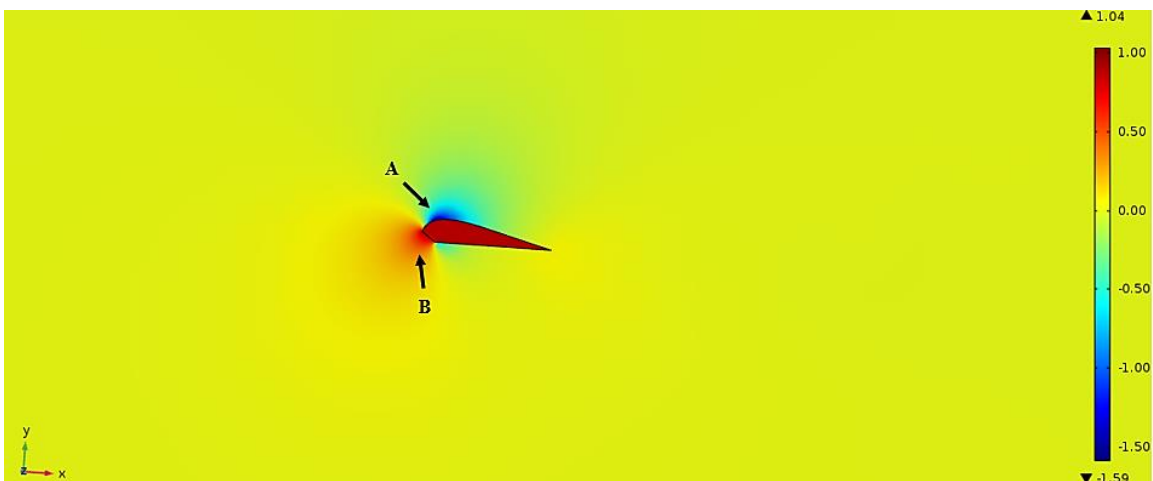


Figure 4.13 C_L versus α of the numerical simulations of Case 3, Case 3 Compressible and Case 4 in comparison with Case 1 and the experimental data.

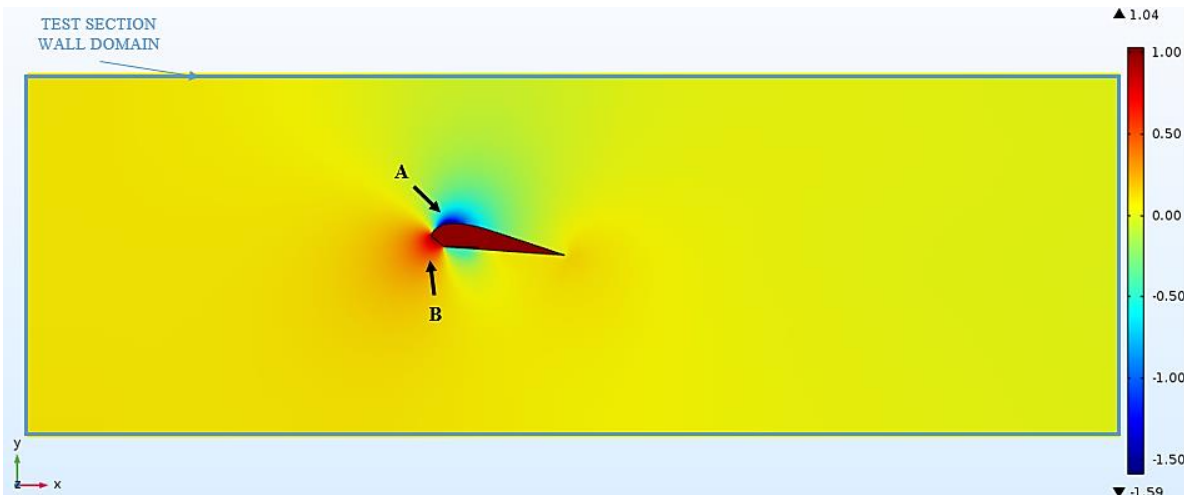
The modification of the computational domain with the dimensions of the wind tunnel test section influenced on the results obtained for Case 4. For instance, the numerical results for Case 4 presented an increment of the lift curve slope approximately of 26% as compared to Case 1, as shown by the red line in Figure 4.13.

Figure 4.14 shows the contour pressure plots in a cross-section plane at the center rib of the canopies along the flow direction normalized with respect to the dynamic pressure for Case 1 and Case 4 at an angle of attack of 4° . Notice that for better comparison, the plots were equally scaled. A similar behavior was presented around the canopy surfaces for the contour pressure plots. For instance, flow acceleration over the upper surfaces generated a low-pressure region near the LE of the canopy, shown in blue color indicated by the arrows **A**. Additionally, a stagnation region near the LE, at the front of the opening inlet, was created because of flow deceleration, shown in red color indicated by the arrows **B**. However, the pressure ranges showed that Case 1 had smaller pressure variations around the canopy surfaces as compared to Case 4. The clearance between the canopy surfaces and the test section walls was the primary reason because the pressure did not fully expanded in the domain size of the test section.

Finally, the increment on lift may be attributed to changes of the dynamic pressure along the test section because of the blockage area (Barber & Johari, 2001). Barber and Johari emphasized the implementation of a correction in the dynamic pressure and drag because of walls effects for hemispherical parachutes with a blockage area up to 22%.



a) Contour pressure plot for Case 1.



b) Contour pressure plot for Case 4.

Figure 4.14 Contour pressure plots in a cross section plane at the center rib of the canopies along the flow direction for Case 1 and Case 4 at an angle of attack of 4°, normalized by the dynamic pressure.

Table 4.1 gives a summary of the calculated values of the lift curve slope (a), the percentage of change of the lift curve slope and offset at $\alpha = 0^\circ$ for the three cases as compared to Case 1. Notice the sign for the percentage of change for the lift curve slope and offset value. A positive sign denotes an increment value, while a negative denotes a decrement value with respect to Case 1. Finally, notice that the location of the low-pressure region in the upper surface affected mainly the lift value compared with the drag generated by the canopy, as explained later in this section.

Table 4.1

Values of lift curve slope (a), percentage of change in lift slope and offset at $\alpha = 0^\circ$ for Case 3, Case 3 Compressible and Case 4 as compared with Case 1.

SIMULATION CASE	a (1/deg)	CHANGE OF a (%)	OFFSET AT $\alpha = 0^\circ$ (%)
CASE 3	0.0347	-17.4	-4.7
CASE 3 COMPRESSIBLE	0.0354	-15.7	-4.7
CASE 4	0.0529	+26	+1.4

Figure 4.15 shows the numerical results of C_D versus α for Case 3, Case 3 Compressible and Case 4, respectively, in comparison with Case 1 and the available experimental data.

The numerical results of drag obtained for the three cases presented the same trend as compared with Case 1. Additionally, the three curves showed a similar constant offset for all the angles of attack simulated when compared with the experimental data available.

Even though Case 3 considered only Reynolds number similarity for the simulations, the scaled dimensions of the canopy did not affect the drag values. Case 3 presented an offset of approximately 8.5% calculated at 0° angle of attack, shifting the curve upwards as compared with Case 1.

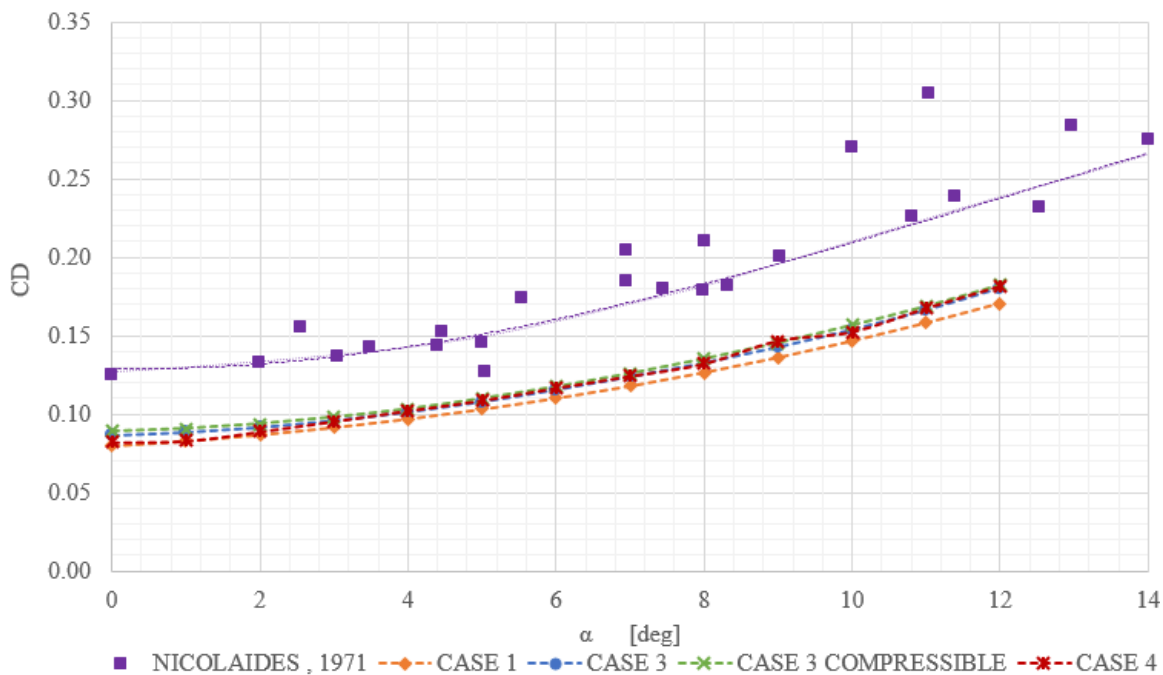


Figure 4.15 C_D versus α for the numerical simulations of Case 3, Case 3 Compressible and Case 4 in comparison with the Case 1 and the experimental data.

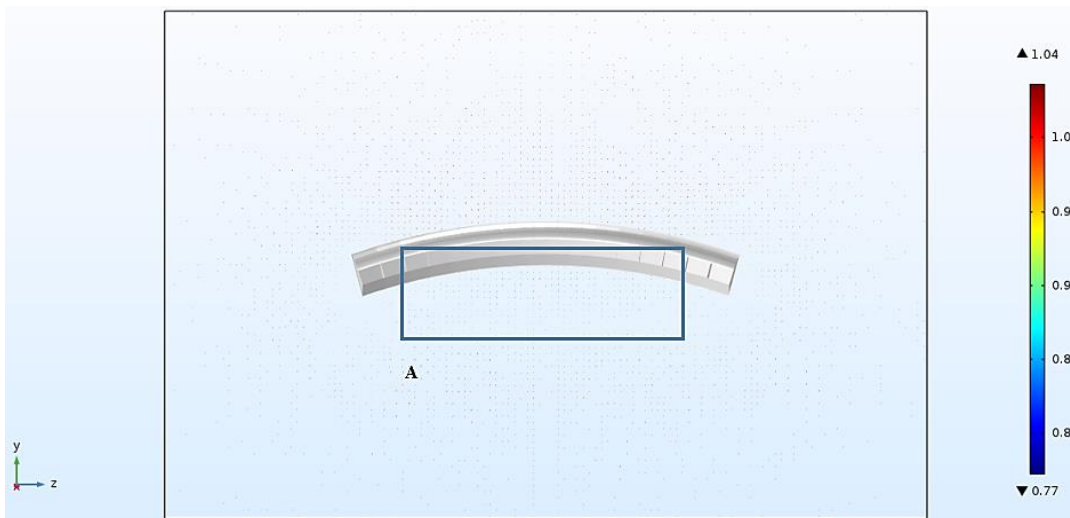
In the same manner, results for Case 3 Compressible did not show major changes in the values of drag coefficient. Although this case considered Reynolds and Mach number

to simulate the scaling and compressibility effects, this case gave an offset of approximately 10.3% at 0° angle of attack, shifting the curve upwards as compared to Case 1.

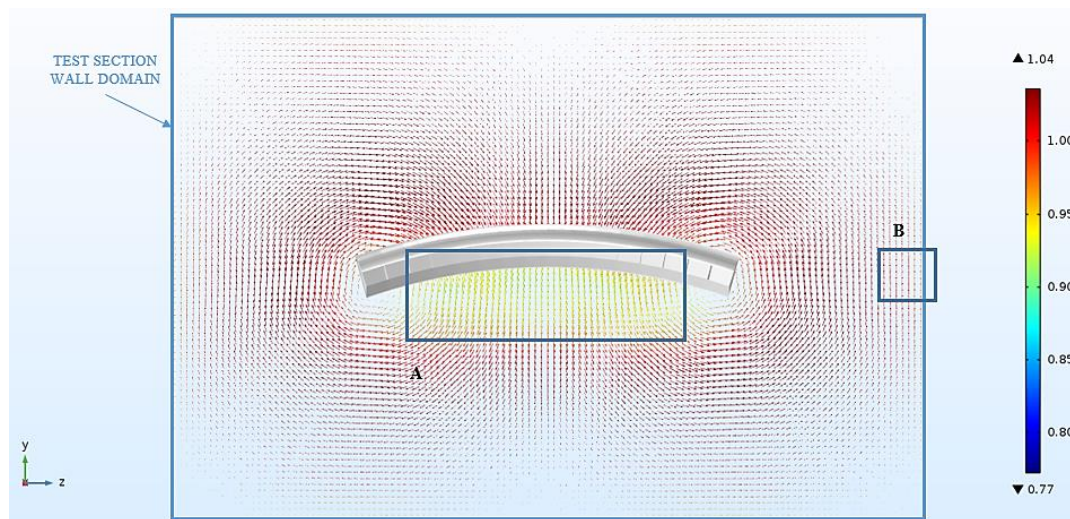
The results for Case 4 showed a similar trend as compared with Case 1. An offset was determined at 0° angle of attack of approximately 3% as compared to Case 1. However, the drag increased at a higher rate than the other cases. A possible reason for this increase was attributed to changes in the dynamic pressure and have the drag coefficient in the test section because of blockage effects (Barber & Johari, 2001). Therefore, the percentage of blockage area was estimated using the projected area of the canopy model and the cross-section of the test section for both cases. Refer to Appendix C for more detail for the calculation of the blockage area of the canopies in the wind tunnel test sections.

The blockage area estimated for Case 1 ranged from 2% to 3% approximately when the angle of attack increased from 0° up to 12° . In the same manner, the blockage area for Case 4 ranged from 4% to 7% approximately when the angle of attack increased from 0° up to 12° . Therefore, wall effects caused by blockage area were expected higher on the numerical results for Case 4.

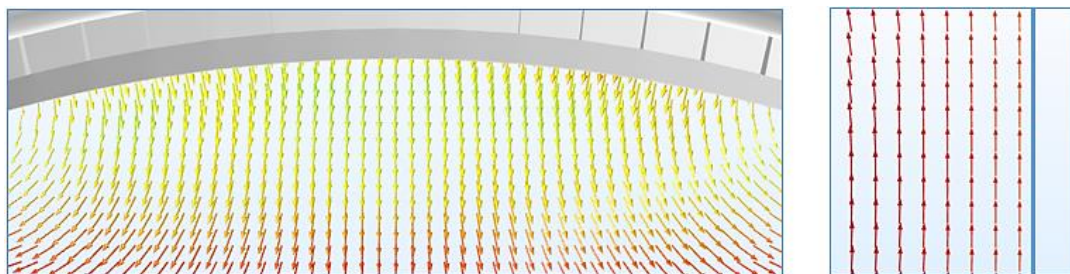
Figure 4.16 shows velocity vectors normalized with respect to the free-stream airspeed in a plane located one chord length downstream from the TE of the canopies for Case 1 and Case 4 at an angle of attack of 4° . Notice that the length of the arrows denotes the magnitude of the velocity in the y - z plane, whereas the color of the arrows denotes the velocity magnitude in the x , y and z directions.



a) Flow field velocity for Case 1.



b) Flow field velocity for Case 4.



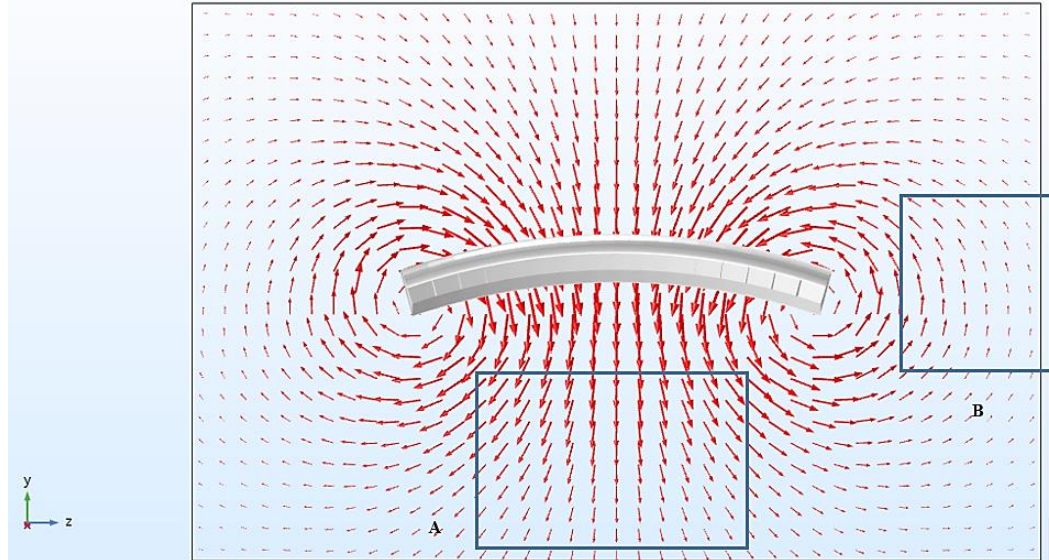
c) Views A and B for Case 4.

Figure 4.16 Velocity vectors normalized with respect to the free-stream airspeed in a plane located one chord length downstream from the TE of the canopies for Case 1 and Case 4 at an angle of attack of 4° .

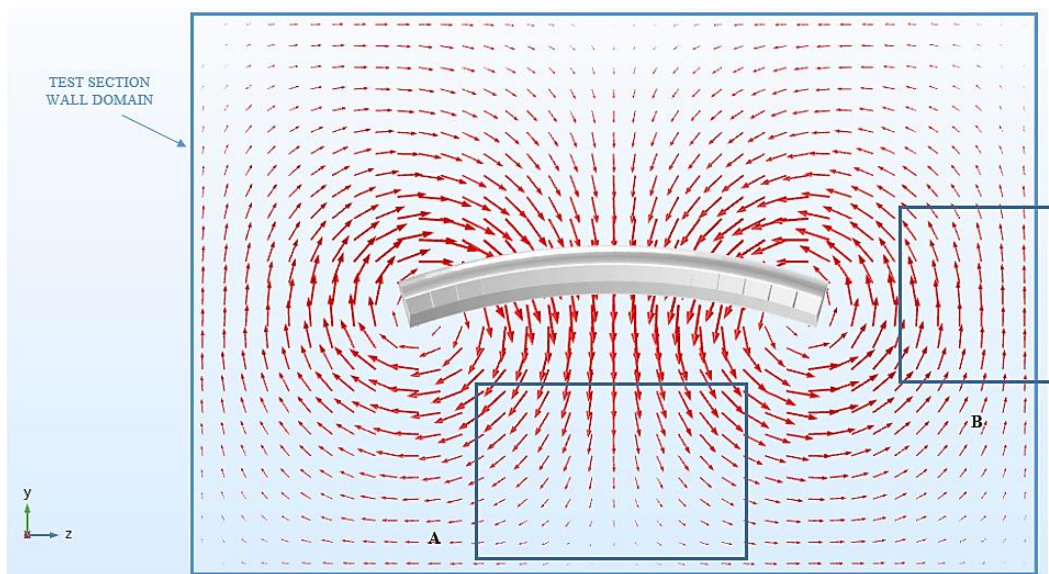
The flow pattern showed the vortices created because of the difference of pressure between the upper and lower surfaces of the canopy. Notice that the velocity in the y - z plane was minimum as the flow moved downwards, as shown by the rectangle **A** in Figure 4.16a. Additionally, the strength of the vortices decreases as the flow was far away from the canopy surfaces, so decreasing the induced drag.

In the same manner, the velocity vectors for Case 4 differently from Case 1; the velocities in the y - z plane of the flow moving downwards were considerable, as shown with the rectangle **A** in Figure 4.16b. Additionally, the vortices magnitude did not disappear completely because of the small clearance between the canopy surfaces and the test section walls, as shown with the rectangle **B** in Figure 4.16b.

An alternative method to visualize the wall effects on the canopy performance is by normalizing the velocity vectors with respect to the dynamic pressure. Figure 4.17 shows velocity vectors normalized with respect to the free-stream airspeed in a plane located one chord length downstream from the TE of the canopies for Case 1 and Case 4 at an angle of attack of 4° . Notice that the length of the arrows denotes the magnitude of the velocity in the y - z plane. The velocity decreases rapidly in magnitude as moving downwards for Case 4 compared to Case 1, as shown by the rectangles **A** from both cases in Figure 4.17. Additionally, the velocity magnitude is tangent and forced to decrease near the wind tunnel walls for Case 4 compared with Case 1, as shown by the rectangles **B** from both cases in Figure 4.17.



a) Flow field velocity for Case 1.



b) Flow field velocity for Case 4.

Figure 4.17 Velocity vectors normalized with respect to the free-stream dynamic pressure in a plane located one chord length downstream from the TE of the canopies for Case 1 and Case 4 at an angle of attack of 4° .

Figure 4.18 presents C_L versus C_D of the numerical simulations of Case 3, Case 3 Compressible and Case 4 in comparison with the Case 1 and the experimental data. The lift-to-drag curves showed a similar trend compared to Case 1 and the experimental data.

However, the differences on the lift and drag were reflected as displacements of the lift to drag curves for the different cases. For instance, Case 3 and Case 3 Compressible showed a decrease of the lift values for angles of attack higher than 8° .

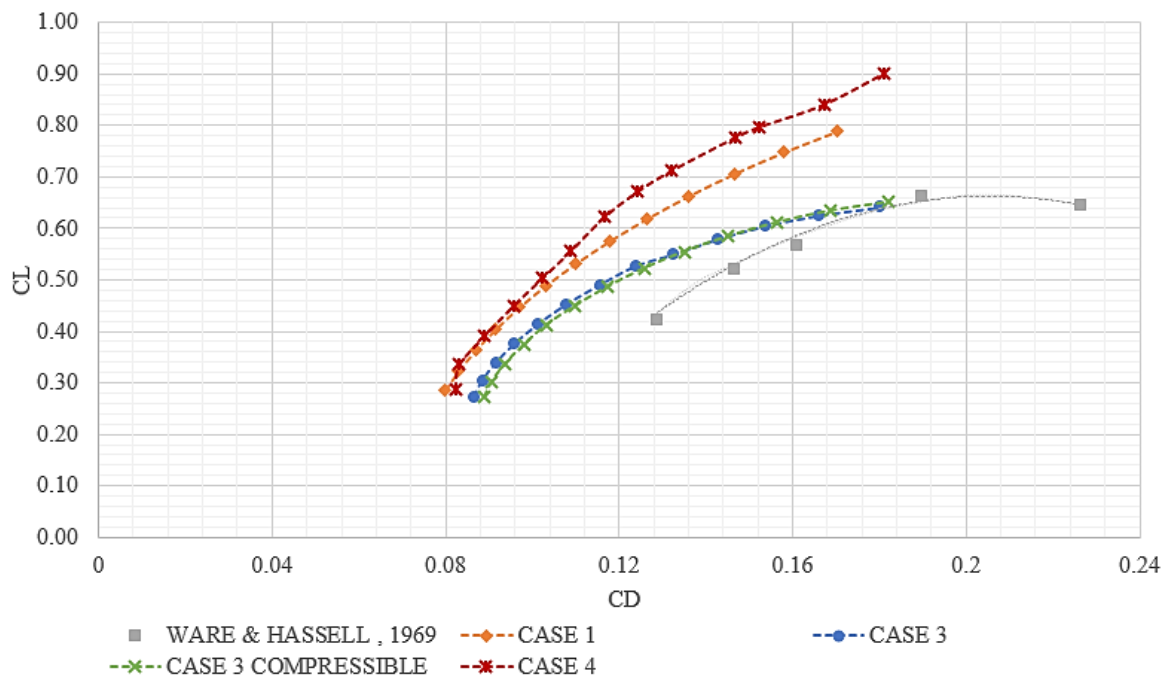


Figure 4.18 C_L versus C_D of the numerical simulations of Case 3, Case 3 Compressible and Case 4 in comparison with the Case 1 and the experimental data.

Finally, the values of L/D_{max} were calculated for the three cases at 0° angle of attack and compared with Case 1, as presented in Table 4.2. Notice the negative sign in the percentage of change in L/D_{max} meaning a decrease with respect Case 1.

Table 4.2

Values of L/D_{max} for Case 3, Case 3 Compressible and Case 4 and percentage of change as compared with Case 1.

SIMULATION CASE	L/D_{max}	CHANGE OF L/D_{max} (%)
CASE 3	4.25	-13.19
CASE 3 COMPRESSIBLE	4.15	-15.2
CASE 4	5.40	+10.45

Results for the numerical analysis presented in this section demonstrated that experimental tests are feasible in a low speed wind tunnel to determine the aerodynamic performance of a scaled canopy model. Multiple simulations under similar flow conditions predicted the flow behavior around the canopy surfaces. The aerodynamic characteristics of C_L , C_D and C_L/C_D for angles of attack ranging from 0° to 12° followed the patterns as compared with numerical data from the literature. Additionally, values of the lift curve slope (a), L/D_{max} and percentages of difference were determined by comparing with the baseline simulation.

However, the numerical results showed differences on the values of C_L , C_D and C_L/C_D , which are because of non-linear effects caused by the low AR of the canopy design, distortions because of the structure flexibility and wind tunnel wall effects. Consequently, experimental tests as well as numerical simulations may require the implementation of correction factors for the lift and drag measurements and scaling effects to predict accurately the aerodynamic performance of ram-air parachutes.

5. Conclusion, Recommendations and Future Work

5.1. Conclusions

The following conclusions have been drawn from the present investigation:

A semi-automatic CAD generation methodology was presented, that was capable of implementing multiple design parameters such as chord and span, airfoil and planform shape, size of opening inlet and number of chambers and ribs. Additionally, this methodology modeled various surface distortions such as surface inflation, anhedral arc, and incidence and translation of non-loaded ribs.

The aerodynamic characteristics of C_L , C_D and C_L/C_D for angles of attack within a range of 0 to 12° were determined for a rigid canopy model from the literature, by performing CFD simulations under multiple flow conditions. Additionally, numerical outcomes were validated with experimental data and direct comparison of the lift curve slopes (a), surface pressure and velocity arrows plots.

Validation of the results showed agreement of the C_L , C_D and C_L/C_D curves with the experimental data from literature. Results of the C_L matched the experimental data for angles of attack up to approximately 8°. Additionally, results of the C_D followed the same trend, corresponding the experimental data with a constant offset for the entire range of angles of attack simulated. Differences were attributed primarily to simplification of the canopy deformations for CFD simulations, effects caused by additional geometry features such as the lines drag during tests and experimental measurement techniques.

Results of Reynolds number sensitivity determined the aerodynamic characteristics of the canopy for a low Reynolds number with a difference less than 6.9%. However, results showed that low flow velocities caused deficiency of internal pressure in the canopy

surfaces, leading to a possible structure collapse considering the dimensions of the canopy.

Results of domain size sensitivity concluded that experimental tests in a low speed wind tunnel are feasible to measure the aerodynamic performance of scaled ram-air parachutes. However, the lift curve slope presented an increase approximately of 26% compared with free air domain analysis. Consequently, implementation of correction factors is recommended to compensate the high interaction of the test section wall effects on the canopy performance.

5.2. Recommendations and Future Work

The present investigation has obtained numerical results of the aerodynamic performance of a scaled ram-air parachute. The results were validated with available data from the literature. Recommendations for future work are as follows:

The present investigation has provided results of the aerodynamic performance of a rigid canopy model. The results were partially validated with experimental data from the literature because of the simplifications for the CFD simulations and measurement techniques during the tests. Consequently, the first recommendation would be to perform experimental tests with a similar canopy geometry and flow conditions to directly validate the CFD methodology.

The design of a 2D force and balance to measure the aerodynamic forces of a canopy model in the test section was discovered. The implementation of this force and balance design inside the wind tunnel test section allows measurement of the resultant forces of a flexible canopy by using suspension lines. However, the design presented limitations to measure large forces because of stability of the system. Therefore, the second

recommendation would be to rebuild the basis of the 2D force and balance by implementing a more solid structure capable to withstand the application of larger forces using the same concept of load measurement.

A CAD generation methodology was developed in this investigation that was capable of creating complex canopy geometries using a wide range of design parameters and implementing surface distortions. However, limitations are in modeling sharp edges and smooth surface transitions. In addition, the time required to fully complete a geometry depends directly on the geometry complexity. Consequently, a third recommendation would be to modify the scripts to optimize process using other design tools available in the software. Additionally, the implementation of different design tools or other software using the same design concept could lead the development of a full automatic CAD generation process.

Finally, the multiple numerical simulations consisted on solving the steady state RANS equations to predict the flow behavior around the canopy structure. Additionally, the turbulence model chosen in this investigation was SST (low Reynolds number) to solve for the boundary layer effects. Therefore, the fourth recommendation would be to validate the present numerical results by performing time dependent simulations with a different turbulent model, e.g., Spalart-Allmaras, to solve for the same flow conditions of the simulations in this thesis.

REFERENCES

- Air - Thermophysical Properties*. (2019, January 14). Retrieved from Engineering Toolbox: https://www.engineeringtoolbox.com/air-properties-d_156.html
- Anderson, J. D. (2010). *Fundamentals of Aerodynamics* (5th ed.). Boston: McGraw-Hill.
- Barber, J., & Johari, H. (2001). *Experimental investigation of personnel parachute designs using scale model wind tunnel testing*. 16th AIAA Aerodynamic Decelerator Systems Technology Conference and Seminar. doi:10.2514/6.20012074
- Belloc, H. (2015). Wind tunnel investigation of a rigid paraglider reference wing. *Journal of Aircraft*, 52, 703-708. doi:10.2514/1.C032513
- Burke, B. (1997). *The Canopy Pilot's Handbook*. Skydive Arizona, Eloy, AZ. Retrieved from <http://clubjumpin.com/wp-content/uploads/2014/03/The-Canopy-Pilots-Handbook.pdf>
- Burnett, B. (2016). *Coupled fluid-structure interaction modeling of a parafoil*. Master Thesis, Embry-Riddle Aeronautical University, Aerospace Engineering, Daytona Beach. Retrieved from <https://commons.erau.edu/edt/294>
- Carney, A. (2007). *Deformation measurement of parachute fabric using imaging and smart material sensors*. Master Thesis, University of Massachusetts, Mechanical Engineering, Lowell, MA.
- Coe, B., & LeBlanc, J. (2016, May). Ram-Air Parachutes Design. (C. A. Guzman, Interviewer) DeLand, FL, United States of America.
- COMSOL. (2017). Documentation. Retrieved March 2018, from <https://cdn.comsol.com/documentation/5.3.0.316/IntroductionToCOMSOLMultiphysics.pdf>
- Crane, C. (1982). *Flow of Fluids through Valves, Fittings, and Pipe*. Technical Paper No. 410 M. Retrieved January 14, 2019, from <https://engkarrar.files.wordpress.com/2013/01/flow-of-fluids-through-valve-fittings-and-pipes.pdf>
- Daneshjo, N., Korba, P., & Eldojali, M. A. (2012). *The CATIA Design Process, Design and Manufacture in Aviation*. Technical University in Košice, Aviation Engineering. Retrieved March 08, 2019, from <https://www.sjf.tuke.sk/transferinovacii/pages/archiv/transfer/23-2012/pdf/194-196.pdf>

- Dassault Systèmes. (2006). Documentation. Retrieved May 2016, from <http://catiadoc.free.fr/online/interfaces/CAAMasterIdx.htm>
- Eslambolchi, A., & Johari, H. (2013). *Simulation of Flowfield around a Ram-Air Personnel Parachute Canopy*. AIAA Aerodynamic Decelerator Systems (ADS) Conference. doi:10.2514/6.2013-1281
- Fogell, N. A. (2014). *Fluid-structure interaction simulations of the inflated shape of ram-air parachutes*. Doctoral Dissertation, Imperial College London.
- Fonseca, A. A. (2018). *A Computational Fluid Dynamics Study on the Aerodynamic Performance of Ram-Air Parachutes*. Master Thesis, Embry-Riddle Aeronautical University, Aerospace Engineering, Daytona Beach. Retrieved from <https://commons.erau.edu/edt/405/>
- Ghoreyshi, M., Bergeron, K., Seidel, J., Jirásek, A., Lofthouse, A. J., & Cummings, R. M. (2016). Prediction of Aerodynamic Characteristics of Ram-Air Parachutes. *Journal of Aircraft*, 53(6), 1802-1820. doi:10.2514/1.c033763
- Hoerner, S. F., & Borst, H. V. (1985). *Fluid-dynamic lift: practical information on aerodynamic and hydrodynamic lift* (2nd ed.). Brick Town, NJ: L.A. Hoerner.
- Iosilevskii, G. (1996). Lifting-line theory of an arched wing in asymmetric flight. *Journal of Aircraft*, 33(5), 1023-1026. doi:10.2514/3.47050
- Jalbert, D. C. (1964). *U.S. Washington, DC Patent No. US3131894A*.
- Lee, C. K., & Li, P. (2007). Geometric Properties of Parachutes Using 3-D Laser Scanning. *Journal of Aircraft*, 44(2), 377-385. doi:10.2514/1.18387
- Lingard, J. S. (1995). *Precision Aerial Delivery Seminar: Ram-Air Parachute Design*. 13th AIAA Aerodynamic Decelerator Systems Technology Conference, Clearwater Beach, FL.
- Macha, J. M., & Buffington, R. J. (1990). Wall-interference corrections for parachutes in a closed wind tunnel. *Journal of Aircraft*, 27(4), 320-325. doi:10.2514/3.25275
- McConnel, J. (2017, August 8). Canopy Pilot Guide. Underwood, Australia. Retrieved February 2, 2019, from https://www.apf.com.au/ArticleDocuments/836/Canopy_Pilot_Guide_v2_20170808.pdf.aspx?Embed=Y
- Mkrtchyan, H., & Johari, H. (2011). *Detailed aerodynamic analysis of ram-air parachute systems in steady flight*. 21st AIAA Aerodynamic Decelerator Systems Technology Conference and Seminar 2011. doi:10.2514/6.2011-2553

- Mohammadi, M., & Johari, H. (2010). Computation of flow over a high-performance parafoil canopy. *Journal of Aircraft*, 47, 1338-1345. doi:10.2514/1.47363
- Nicolaides, J. D. (1971). *Parafoil Wind Tunnel Tests*. Tech. No. 70-146, Air Force Flight Dynamics Laboratory, Notre Dame, IN.
- Ortega, E., Flores, R., & Pons-Prats, J. (2017). Ram-Air Parachute Simulation with Panel Methods and Staggered Coupling. *Journal of Aircraft*, 54(2), 807-814. doi:10.2514/1.c033677
- Peralta, R., & Johari, H. (2015). *Geometry of a Ram-Air Parachute Canopy in Steady Flight from Numerical Simulations*. 23rd AIAA Aerodynamic Decelerator Systems Technology Conference. doi:10.2514/6.2015-2103
- Pinholster, G. (2017, August 30). *Embry-Riddle Acquires Cray Supercomputer to Advance Research*. Retrieved March 14, 2019, from <https://news.erau.edu/headlines/embry-riddle-acquires-cray-supercomputer-to-advance-research/>
- Sobieski, J. (1994). *The Aerodynamics and Piloting of High Performance Ram-Air Parachutes*. Retrieved from <http://skysurfer.com.au/hosted/highperf.pdf>
- The MathWorks, Inc. (2018). Documentation. Retrieved June 2018, from <https://www.mathworks.com/help/>
- Uddin, M. N., & Mashud, M. (2010). Wind Tunnel Test of a Paraglider (flexible) Wing Canopy. *International Journal of Mechanical & Mechatronics Engineering IJMME-IJENS*, 10(3), 7-14. Retrieved August 22, 2016, from https://www.researchgate.net/publication/266493626_Wind_Tunnel_Test_of_a_Paraglider_flexible_Wing_Canopy.
- Ware, G. M., & Hassell, J. L. (1969). *Wind-tunnel investigation of ram-air-inflated all flexible wings of aspect ratios 1.0 to 3.0*. Tech. No. SX-1923, National Aeronautics and Space Administration, Washington, D.C.

Appendices

A. Airfoil Coordinates of Ware & Hassell Canopy Model

Table A.1 presents the airfoil coordinates of the center rib normalized by the chord length for the canopy tested in the literature (Ware & Hassell, 1969). Additional points were approximated by interpolating the provided data presented from literature.

Table A.1
Airfoil coordinates.

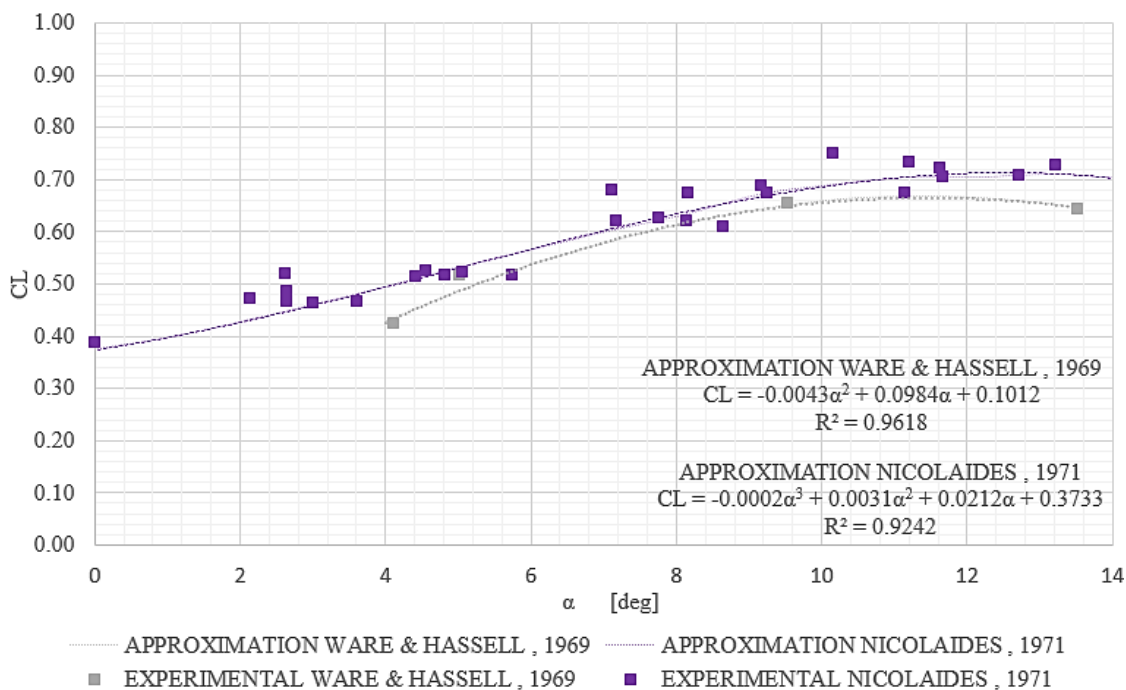
X	Y	Z	X	Y	Z	X	Y	Z
0.0000	0.0000	0.0000	0.9696	0.0528	0.0000	0.7970	0.1783	0.0000
0.5579	0.0000	0.0000	0.9763	0.0576	0.0000	0.7903	0.1783	0.0000
0.5778	0.0000	0.0000	0.9829	0.0624	0.0000	0.7837	0.1783	0.0000
0.5977	0.0000	0.0000	0.9896	0.0671	0.0000	0.7770	0.1783	0.0000
0.6176	0.0000	0.0000	0.9962	0.0719	0.0000	0.7704	0.1776	0.0000
0.6376	0.0000	0.0000	0.9962	0.0774	0.0000	0.7638	0.1769	0.0000
0.6575	0.0000	0.0000	0.9961	0.0828	0.0000	0.7571	0.1761	0.0000
0.6774	0.0000	0.0000	0.9961	0.0883	0.0000	0.7505	0.1756	0.0000
0.6973	0.0000	0.0000	0.9895	0.0989	0.0000	0.7438	0.1751	0.0000
0.7173	0.0000	0.0000	0.9829	0.1095	0.0000	0.7372	0.1745	0.0000
0.7372	0.0000	0.0000	0.9763	0.1201	0.0000	0.7305	0.1738	0.0000
0.7571	0.0000	0.0000	0.9696	0.1263	0.0000	0.7239	0.1731	0.0000
0.7770	0.0000	0.0000	0.9630	0.1325	0.0000	0.7173	0.1723	0.0000
0.7970	0.0000	0.0000	0.9563	0.1387	0.0000	0.7106	0.1716	0.0000
0.8169	0.0000	0.0000	0.9497	0.1429	0.0000	0.7040	0.1709	0.0000
0.8235	0.0000	0.0000	0.9431	0.1470	0.0000	0.6973	0.1702	0.0000
0.8302	0.0000	0.0000	0.9364	0.1512	0.0000	0.6907	0.1691	0.0000
0.8368	0.0000	0.0000	0.9298	0.1545	0.0000	0.6841	0.1680	0.0000
0.8434	0.0000	0.0000	0.9231	0.1577	0.0000	0.6774	0.1670	0.0000
0.8501	0.0000	0.0000	0.9165	0.1610	0.0000	0.6708	0.1660	0.0000
0.8567	0.0000	0.0000	0.9099	0.1634	0.0000	0.6641	0.1650	0.0000
0.8634	0.0000	0.0000	0.9032	0.1658	0.0000	0.6575	0.1640	0.0000
0.8700	0.0000	0.0000	0.8966	0.1682	0.0000	0.6508	0.1626	0.0000
0.8767	0.0000	0.0000	0.8947	0.1686	0.0000	0.6442	0.1613	0.0000
0.8814	0.0000	0.0000	0.8929	0.1691	0.0000	0.6376	0.1600	0.0000
0.8862	0.0000	0.0000	0.8910	0.1696	0.0000	0.6309	0.1585	0.0000
0.8910	0.0000	0.0000	0.8862	0.1705	0.0000	0.6243	0.1571	0.0000
0.8929	0.0000	0.0000	0.8814	0.1714	0.0000	0.6176	0.1556	0.0000
0.8947	0.0000	0.0000	0.8767	0.1723	0.0000	0.6110	0.1543	0.0000
0.8966	0.0000	0.0000	0.8700	0.1732	0.0000	0.6044	0.1531	0.0000
0.9032	0.0048	0.0000	0.8634	0.1741	0.0000	0.5977	0.1518	0.0000
0.9099	0.0096	0.0000	0.8567	0.1749	0.0000	0.5911	0.1502	0.0000
0.9165	0.0144	0.0000	0.8501	0.1757	0.0000	0.5844	0.1486	0.0000
0.9231	0.0193	0.0000	0.8434	0.1765	0.0000	0.5778	0.1470	0.0000
0.9298	0.0241	0.0000	0.8368	0.1773	0.0000	0.5712	0.1454	0.0000
0.9364	0.0289	0.0000	0.8302	0.1775	0.0000	0.5645	0.1437	0.0000
0.9431	0.0337	0.0000	0.8235	0.1776	0.0000	0.5579	0.1421	0.0000
0.9497	0.0385	0.0000	0.8169	0.1777	0.0000	0.3719	0.0947	0.0000
0.9563	0.0432	0.0000	0.8102	0.1779	0.0000	0.1860	0.0474	0.0000
0.9630	0.0480	0.0000	0.8036	0.1781	0.0000			

B. Experimental Data Points Digitalization

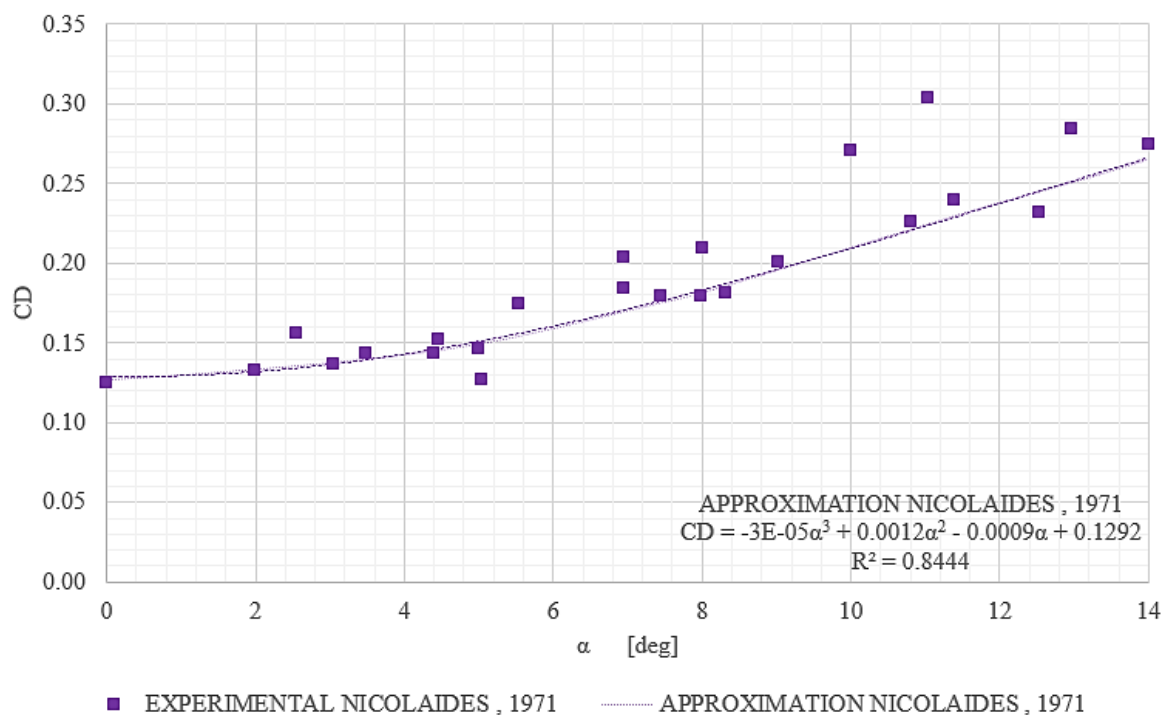
Figure B.1 presents the approximation curves and the experimental data points digitalized of the C_L , C_D and L/D values, from Figure 2.7 and Figure 2.8, for the investigations conducted by Nicolaides and Ware & Hassell.

Notice that the experimental data points digitalized correspond to the tests performed with a flow velocity of 50 ft/s and the tether method employed in the investigations. Additionally, the data digitalized correspond to experimental values for angles of attack up to 14° approximately.

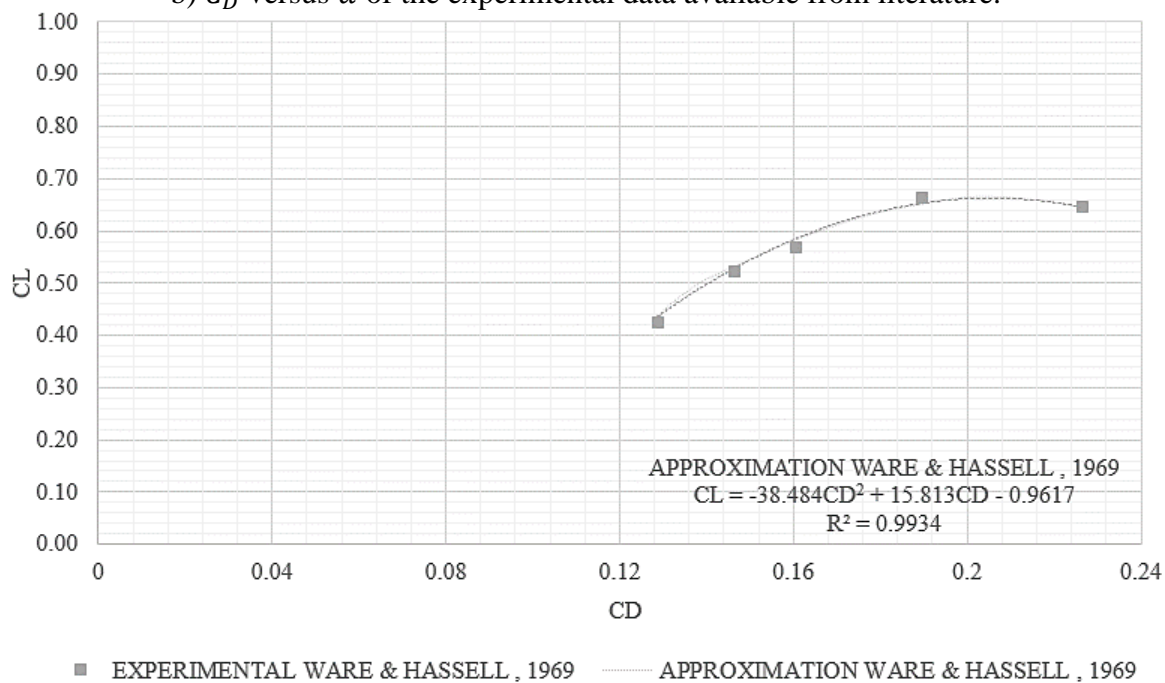
Finally, the authors applied a correction for the drag to obtain the values of just the canopy because of the unexposed lines effects during the experimental tests. This correction was implemented by subtracting a semi-empirical value determined by the authors. Consequently, Figure B.1 presents the C_D of the canopy only, i.e., corrected for the suspension lines effects.



a) C_L versus α of the experimental data available from literature.



b) C_D versus α of the experimental data available from literature.



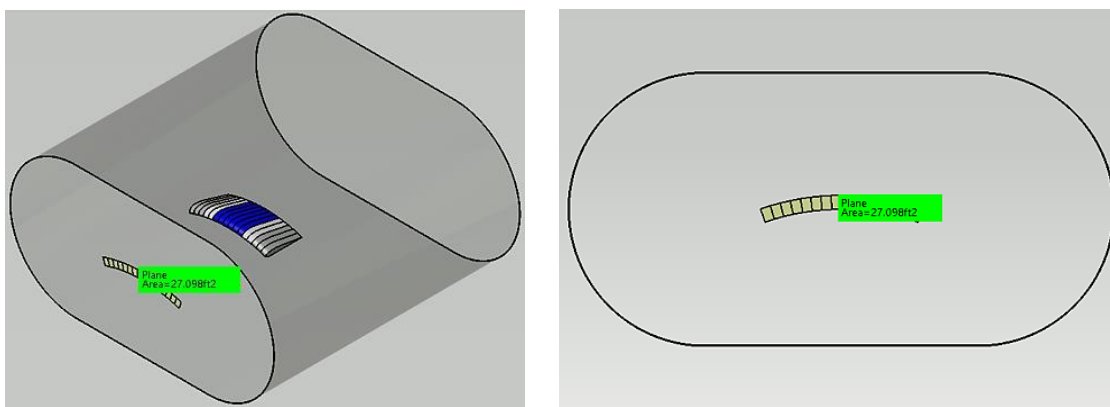
c) C_L versus C_D of the experimental data available from literature.

Figure B.1 Approximation curves and experimental data points digitalized from literature of C_L , C_D and L/D values for various angles of attack.

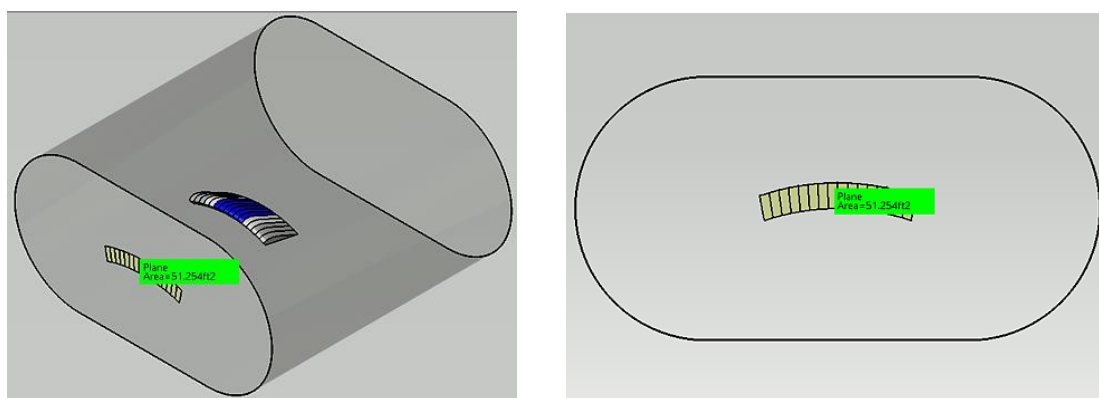
C. Blockage Area Estimation

The percentage of blockage area was estimated using a projected area of the canopy model and the cross section of the test section for Case 1 and Case 4.

Figure C.1 and Figure C.2 presents the test blockage areas corresponding to Case 1 and Case 4, respectively. Notice that calculation of the blockage area considered the canopy only, i.e., no suspension lines, with flat surfaces. Additionally, the blockage area for Case 1 was calculated assuming the test section of the NASA Langley Full Scale wind tunnel, which had an elongated hole test section of 30 ft x 60 ft and 56 ft long. Therefore, the cross section area of the test section was estimated to be 1606.86 ft².



a) Isometric and front view of the system at 0° angle of attack.

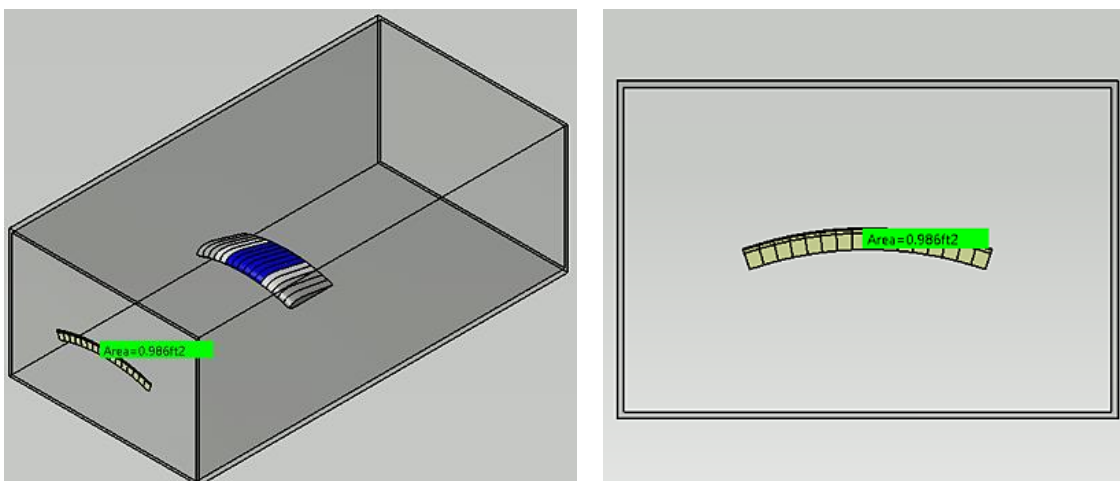


a) Isometric and front view of the system at 12° angle of attack.

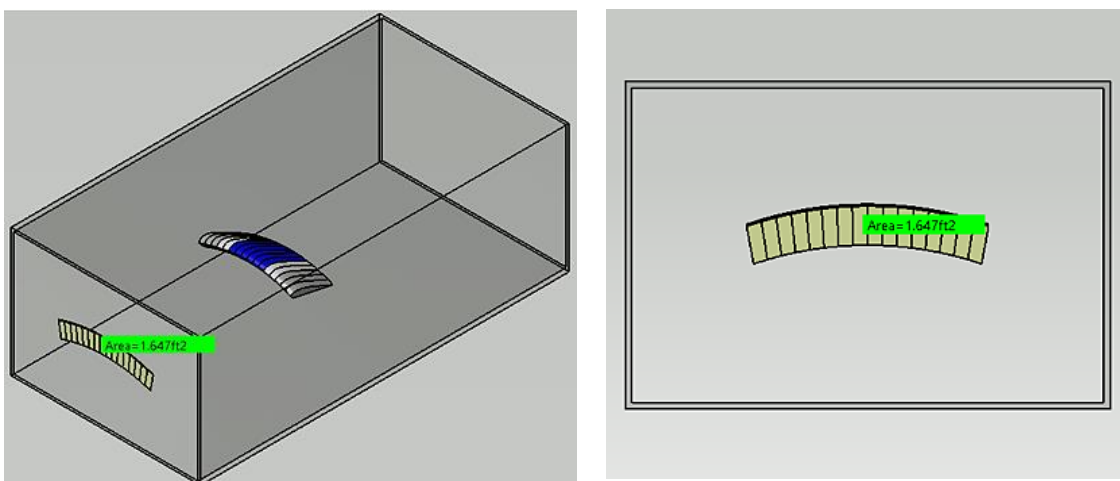
Figure C.1 Blockage area calculation for Case 1.

Consequently, the blockage area estimated for Case 1 ranged from 2% to 3% approximately when the angle of attack increased from 0° up to 12° .

In the same manner, the blockage area for Case 4 ranged from 4% to 7% approximately when the angle of attack increased from 0° up to 12° , which corresponded to the test section of the subsonic low speed wind tunnel from Embry-Riddle at MICAPLEX, which has a rectangle test section of 6 ft x 4 ft and 12 ft long.



a) Isometric and front view of the system at 0° angle of attack.



b) Isometric and front view of the system at 12° angle of attack.

Figure C.2 Blockage area calculation for Case 4.

D. CFD Results Summary

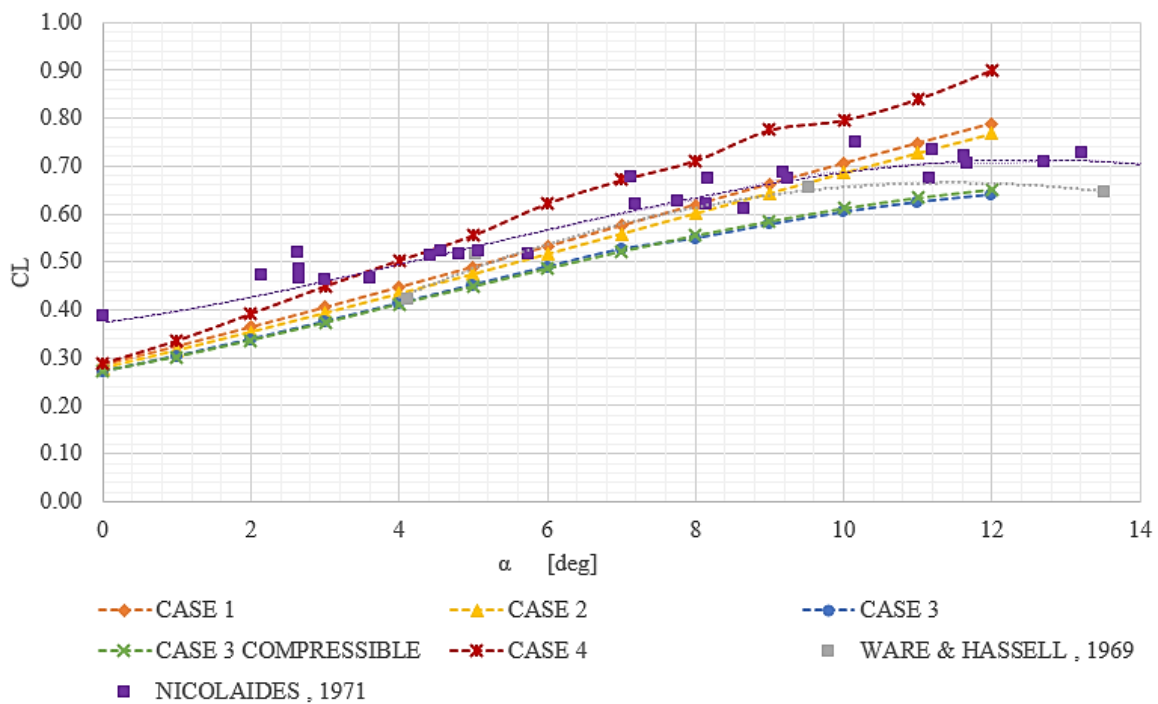
Table D.1 presents a summary of the calculated values of lift curve slope (a) along with the offset at $\alpha = 0^\circ$ and percentage of change of the lift curve slope for all the simulation cases as compared with Case 1. Notice the sign for the different values. A positive sign denotes an increment value, while a negative denotes a decrement value with respect to Case 1.

Table D.1

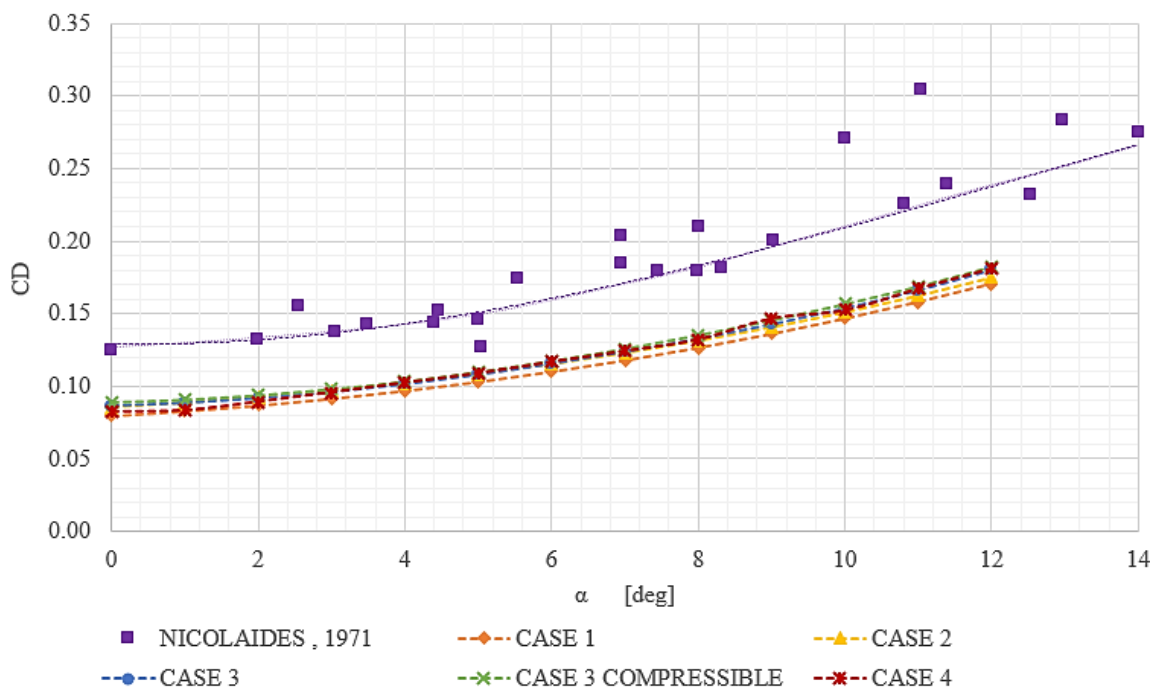
Summary of the calculated values of lift curve slope (a) along with the offset at $\alpha = 0^\circ$ and percentage of change of the lift curve slope for all the simulation cases as compared with Case 1.

SIMULATION CASE	a (1/deg)	CHANGE OF a (%)	C_L OFFSET AT $\alpha = 0^\circ$ (%)	C_D OFFSET AT $\alpha = 0^\circ$ (%)	L/D_{max}	CHANGE OF L/D_{max} (%)
CASE 1	0.0420	-----	-----	-----	4.89	-----
CASE 2	0.0407	-3	-2	+6.9	4.57	-6.47
CASE 3	0.0347	-17.4	-4.7	+8.5	4.25	-13.19
CASE 3 COMPRESSIBLE	0.0354	-15.7	-4.7	+10.3	4.15	-15.2
CASE 4	0.0529	+26	+1.4	+3	5.40	+10.45

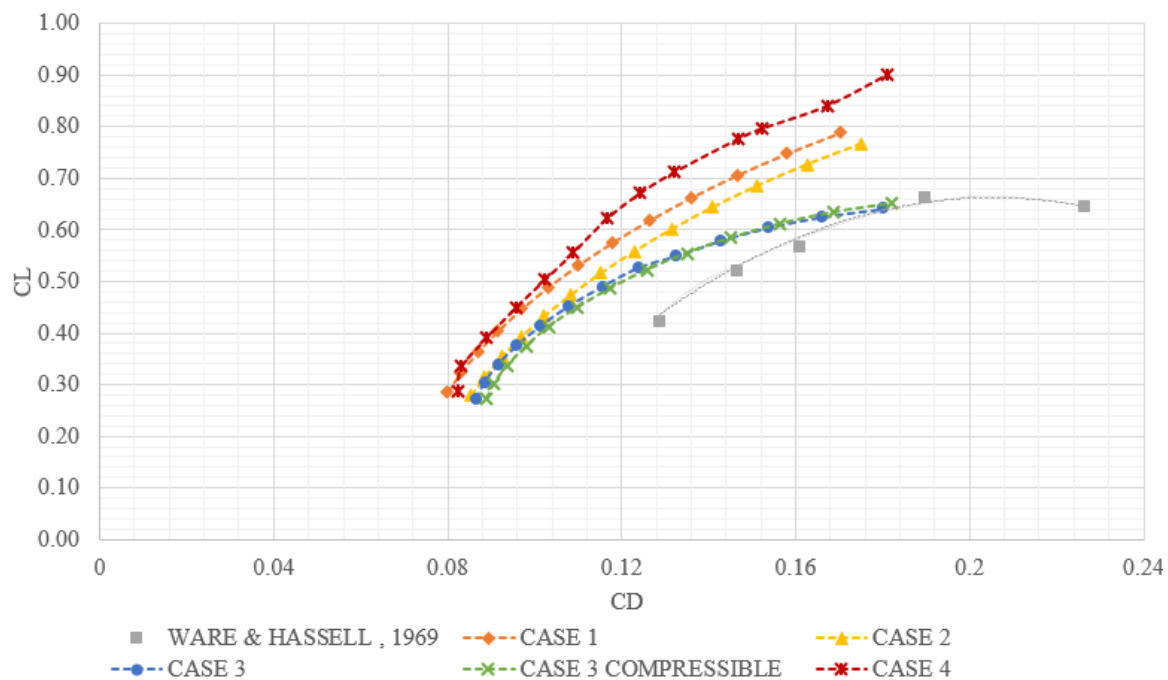
Figure D.1 presents a summary of the C_L , C_D and C_L/C_D curves for various angles of attack of the numerical simulations and the experimental data available from Ware & Hassell and Nicolaides.



a) C_L curves of the numerical simulations and the experimental data available from the literature.



b) C_D curves of the numerical simulations and the experimental data available from the literature.



c) C_L versus C_D curves of the numerical simulations and the experimental data available from the literature.

Figure D.1 Summary of the C_L , C_D and C_L/C_D curves for various angles of attack of the numerical simulations and the experimental data.

E. 2D Force Balance Development

E.1. Introduction

Experimental tests on wind tunnels commonly employ force balance systems to measure the aerodynamic forces of scaled models. This measurement system is generally located at the bottom wall, near the center of the test section. Therefore, the scaled model is placed where flow is homogeneous with minimum disturbances.

A physical limitation with experimental tests of flexible canopy models is that the suspension lines are attached to the forces and balance, e.g., tether test techniques, placing the scaled models near the outlet of the test section. Consequently, the aerodynamic forces and stability of the model are affected by flow disturbances at the outlet (Nicolaidis, 1971).

A simplified design of a 2D force and balance is presented in this chapter, with the purpose to be placed at the inlet of the test section, positioning the scaled canopy model near the center of the test section.

E.2. Force Measurement Approach

The force and balance design started by considering the lift and drag generated by a canopy from literature, to determine the range of forces expected for a scaled model tested in a wind tunnel. Therefore, one of the flexible canopies tested by Ware & Hassell was considered for the force and balance design.

Similar aerodynamic characteristics between the scaled and full canopy models are achieved when the non-dimensional parameters of Reynolds and Mach numbers, given by Equation (E.1) and (E.2), are approximately the same for the tests (Anderson, 2010), i.e.,

$$Re = \frac{\rho_{\infty} V_{\infty} c}{\mu} \quad (E.1)$$

$$M = \frac{V_{\infty}}{a} \quad (E.2)$$

Where V_{∞} is the flow velocity magnitude, a is the speed of sound, ρ_{∞} is the air density and μ is the air dynamic viscosity.

The air density was calculate using the ideal gas law, given by Equation (E.3).

Additionally, the speed of sound was calculated with Equation (E.4), while the dynamic viscosity was determined using Sutherland's Law, given by Equation (E.5).

$$P = \rho_{\infty} R_{gas} T \quad (E.3)$$

$$a = \sqrt{\gamma_{air} R_{gas} T} \quad (E.4)$$

$$\mu = \mu_0 \left(\frac{T}{T_0} \right)^{3/2} \frac{T_0 + 110}{T + 110} \quad (E.5)$$

Where P is the barometric pressure, T is the temperature in Kelvin, R_{gas} is the specific gas constant for dry air ($R_{gas} = 287.05 \text{ J}/(\text{kg K})$), γ_{air} is the ratio of specific heats for dry air ($\gamma_{air} = 1.4$), μ_0 and T_0 are the air dynamic viscosity and temperature at standard sea level conditions, respectively ($\mu_0 = 1.7894 \times 10^{-5} \text{ kg}/(\text{m s})$ and $T_0 = 288.16 \text{ K}$).

For incompressible and subsonic flow, effects of Reynolds number are more significant as compared effects caused by the Mach number (Anderson, 2010). Consequently, the Reynolds number for the canopy models was maintained by changing the chord length and flow velocity for the scaled canopy model.

Additionally, the lift and drag coefficients, expressed by Equations (E.6) and (E.7), respectively, relate the aerodynamic forces of the different canopies under similar Reynolds number (Anderson, 2010), i.e.,

$$C_L = \frac{L}{\frac{1}{2} \rho_{\infty} V_{\infty}^2 S} \quad (E.6)$$

$$C_D = \frac{D}{\frac{1}{2} \rho q_\infty V_\infty^2 S} \quad (\text{E.7})$$

Where L is the lift force and D is the drag force of the canopy model. Table E.1 presents the canopy geometry characteristics and flow conditions for one specific angle of attack tested by Ware & Hassell.

Table E.1
Geometry characteristics and flow conditions for a canopy model tested by Ware & Hassell.

CANOPY GEOMETRY		
DESCRIPTION	PARAMETER	VALUE
CHORD LENGTH	c	8.57 ft
SPAN LENGTH	b	17.14 ft
PLANFORM AREA	S	146.89 ft ²
ASPECT RATIO	AR	2
ANGLE OF ATTACK	α	APPROX. 4.1 °
FLOW CONDITIONS		
DESCRIPTION	PARAMETER	VALUE
FLOW VELOCITY	V	50 ft/s
AIR DENSITY	ρ	0.002378 slug/ft ³
REYNOLDS NUMBER	Re	2.727×10^6
AIR DYNAMIC VISCOSITY	μ	3.737×10^{-7} slug/(s ft)

Results of the experiment conducted by Ware & Hassell determined the values of the lift and drag coefficients of the canopy to be approximately $C_L = 0.4229$ and $C_D = 0.1288$, respectively.

The dimensions of the wind tunnel test section determined the scale factor for the chord length reduction of the scaled canopy model. Additionally, the dimensions of small kites available in the market were also considered to determine the scale factor.

Therefore, the scaled canopy model considered for the design of the force and balance had a chord length approximately five times smaller compared with the canopy from Ware & Hassell.

Table E.2 shows the scaled canopy geometry characteristics and the flow conditions to meet the same Reynolds number as the experiment of Ware & Hassell.

Table E.2

Geometry characteristics and flow conditions for the scaled canopy model for the force and balance design.

CANOPY GEOMETRY		
DESCRIPTION	PARAMETER	VALUE
CHORD LENGTH	c	1.71 ft
SPAN LENGTH	b	3.43 ft
PLANFORM AREA	S	5.88 ft ²
ASPECT RATIO	AR	2
ANGLE OF ATTACK	α	4 °
FLOW CONDITIONS		
DESCRIPTION	PARAMETER	VALUE
FLOW VELOCITY	V	250 ft/s
AIR DENSITY	ρ	0.002378 slug/ft ³
REYNOLDS NUMBER	Re	2.720x10 ⁶
AIR DYNAMIC VISCOSITY	μ	3.737x10 ⁻⁷ slug/(s ft)

Figure E.1 presents the aerodynamic forces of lift, drag and the resultant presented in a ram-air parachute model.

The force and balance design was capable to determine lift and drag forces by measuring the resultant force P_R and the inclination angle θ exerted by the canopy tested, as shown in Figure E.1. Additionally, notice that the resultant load P_R and the inclination angle θ depend on the angle of attack of the canopy.

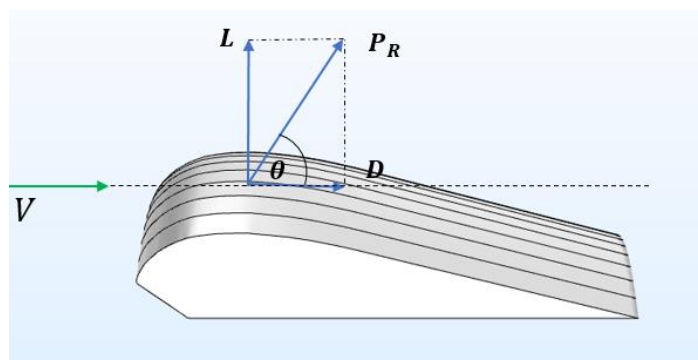


Figure E.1 Lift, drag and resultant aerodynamic forces on a ram-air parachute.

The resultant force expected for the scaled canopy model was calculated from Equations (E.6) and (E.7), solving for the lift and drag forces, i.e.,

$$L_{sc} = \frac{1}{2} C_L q_{\infty} V_{\infty}^2 S \quad (\text{E.8})$$

$$D_{sc} = \frac{1}{2} C_D q_{\infty} V_{\infty}^2 S \quad (\text{E.9})$$

Where L_{sc} is the lift force and D_{sc} is the drag force of the scaled canopy model. Table E.3 gives the lift and drag forces along with the resultant force of the canopy of Ware & Hassell and the scaled canopy model.

Table E.3

Lift, drag and resultant forces of the Ware & Hassel canopy and the scaled canopy model

FORCE	CANOPY MODEL	
	WARE & HASSELL	SCALED MODEL
LIFT	184.65 lb	184.80 lb
DRAG	56.24 lb	56.28 lb
RESULTANT	193.03 lb	193.18 lb

The resultant force expected for a wind tunnel test of the scaled canopy model was 193 lb (859 N) approximately. The different equipment and experimental set-up for the design of the force and balance are presented in the following section, along with the various physical limitations that were addressed.

E.3. Equipment and Experimental Setup

Selection of the equipment for the force and balance design started with an adequate force sensor to be placed at the inlet of the wind tunnel test section. Although, the expected resultant load determined for the scaled canopy model was the main criteria to select the sensor, other constraints included low cost, physical dimensions and simplicity of the design. Therefore, a sensor capable to measure a maximum of 77 lb (343 N) was selected for the purposes of this investigation.

Figure E.2 presents the weight sensor and the different equipment necessary for the design of the force and balance.

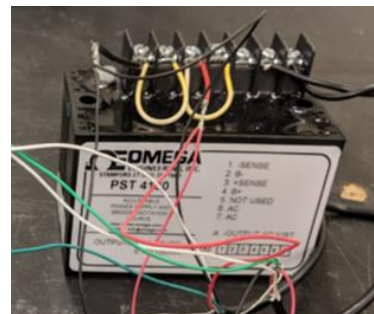
The sensor selected consisted on a combination of strain gages in a beam type load cell. Figure E.2a shows the beam load cell. The mechanism to measure the force was by applying a load at one end of the beam while maintaining the other end fixed to the ground. Additionally, the load cell had a rated output of 1.996 mV/V, necessary for the calculation of the applied load.

The load cell required an excitation or input constant voltage of +10 Volts, which was provided by a voltage supply, as shown in Figure E.2b. The data were collected using a National Instruments data acquisition system (Ni DAQ) of ± 0.5 Volts input voltage, as shown in Figure E.2c.

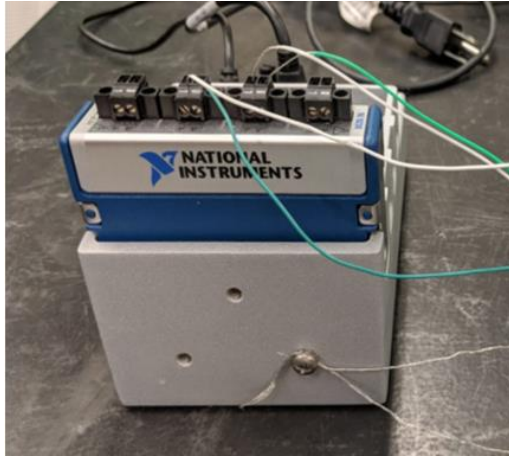
Various set of weights, set 1 in Figure E.2d ranging from 0 to 80 N and set 2 in Figure E.2e ranging from 0 to 55 N, were utilized to calibrate the load cell. Finally, multiple miscellaneous equipment such as wires, screws, metal brackets, wood sheet and a weight mount were used for the assembly and set-up of the force balance system, as shown in Figure E.2f.



a) Weight sensor, beam load cell



b) Constant voltage supply



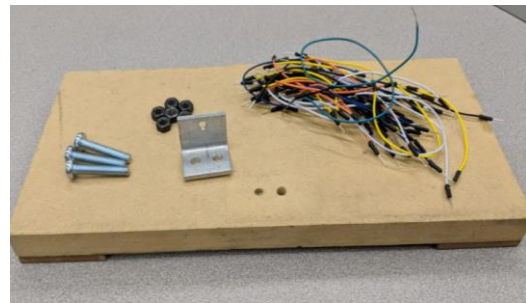
c) National Instruments DAQ



d) Set of weights, set #1



e) Set of weights, set #2



f) Miscellaneous equipment

Figure E.2 Beam load cell and multiple equipment employed for the force and balance development and calibration.

Experimental tests with a single load cell provided with data to calibrate the force sensor, i.e., the offset from manufacture. The assembly and experimental set-up of the system required multiple wiring connections along with the various machined holes for the screws in the wood sheet and the brackets. Figure E.3 shows a schematic representation of the different wiring connections for the experimental tests with a single load cell.

The load cell was connected to the power supply with the black and red wires, i.e., ground and positive voltage, respectively, as shown in Figure E.3. Additionally, the output signal from the load cell was connected to the Ni DAQ, as shown with the green

wire in Figure E.3. The DAQ transferred the data collected to a personal computer (PC) for the post processing.

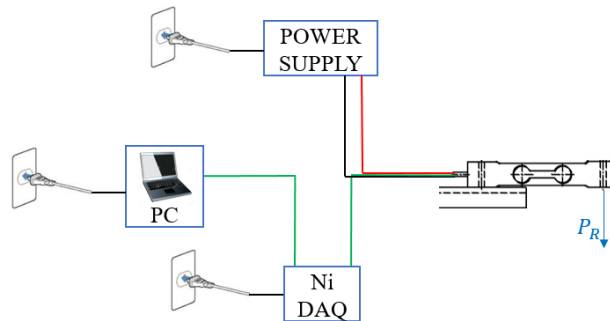


Figure E.3 Schematic of the experimental set-up for the single load cell system.

Similar to the single load cell system, a combination of two load cells provided data to calibrate the weight sensors when assembled together. Figure E.4 shows a schematic of the two load cells in the assembly along with the wiring connections for the experiments.

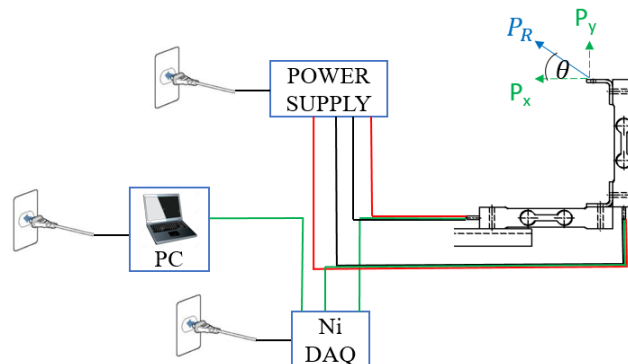


Figure E.4 Schematic of the experimental set-up for the load cell arrangement.

This combination of load cells, referred as load cell arrangement in this investigation, enabled the force measurements in the vertical and horizontal directions. Therefore, the resultant load P_R and the inclination angle θ were determined using the measurements from the two load cells. Finally, similar wiring connections as the single load cell system were employed for the cell arrangement, as shown in Figure E.4. The data collected by the Ni DAQ was stored up for the post processing using a PC.

E.4. Data Reduction

An interface, developed in MATLAB R2016b, allowed the user to communicate the Ni DAQ with the PC for the data collection. Multiple experiments were conducted using the single and two load cells provided, with raw data stored for later post process using MATLAB scripts.

All the experiments were conducted with a sample rate of 10,000 samples per second and a sampling time of 10 seconds. The average of the sampling data was converted from Volts to N using a conversion factor, which was determined using the maximum weight, the rated output and the excitation voltage for the load cells provided by the manufacture. The conversion factor (CF) is expressed as:

$$CF = \frac{\text{maximum weight}}{\text{rated output} \cdot \text{excitation voltage}} \quad (\text{E.10})$$

$$CF = \frac{343}{0.001996 \cdot 10}$$

$$CF \approx 17,184 \quad (\text{N / Volt})$$

E.4.1. Single Load Cell Calibration

The purpose of the single load cell calibration was to tare the load measurements. For this calibration, various tests were conducted using the set 1 of weights as shown in Figure E.2d. The weights were previously measured parallel using a scale to determine the value of the loads, denominated in this investigation as *actual loads*.

The multiple weights were applied to the system to determine the forces measured by the single load cell, designated in this investigation as *load cell measurement* (P_{load_cell}). Figure E.5 shows a calibration test for the single load cell system with a tested weight of 7.34 N.

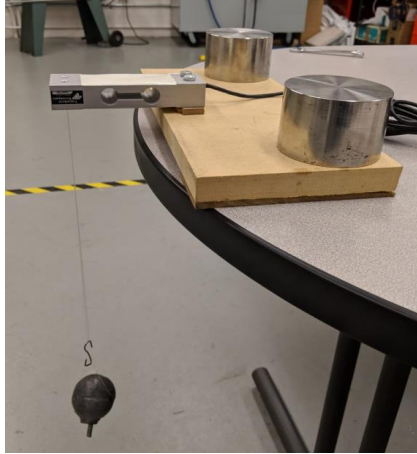


Figure E.5 Single load cell system calibration test with a weight of 7.34 N.

Results of different tests, the load cell measurements had a difference of 3.8% compared to the actual loads for weights higher than 0.5 N. Therefore, a correlation was determined between the difference of the actual loads and the load cell measurements, defined by Equation (E.11), i.e.,

$$P_{offset} = 2.2799 \times 10^3 V_{out}^2 - 409.5515 V_{out} - 0.0992 \quad (\text{Newton}) \quad (\text{E.11})$$

Where P_{offset} is the offset load in N and V_{out} is the output signal from the load cell in Volts. This second order polynomial correlation was obtained using the MATLAB function *polyfit* (The MathWorks, Inc, 2018). Consequently, the corrected measurements are given by Equation (E.12), i.e.,

$$P_{corrected} = P_{load_cell} + P_{offset} \quad (\text{E.12})$$

Where $P_{corrected}$ is the load cell measurement with offset correction. The single load cell system was tested repeatedly with the same loads, including the offset given by Equation (E.11).

Figure E.6 shows the loads measured by the single load cell before and after implementing the correction from Equation (E.11). The corrected measurements, shown

by green diamonds, were closer to the actual loads especially at high-applied loads.

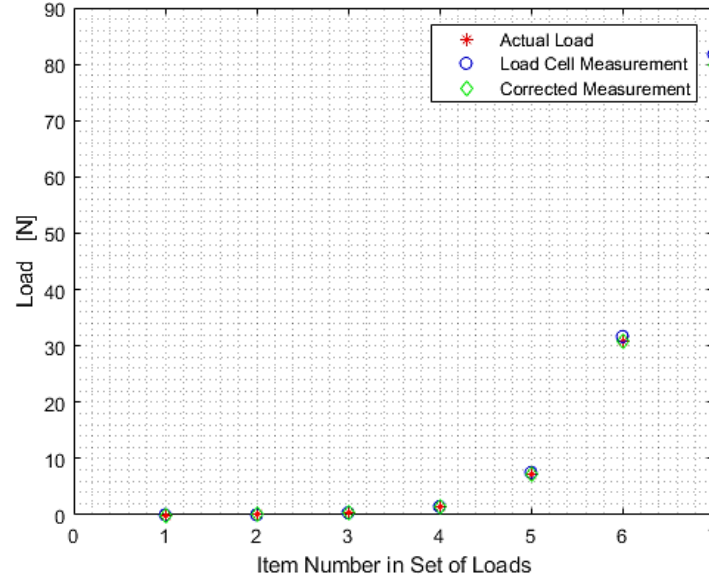


Figure E.6 Corrected load measurements for a single load cell.

For weights higher than 0.5 N applied to the single load cell, the corrected measurements had a difference less than 0.5% compared to the actual loads. Consequently, further tests with the load cells included the offset correction, as presented for the load cell arrangement in the following subsection.

E.4.2. Load Cell Arrangement Calibration

Similarly to the single load cell system, the main objective of the cell arrangement was to determine the calibration curves of each load cell, which determined an approximation of the resultant applied load P_R and inclination angle θ , as shown in Figure E.4. The calibration of the cell arrangement were performed using the set 2 of weights, as shown in Figure E.2e. In the same manner, the weights were previously measured apart using a scale to determine the value of the loads.

Multiple tests were conducted by applying the weights at different inclination angles to the cell arrangement system. Figure E.7 shows a calibration test for the cell

arrangement system with a tested weight of 7.34 N.

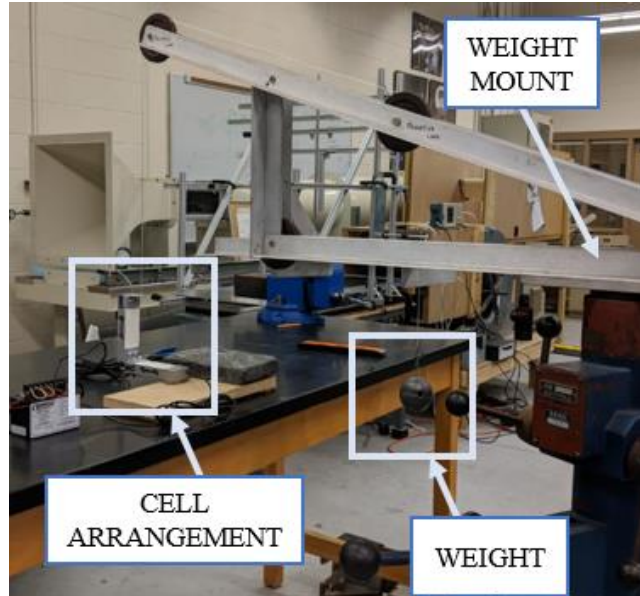


Figure E.7 Calibration test for the cell arrangement system with a weight of 7.34 N and an inclination angle of 90° approximately.

During the experiments, each load cell measured individually a force. Therefore, the forces measure by the vertical load cell were called F_1 forces, while for the horizontal load cell were called F_2 forces.

The post processing of the data consisted on creating two 3D matrices with the experimental values of the weights, inclination angles and forces measured by each load cell. For instance, the 3D matrix for the vertical load cell consisted on [applied weights \mathbf{X} inclination angles \mathbf{X} forces F_1]. In the same manner, the 3D matrix for the horizontal load cell consisted on [applied weights \mathbf{X} inclination angles \mathbf{X} forces F_2].

These matrices were utilized to calculate the calibration curves for the cell arrangement by using the MATLAB function *fit*, with method *poly23* (The MathWorks, Inc, 2018). Equations (E.13) and (E.14) show the corresponding calibration curves for each load cell, i.e.,

$$F_1 = a_0 + a_1\theta + a_2P_R + a_3\theta^2 + a_4\theta P_R + a_5P_R^2 + a_6\theta^2 P_R + a_7\theta P_R^2 + a_8P_R^3 \quad (\text{E.13})$$

$$F_2 = b_0 + b_1\theta + b_2P_R + b_3\theta^2 + b_4\theta P_R + b_5P_R^2 + b_6\theta^2 P_R + b_7\theta P_R^2 + b_8P_R^3 \quad (\text{E.14})$$

Where F_1 and F_2 are given in N, P_R is in Newton, θ is in radians and the curve fit values

a_i and b_i given in Table E.4.

Table E.4

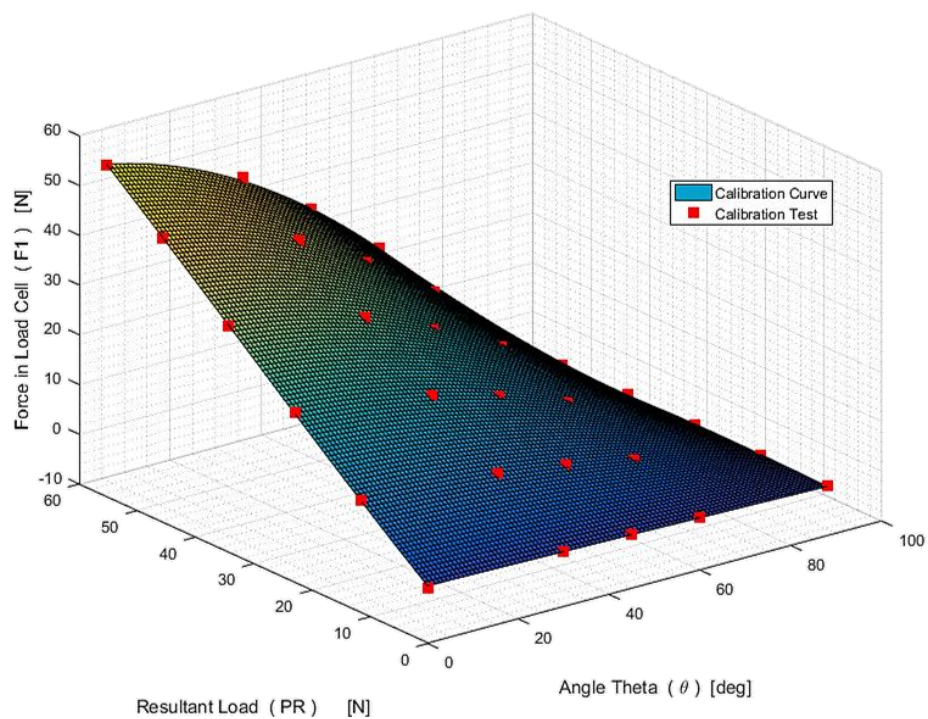
Values of coefficients a_i and b_i for equation of the cell arrangement calibration curves.

a_0	=	1.59		b_0	=	-1.291
a_1	=	-0.8791		b_1	=	1.339
a_2	=	0.9229		b_2	=	0.01178
a_3	=	-0.1328		b_3	=	-0.314
a_4	=	-0.07005		b_4	=	1.139
a_5	=	0.003283		b_5	=	-7.552×10^{-5}
a_6	=	-0.3338		b_6	=	-0.3249
a_7	=	-0.001984		b_7	=	-0.000131
a_8	=	-3.457×10^{-5}		b_8	=	5.335×10^{-6}

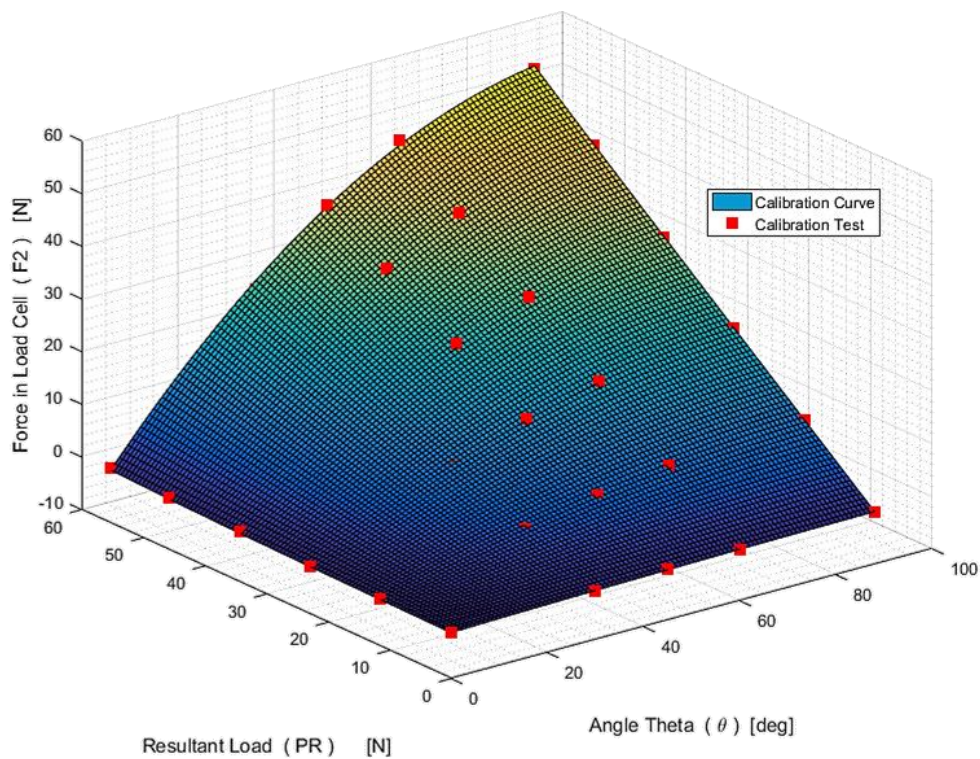
Difference of the calibration curves with respect to the tests was determined by the value of R^2 , the curves had a R^2 of 0.9994 and 0.9991 for the vertical and horizontal load cells, respectively.

Figure E.8 shows the calibration curves for the vertical and horizontal load cells. Additionally, Figure E.8 includes the experimental data from the multiple tests at different inclination angles utilized to determine the curves, designated as *calibration test*.

The methodology to approximate the resultant load and the inclination angle using the calibration curves, starts by measuring the forces in the vertical and horizontal load cells (F_1 and F_2 forces, respectively) during a test. The intercept point of the contour plots from the calibration curves at F_1 and F_2 , determine the magnitude of the resultant load and the inclination angle.



a) Calibration curve for the vertical load cell (F_1 force).



b) Calibration curve for the horizontal load cell (F_2 force).

Figure E.8 Calibrations curves for the cell arrangement and experimental data.

Multiple tests to validate the calibration curves, limitations of the cell arrangement design and discussion of the results using the procedure to determine P_R and θ are presented more in detail as followed.

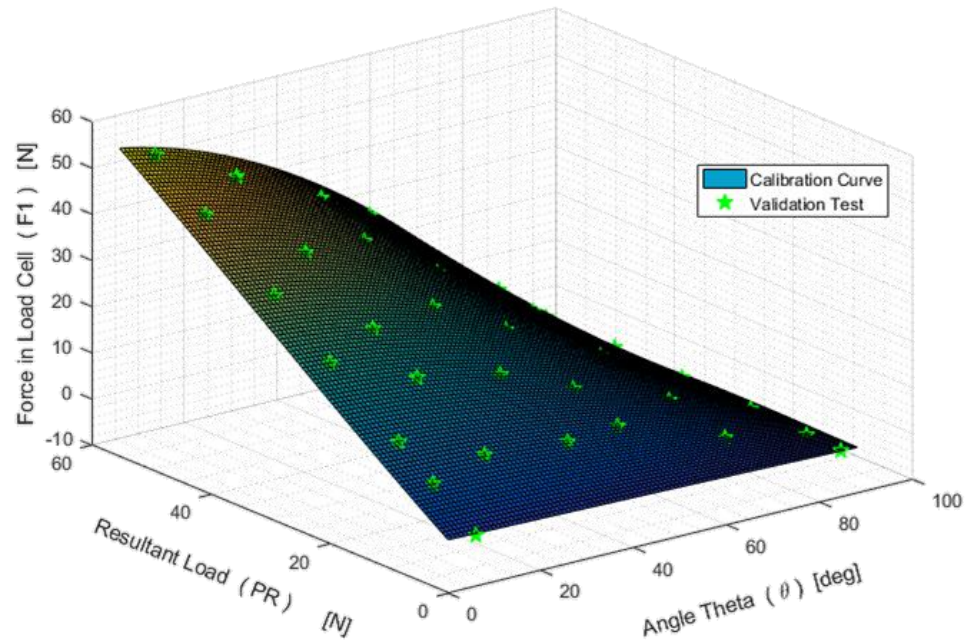
E.5. Results and Discussion

The present chapter summarizes the main outcomes obtained for the different studies performed in this investigation. The chapter starts with the 2D force and balance results, including validation under different load conditions along with limitations of the design for future reference.

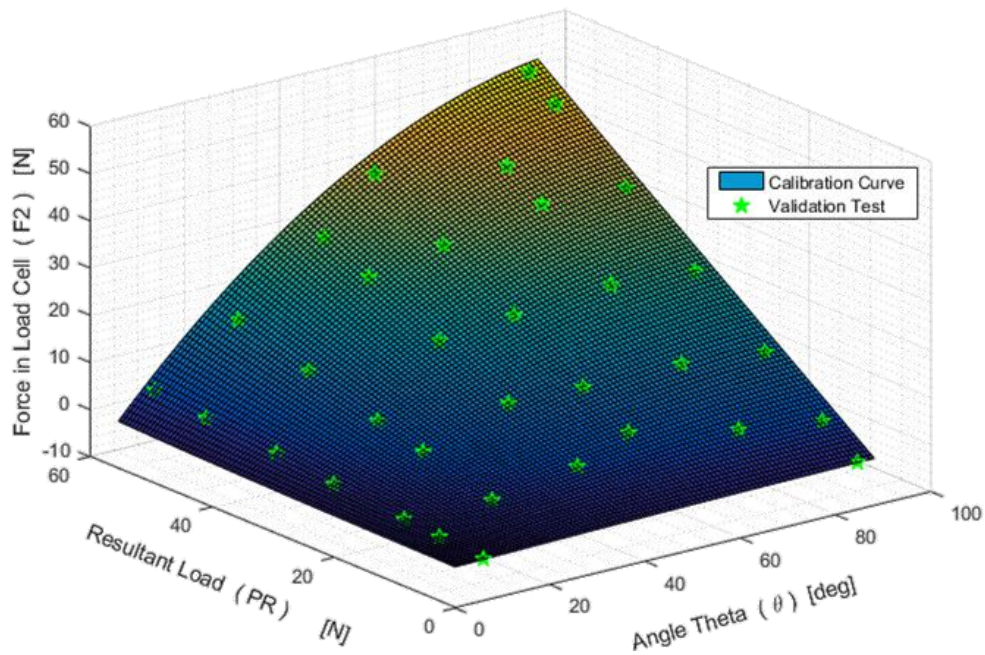
The load cell arrangement was tested with various load at different angles to validate the calibration curves and determine the resultant load P_R and inclination angle θ using the methodology explained previously. The validation tests employed the set 2 of weights, as presented in Figure E.2e.

Figure E.9 presents the calibrations curves determined previously along with multiple validations tests, denoted in this investigation as *Validation Test*, shown with the green stars. Additionally, notice that the applied loads for the various tests ranged between $0 \leq P_R \leq 55$ N, while for the inclination angle the tests ranged between $0^\circ \leq \theta \leq 90^\circ$, approximately.

Although each load cell was capable to measure up to 77 lb (343 N), the load cell arrangement was tested with a maximum resultant force of 55 N. The main reason of this range was the steadiness of the load cell arrangement and the limitation of the equipment employed to withstand the moment produced by high loads in the mount.



a) Vertical load cell.



b) Horizontal load cell.

Figure E.9 Calibration curves for the load cell arrangement along with experimental tests for validation.

As a reminder from chapter 3, the resultant load P_R and inclination angle θ were calculated by intercepting the contour plots, presented in Figure E.9, at the measured

forces F_1 and F_2 by the load cells for a specific test.

For example, Figure E.10 presents the contour plots of the vertical and horizontal curves when the load cell arrangement was tested with a resultant load of 30.2 N at an inclination angle of 51° , approximately. The forces measured by the load cells were: vertical load cell $F_1 = 18.33$ N and horizontal load cell $F_2 = 23.18$ N, illustrated as the red and blue lines, respectively.

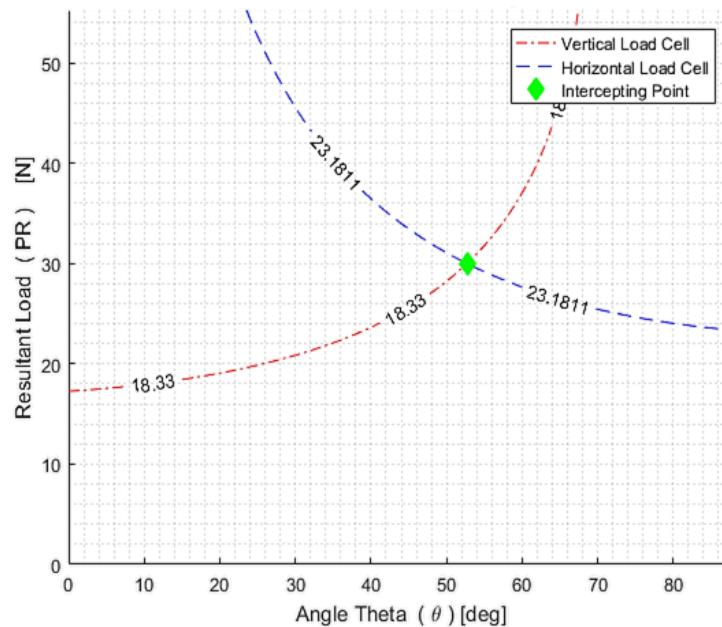


Figure E.10 Contour plots of the forces measured by the load cells in the cell arrangement for an applied load of 30.2 N at an inclination angle of 51° , approximately.

The intercepting point, as shown with the green diamond in Figure E.10, approximated the resultant load P_R in the vertical axis and inclination angle θ in the horizontal axis. For this particular case, the load cell arrangement estimated a resultant load of $P_R = 30$ N and an inclination angle of $\theta = 52.7^\circ$. Additionally, differences for the resultant load P_R and inclination angle θ for this case were 0.66% and 3.33%, respectively.

Figure E.11 presents the percentage of difference of the resultant load P_R and inclination angle θ for the multiple tests to validate the calibration curves. The highest

differences were approximately of 2.29% and 3.33% for resultant load P_R and inclination angle θ , respectively. These differences were attributed to several reasons:

- Measurements of the inclination angle during the tests were performed using a digital level with an error of $\pm 0.35^\circ$.
- The weights were measured in a separate scale to determine the actual load. The scale provided measurements with an error less than ± 0.02 N approximately (± 0.002 Kg).
- Oscillations of the applied load while hanging in the weight mount during the experiments.
- Vibrations and oscillations of the load cell arrangement system caused by the momentum produced with high loads in the weight mount.
- Differences caused by deflection of the brackets in the assembly of the load cell system.
- Approximations of the results during the post process of the raw data.

Additionally, for inclination angles θ near 0° or 90° , or for applied resultant loads P_R below 5 N, the difference increased drastically up to 50%. Therefore, Figure E.11 presents 32 of the 34 tests performed for the validation of the curves.

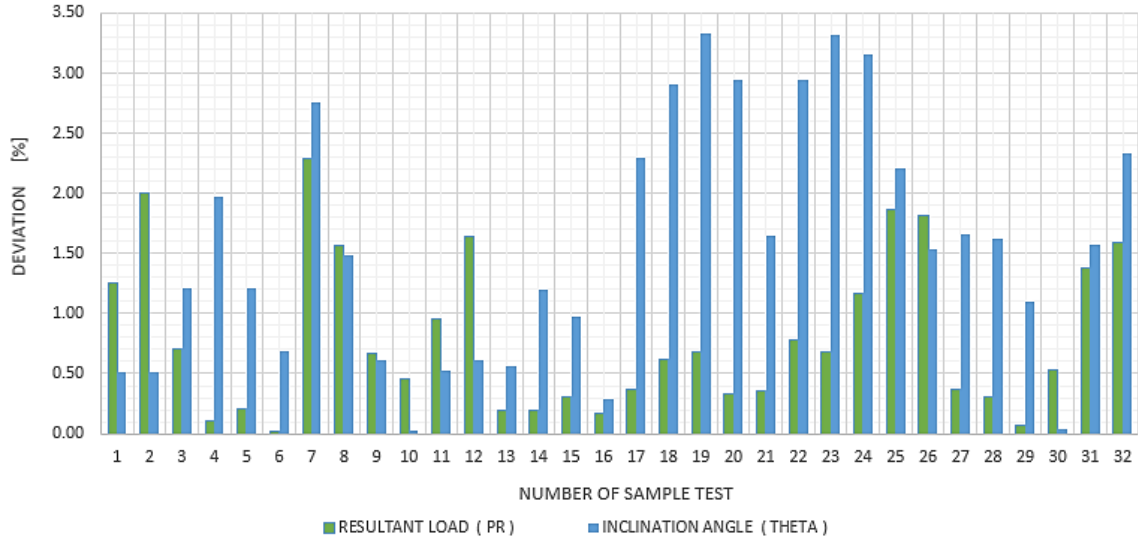


Figure E.11 Percentage of difference of the resultant load P_R and inclination angle θ for the validation tests.

Finally, the cell arrangement was able to predict a resultant load P_R and inclination angle θ with an error less than 3.5% under the following conditions:

- A minimum required load P_R applied to the load cell arrangement of 5 N (1.12 lb approximately).

A range for the inclination angle θ of $5^\circ \leq \theta \leq 85^\circ$ (considering 0° parallel to the horizontal axis, as presented in Figure E.4).

Figure E.12 presents the isometric, top, front and side views for the assembly of the 2D force balance and canopy model inside the test section of the wind tunnel. Notice that the lines were drawn for reference only.

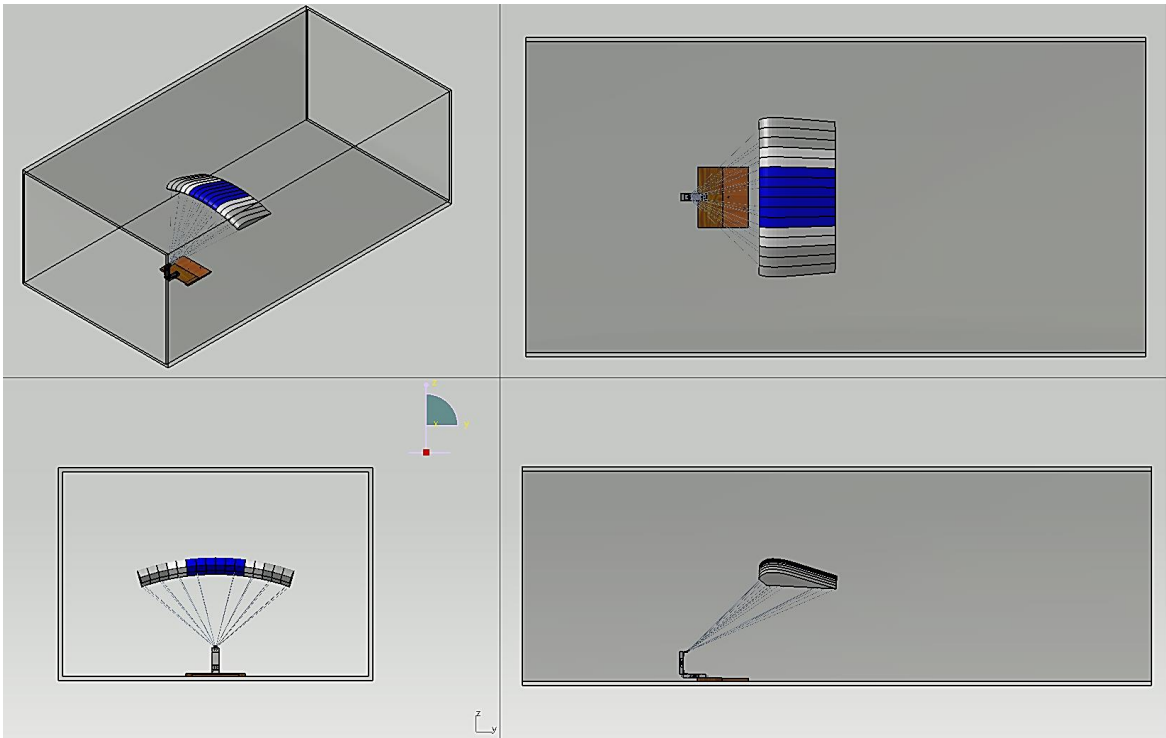


Figure E.12 Isometric, top, front and side view for future the experimental tests in the wind tunnel at Embry-Riddle.